Thermoelectric performance of p-type TiCoSb half-Heusler compounds – Intrinsic phase separation and charge carrier concentration optimization as key to high efficiency

Dissertation
zur Erlangung des Grades
"Doktor der Naturwissenschaften"
im Promotionsfach Chemie
am Fachbereich Chemie, Pharmazie und Geowissenschaften
der Johannes Gutenberg-Universität Mainz

vorgelegt von
Elisabeth Rausch
geboren in Böblingen

Mainz, Juni 2015

Dekan:

1. Berichterstatter:
2. Berichterstatter:

Tag der mündlichen Prüfung: 24.07.2015

D77

Dissertation, Johannes-Gutenberg Universität Mainz

Die vorliegende Arbeit wurde in der Zeit von März 2012 bis Juni 2015 am Institut für Anorganische und Analytische Chemie im Fachbereich Chemie, Pharmazie und Geowissenschaften der Johannes Gutenberg-Universität, Mainz, sowie am Max-Planck Institut für Chemische Physik fester Stoffe, Dresden unter der Leitung von angefertigt.

Mainz, Juni 2015

Hiermit versichere ich, dass ich die vorliegende Dissertation selbstständig verfasst und keine anderen als die angegebenen Hilfsmittel benutzt habe. Alle der Literatur entnommenen Stellen sind als solche gekennzeichnet.

Mainz, Juni 2015

Contents

1 Abstract

Thermoelectric (TE) generators, composed of pairs of n-type and p-type materials, directly transform waste heat into useful electricity. The efficiency of a thermoelectric material depends on its electronic and lattice properties, summarized in its figure of merit ZT. Desirable are high electrical conductivity σ and Seebeck coefficients S, and low thermal conductivity κ. Half-Heusler materials crystalizing in the space group $F\bar{4}3m$ with the general formula XYZ (X, Y transition metals, Z main group element) with 18 valence electrons per formula unit are very promising candidates for thermoelectric applications in the medium-temperature range such as in industrial and automotive waste heat recovery [1–7]. The advantage of Heusler compounds are excellent electronic properties and high thermal and mechanical stability, as well as their low toxicity and elemental abundance [5–10]. Thus, the main obstacle to further improving their TE performance is their relatively high thermal conductivity.

Recently, the concept of an intrinsic phase separation has become a focus of research to achieve low thermal conductivities and boost the TE performance in half-Heusler compounds. In particular, the n-type (Ti/Zr/Hf)NiSn system has been investigated in this regard [11–16] leading to several patent applications [17–20]. In contrast state-of-the-art p-type materials are found in the (Ti/Zr/Hf)$CoSb_{0.8}Sn_{0.2}$ system [2, 3, 21, 22]. A breaktrough was achieved by reducing the lattice thermal conductivity by a nanostructuring approach via ball milling of $Zr_{0.5}Hf_{0.5}CoSb_{0.8}Sn_{0.2}$ followed by a rapid consolidation method [2].

However, the phase separation approach can form a significant alternative saving processing time, energy consumption and increasing the thermoelectric efficiency. This concept is transfered to the p-type (Ti/Zr/Hf)$CoSb_{0.8}Sn_{0.2}$ system and a reliable fabrication procedure is elaborated. Mandatory is the alloying of Ti together with Hf in order to achieve phase separation in two half-Heusler phases. The microstructuring leads to a similar TE performance as by the ball milling approach [2, 23].

A fundamental concept to tune the performance of thermoelectric materials is charge carrier concentration optimization. Investigations of $Ti_{0.3}Zr_{0.35}Hf_{0.35}CoSb_{1-x}Sn_x$ prove that the optimum carrier concentration is reached with a substitution level of $x = 0.15$, which yields the maximum $ZT = 0.8$. This is an enhancement of about 40% compared to samples with $x = 0.2$.

The TE performance can be enhanced further by a fine-tuning of the Ti to Hf ratio. A correlation of the microstructuring and the thermoelectric properties can be observed and a record thermoelectric figure of merit $ZT = 1.2$ at 710°C was reached with the composition $Ti_{0.25}Hf_{0.75}CoSb_{0.85}Sn_{0.15}$.

The study is complemented by a long-term stability test under thermal cycling conditions. A heat treatment of the material similar to actual conditions of operation, such as occurs during the energy conversion from an automotive exhaust pipe, is simulated and the impact on the structural and thermoelctric properties is investigated. Particulary, the best and most reliable performance is achieved in $Ti_{0.5}Hf_{0.5}CoSb_{0.85}Sn_{0.15}$, which reached a maximum figure of merit ZT of 1.1 at 700°C. The intrinsic phase separation and resulting microstructuring is stable even after 500 heating and cooling cycles.

2 List of Publications

Most parts of this work were published in scientific journals, as listed below:

1. E. Rausch, B. Balke, S. Ouardi, and C. Felser
Enhanced thermoelectric performance in the p-type Half-Heusler (Ti/Zr/Hf)$CoSb_{0.8}Sn_{0.2}$ system via phase separation.
Phys. Chem. Chem. Phys. 16 (2014) 25258.

2. E. Rausch, B. Balke, T. Deschauer, S. Ouardi, and C. Felser
Charge carrier concentration optimization of thermoelectric p-type half-Heusler compounds.
APL Mater. 3 (2015) 041516.

3. E. Rausch, S. Ouardi, U. Burkhardt, C. Felser, J. M. Stahlhofen, and B. Balke
Fine tuning of thermoelectric performance in phaseseparated half-Heusler compounds.
Accepted Manuscript, J. Mat. Chem. C (2015) DOI: 10.1039/C5TC01196E.

4. E. Rausch, B. Balke, S. Ouardi, and C. Felser
Long-term stability of thermoelectric state-of-the arte p-type half-Heusler compounds upon thermal cycling.
Accepted Manuscript, Energy Technol. (2015) DOI: 10.1002/ente.201500183.

5. C. Wang, J. Meyer, N. Teichert, A. Auge, E. Rausch, B. Balke, A. Hütten, G. H. Fecher, and C. Felser
Heusler nanoparticles for spintronics and ferromagnetic shape memory alloys.
J. Vac. Sci. Technol. B 32, (2014) 020802.

6. J. M. Mena, E. Rausch, S. Ouardi, T. Gruhn, G. H. Fecher, H. G. Schoberth, H. Emmerich, and C. Felser
Miscibility gap in the phase diagrams of thermoelectric half-Heusler materials $CoTi_{1-x}Y_xSb$ (Y = Sc, V, Mn, Fe).
Submitted to Journal of Electronic Materials (ICT 2015 proceedings).

3 Introduction

3.1 Thermoelectric energy conversion

The quest to solve the world's energy problem, reduce CO_2 emissions, and find alternative and sustainable energy sources is more than ever a hot topic. A great amount of the produced energy is not even used but rejected, most of it as waste heat. In Germany about 25 % of the energy is lost as waste heat[24], globally more than 54 % of industrial power plants energy is lost [25], and 60 % of the energy produced in the US is rejected [26].

Thermoelectric devices can enhance energy efficiency by converting waste heat directly to useful electrical energy. Possible applications for this gas-emission-free solid-state technology include deep-space missions, industrial waste heat recovery, and automotive implementations [27, 28]. In passenger cars about 60% of the energy is lost, approximately $\frac{2}{3}$ of it as waste heat. The European Union set the amibitious goal to reduce CO_2 emission in passenger cars from 130 g/km in 2015 to 95 g/km by 2021 [29]. The recovery of waste heat of an automotive exhaust pipe can be re-used for example to provide electricity for avionics.

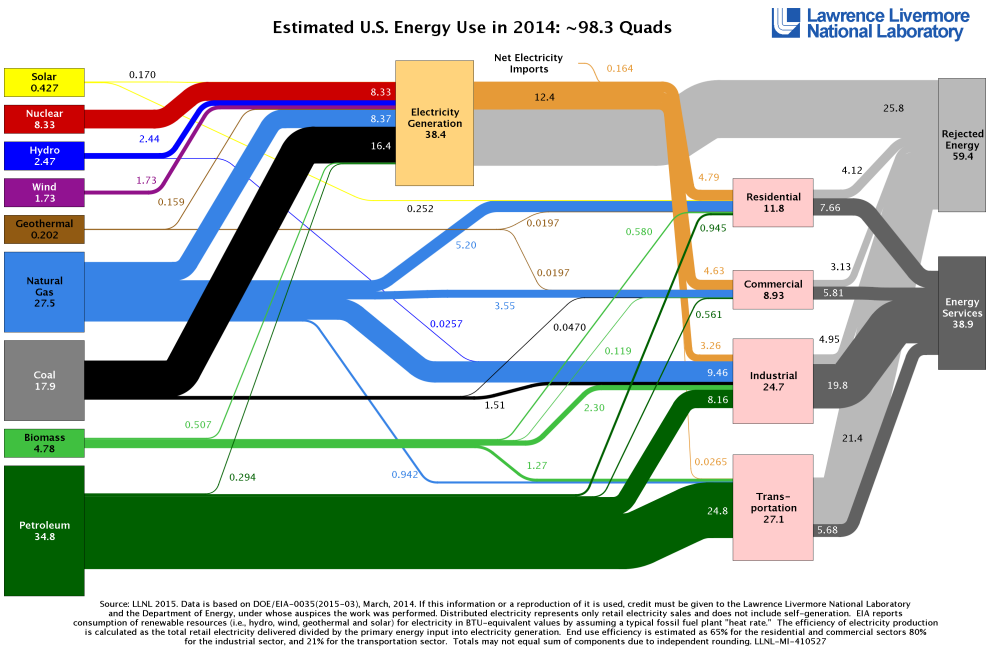

Figure 3.1: US energy flow chart 2014 released by Lawrence Livermore National Laboratory. Displayed are sources of energy production, how Americans used the energy and how much was rejected as waste heat [26].

A thermoelectric generator (TEG) consisits of pairs of n- and p-type semiconducting materials, that are connected electrically in series (see Figure 3.2(a)). Those are sandwiched between two electrically insulating but thermally conducting ceramic plates to form a module. If the TEG is connectequiled to an external load and a temperature gradient is applied, electric energy is generated. Vice versa, if an electric current is passed through the module, heat is absorbed on one side and ejected at the other. In this case the module can be used for refrigeration (Peltier cooling). Physical foundation for the energy conversion is the Seebeck effect (or Peltier effect for cooling). Simply put, the charge carriers at the hot end of the semiconductor, possess more thermal energy and consequently diffuse into the material towards the cold end. This generates an electrical potential until the equilibrium is reached. If n- and p-type materials are connected in series and a load is inserted an electrical current is produced due to the thermal gradient [28, 30–34].

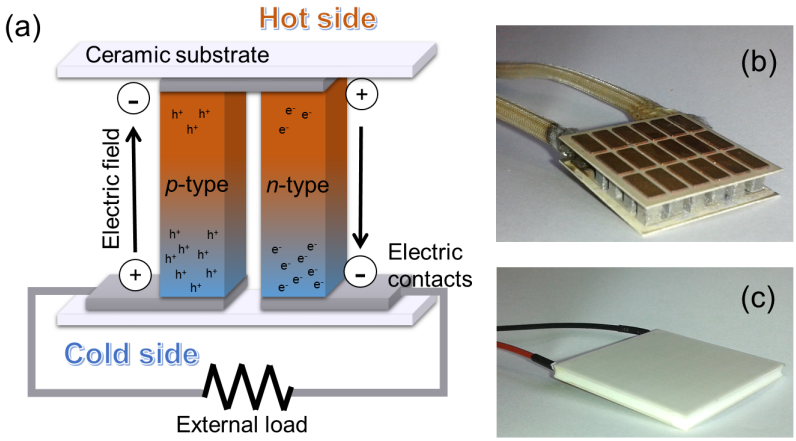

Figure 3.2: (a) Schematic drawing of one couple of a TEG. Adapted from [28, 35] (b) Test-Modules fabricated from half-Heusler compounds by the Frauenhofer Gesellschaft, Freiburg [36] (c) Commercially available TEG fabricated by thermalforce.de (TEG 127-200-24).

The efficiency of a TEG is defined as the power input to the load over the net heat flow rate. It depends on the thermal gradient ΔT, the average operation temperature T, and the performance of the TE material. The maximum efficiency of a TE device is given by [6, 32, 33]:

$$\eta_{TE} = \frac{T_H - T_C}{T_H} \frac{\sqrt{1+\overline{ZT}}-1}{\sqrt{1+\overline{ZT}}+\frac{T_C}{T_H}} \tag{3.1}$$

Thermodynamically the efficiency is limited by the Carnot efficency $\eta_C = \frac{T_H - T_C}{T_H}$. T_C and T_H are the temperatures at the cold and hot side of the module, respectively. $\overline{ZT}$ here denotes the average effective device figure of merit, which is equal to the materials

figure of merit ZT, if the n- and p-type material are matched, meaning they posess identical TE properties (Seebeck coefficient, electrical conductivity and thermal conductivity). Compatibility of n- and p-type material is an important issue when optimizing the device efficiency [32].

The thermoelectric effect was first discoverd by *T. J. Seebeck* in 1821. He found that a circuit of two disssimilar metals with junctions at different temperatures is deflecting a compass needle [37]. An electrical current is generated and therefore deflecting the compass needle according to Ampère's circuital law. Seebeck's systematic investigations of a number of metals and ores lead to a systematic ordering according to their relative Seebeck effect [38].

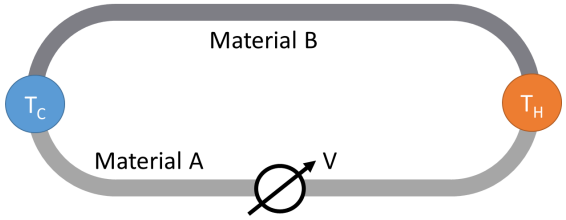

Figure 3.3: Experimental set-up to observe the Seebeck effect. Two metals (Material A and B) are connected in series and one junction is heated (T_H) and the other cooled (T_C).

Figure 3.3 shows the most simple experimental set-up to observe the Seebeck effect. The voltage produced is proportional to the temperature gradient by the Seebeck coefficient S (also known as the thermopower) [30, 31, 35, 39].

$$V = S\,(T_H - T_C) \quad \curvearrowright \quad S = \frac{V}{\Delta T} \tag{3.2}$$

The reversed effect was discoverd by *J. Peltier* 13 years later. If a electrical current is passed trough the experimentel set-up, one junction is heated and the other cooled. The ratio between transported heat Q to electric current I is called Peltier coefficent Π [30, 31, 35, 39].

$$\Pi = \frac{Q}{I} \tag{3.3}$$

The interrelation between Peltier and Seebeck effect ($\Pi = TS$) was found by *W. Thomson* in 1851 [30, 31, 35, 39]. He also predicted and observed a third thermoelectric effect: Heating or cooling of a single homogeneous conductor when a current passes along in the presence of a temperature gradient (Thomson effect).

Finally, the dimensioneless figure of merit ZT, as a measure for the quality of TE performance of a material, was introduced by *Altenkirch* in 1911 [39–41].

$$ZT = \frac{S^2\sigma}{\kappa}\,T \tag{3.4}$$

where S is the Seebeck coefficient , σ the electrical conductivity, κ the total thermal conductivity, and T the absolute working temperature. A high electrical conductivity for minimum internal resistance, high Seebeck coeficient for maximum voltage and therefore power output, and low thermal conductivity for maintaining a maximum temperature are required.

The indroduction of several concepts were important stepping stones towards the ultimate goal of maximizing ZT: *Ioffe* promoted the use of semiconductors and a reduction of lattice thermal conductivity by point defects through allyoing in solid solutions [42, 43]. In 1954, *Goldsmith* highlighted the importance of high mobility and effective mass combination and low lattice thermal conductivity by the investigations of Bi_2Te_3 [44]. The Phonon-glass electron-crystal (PGEC) concept was introduced by *Slack* [45] reflecting the idea of optimum electronic properties and minimum thermal conductivity in one material. *Hicks* and *Dresselhaus* predictions for enhancing the TE performance of Bi_2Te_3 due to confinement of electron charge carriers in quantum-well superlattice strucures in the early 1990s [46], pushed the field towards nano-engenieering of 2D superlattices and later on to 3D nanostrutured bulk materials [47, 48].

Nowadays, TE materials are in focus of research due to the search for sustainable and environmental friendly energy production. Depending on the application purposes (cooling or electrical generator), different requirements have to be fulfilled by the TE materials. The maximum ZT should peak within the temperature range of operation. Figure 3.4 provides an overview of state-of-the-art materials for different temperature ranges. For low tempratures (RT to 200°C), Bi_2Te_3 systems are commonly used[49, 50], for very high temperature (> 800°C) SiGe alloys are employed. [55, 56] At moderate temperatures, such as in industrial waste heat and automobiles (T = 500 – 800 °C), among other materials, like e. g. lead chalcogenide PbSe/PbTe alloys [51, 52, 60], $(GeTe)_{0.85}(AgSbTe_2)_{0.15}$ (TAGS) [31] and skutterudites [53, 54], half-Heusler compounds have recently gained attention as promising materials for TE applications. [1–5]

Apart from the simple quest for maximizing ZT, other issues like compatibilty of the n- and p-type materials [32, 61], long-term stability under operating conditions, environmental friendlines, material cost per kg, and mechanical strength have to be adressed for the fabrication and application of modules.[6, 62] The previously very ambitous goal of $ZT = 4$, which corresponds to 30% of the carnot efficiency [27, 33, 63] has been diminished for mid-temperatue applications to a benchmark of $\overline{ZT} \geq 1$ of the n- and p-type material couple for the sake of low cost, low toxicity and co-processability of the n- and p-type materials [6, 27, 36, 64].

3.2 Transport properties of TE materials

The relevant transport properties of a TE material are summarized in its figure of merit ZT (see Equation 3.4) . Desirable are high electrical conductivity σ and Seebeck coefficients S, and low thermal conductivity κ, consisting of a lattice component κ_{lat} and an electronic component κ_{el}. Unfortunately, all these physical properties are interde-

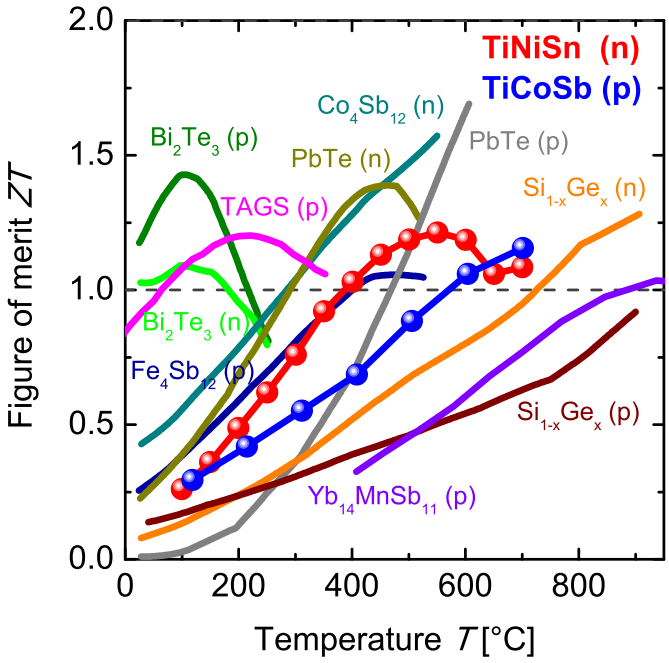

Figure 3.4: Overview of state-of-the-art TE materials. Adapted from [6, 32, 34]. The exact compositions are as follows: BiTe (n): $Cu_{0.01}Bi_2Te_{2.7}Se_{0.3}$ [49] and (p): $Bi_xSb_{2-x}Te_3$ [50] , Pb-Te (n): $PbTe_{0.9988}I_{0.0012}$ [51] and (p): $K_{0.02}Pb_{0.98}Te_{0.15}Se_{0.85}$ [52], Skutterudites (n) $Ba_{0.08}La_{0.05}Yb_{0.04}Co_4Sb_{12}$ [53] and (p) $Ce_{0.45}Nd_{0.45}Fe_{3.5}Co_{0.5}Sb_{12}$ [54], Si-Ge (n): $(Si_{95}Ge_5)_{0.65}(Si_{70}Ge_{30}P_{30})_{0.35}$ [55] and (p): $(Si_{80}Ge_{20})_{0.8}(Si_{100}P_3)_{0.2}$ [56], $Yb_{14}MnSb_{11}$ (p) [57], TAGS $(GeTe)_{0.85}(AgSbTe_2)_{0.15}$ (p) [58]. Higlighted are half-Heusler compounds n-type $Ti_{0.5}Zr_{0.25}Hf_{0.25}NiSn_{0.998}Sb_{0.002}$ [14], and p-type $Ti_{0.25}Hf_{0.75}CoSb_{0.85}Sn_{0.15}$ [59].

pendent and cannot be manipulated separately. Therefore, the maximization of ZT is challenging.

3.2.1 Electronic properties

The demands on the electronic properties for a good TE material are summarized in the power factor, defined as the product $S^2\sigma$. High Seebeck coefficients S as well as high electrical conductivity σ are desirable. Additionally, the electronic contribution to the thermal conductivity κ_{el} depends on the electronic properties of a material. This is discussed in Chapter 3.2.2.

Starting point for a discussion of the electronic transport properties is the distributions of electrons in a solid that is given by the Fermi-Dirac statistics [65]:

$$f_0 = \frac{1}{exp\frac{E-\mu}{k_B T} + 1} \tag{3.5}$$

The propability f_0 of occupying an electron state at a given energy E depends on the chemical potential μ that is equal to the Fermi energy at T = 0 K, or accordingly for $T \geq 0K$, $E \approx E_F$ is estimated. The electronic properties of a solid can be described by the Mott formula, which is obtained from the Boltzman equation by using a single parabolic band approximation [32, 33, 66–69]:

$$S = \frac{\pi^2 k_b^2}{3e} T \left\{ \frac{d\left[ln\left(\sigma(E)\right)\right]}{dE} \right\}_{E=E_F} \tag{3.6}$$

with e elementary charge, and $\sigma(E)$ electrical conductivity, that is a function of the energy E, at the fermi level E_F. For infinitesimal small energy steps dE the slope of $\sigma(E)$ is proportional to the densitiy of states (DOS) and therefore the term $d\left[ln\left(\sigma(E)\right)\right] dE$ is equal to the slope of the DOS at the Fermi level [32, 33, 69, 70].

The electrical conductivity depends on charge carrier concentration n and mobility μ [32, 71]:

$$\sigma = ne\mu \tag{3.7}$$

Combining those two equations leads to:

$$S = \frac{\pi^2 k_b^2}{3e} T \left\{ \frac{1}{n}\frac{dn(E)}{dE} + \frac{1}{\mu}\frac{dn(E)}{dE} \right\}_{E=E_F} \tag{3.8}$$

This demonstrates the fundamental conflict towards optimizing the power factor of TE materials. High n leads to high σ but low S and a compromise has to be found [32, 33, 48]. Metals have a high carrier concentration ($n \geq 10^{22} cm^{-3}$) and $\sigma \geq 10^6 S/m$. Insulators have low n and low σ ($\leq 10^{12} S/m$) but high S. In between those two extremes, are semiconductors with n in the range from $10^{18} cm^{-3}$ to $10^{21} cm^{-3}$ and σ in the range 10^{-7} Sm^{-1} to 10^0 Sm^{-1} [71]. Intrinisic or non-degenerate semiconductors usually have a low carrier concentration and hence $S \propto \frac{1}{ln(1/n)}$. Degenerate or highly doped semicondoctors with a high carrier concentration can be considered to act like a metal. Assuming pure acoustic phonon scattering of carriers, the Seebeck coefficient is given by [32]:

$$S = \frac{8\pi^2 k_b^2}{3eh^2} m^*_{DOS} T \left(\frac{\pi}{3n}\right)^{2/3} \tag{3.9}$$

The effective mass of the charge carriers m^*_{DOS} is calculated from the DOS and varies inversly with the curvature of the bands [72]. Flat shallow bands with a small band curvature lead to a high DOS at the Fermi level and therefore high m^* and high S. However, those heavy carriers move with a low velocity leading to a small σ. Also highly dispersed bands can lead to a high m^* [33]. Whereas for the carrier concentration a clear optimum can be found for each material (compare Chapter 7) within the range of heavily doped semiconductors, good TEs with a large variety of m^* and μ exist [32].

The size of the band gap in semiconductors also influences the thermopower. The sign of S is determined by the type of charge carriers in the material. If holes and electrons are present, bipolar conduction occurs and the Seebeck coeeficient is diminished [30, 31]:

$$S = \frac{S_e\sigma_e + S_h\sigma_h}{\sigma_e + \sigma_h} \tag{3.10}$$

Bipolar conduction plays a role for small band gap materials and at high temperatures. In materials with small band gaps, more minority carriers can be excited thermally from the valence to the conduction band and contribute to the transport. This cancels out the Seebeck voltage. Consequently highly doped semiconductors with one predominant carrier type are desirable for a large thermopower [32, 33]. For high temperature applications usually $E_G \geq 0.5$ is required due to the late onset of bipolar conduction whereas materials with small bandgaps are rather used for cooling applications [73].

3.2.2 Thermal conductivity

The thermal conductivity is defined as the heat flux vector $\vec{Q}$ across a unit cross section perpendicular to $\vec{Q}$ in presence of a temperature gradient $\vec{\nabla}T$ [74, 75]:

$$\kappa = -\frac{\vec{Q}}{\vec{\nabla}T} \tag{3.11}$$

Heat energy in solids can be transported by electrical carriers (holes or electrons), lattice waves (phonons), electromagnetic waves, spin waves, or other excitations. The various excitations α in a solid can be treated with a simple kinetic gas theory and can be added up to the total thermal conductivity [74, 75]:

$$\kappa = \frac{1}{3}\sum_{\alpha} C_\alpha v_\alpha l_\alpha \tag{3.12}$$

C_α denotes the total heat capacity and l_α the particle mean free path $l = v\tau$, respresenting the average distance a particle travels with velocity v before it is scattered after its relaxation time τ. Since these are non-equilibrium transport parameters, this equation cannot be solved exactly. Calculations are based on a combination of pertubation theory and Boltzman transport equation. Microscopic processes that govern the heat conduction in solids arise from charge carriers and lattice waves [75].

In metals electrical carriers are the dominant heat transporters, whereas in insulators lattice waves are the main heat carriers. For semiconductors the lattice part(κ_{lat}) and electrical part (κ_{el}) of the thermal conductivity have to be considered [32, 33, 75]:

$$\kappa = \kappa_{lat} + \kappa_{el} \tag{3.13}$$

The magnitude of the thermal conductivity as well as its temperature dependence varies drastically depending on the materials properties. Additionally, κ is sensitive to any kind of lattice defects or imperfections, dislocations, anharmonicity of the lattice forces, carrier concentrations, interaction between carriers and phonons, or magnetic ions

and phonons. The limited sample size in single crytals or grain sizes in polycrystalline samples leads to thermal resistance by boundary scattering [75, 76].

Electronic thermal conductivity

In metals the electronic thermal conductivity κ_{el} can be estimated by a free electron theory (degenerate electron gas). Each electron moves in a periodic potential, produced by the ions and other electrons. Vibrations of the lattice, which lead to a deviation from this periodicity, are treated as pertubations.

Solving the Boltzman transport equation, leads to the Wiedemann-Franz law [75, 77]:

$$L_0 = \frac{\kappa_{el}}{\sigma T} = \frac{\pi^2}{3}\frac{k_B^2}{e^2} = 2.4453 \times 10^{-8} W\Omega K^{-2} \tag{3.14}$$

All metals have an identical ratio (Lorentz number L_0) of electronic thermal conductivity to electrical conductivity, that is proportional to the absolute temperature. This law is well obeyed at high temperatures and at very low temperatures. In the intermediate regions, inelastic scattering processes have to be taken into account.

Good thermoelectric materials are typically highly doped semiconductors. The ratio $\frac{\kappa_{el}}{\sigma T}$ is consequently not a constant and rather complicated to work out [75]. It can deviate significantly from the degenerate limit (up to 40%). Hence it is common practice to estimate L_0 with the constant for metals given in equation 3.14. Very recently, *Kim et al.* proposed a elegant way to estimate the Lorentz number from the Seebeck coefficient S in μVK^{-1} as a first order correction [78]:

$$L = 1.5 + exp\left[-\frac{|S|}{116}\right] \times 10^{-8}\ \mathrm{W\Omega K^{-2}} \tag{3.15}$$

This equation has been demonstrated to be accurate within 5% for the SPB-AS model. and provides a much better approximation than utilization of the constant L_0 for TE materials.

Additionally, one should keep in mind, that bipolar diffusion due to the creation of electron-hole pairs can occur in semiconductors. This is extracting a certain amount of energy at the high-temperature end and leads to an increase in κ. Especially if carrier concentration and mobilities of both carriers are about equal, like it is the case in intrinsic semiconductors (compare also Chapter 3.2.1). In highly doped semiconductors, like most thermoelectric materials, only one carrier has high mobililty and this effect is usally not noticable [30, 75].

Lattice thermal conductivity

In non-metals, thermal transport by phonons is the main conduction mechanism, also in semiconductors and alloys it dominates over a wide temperature range. Phonons are quanta of the crystal vibrational field. The thermal energy is propagating in the presence of a temperature gradient by means of wave packets consisting of various normal modes

(= phonons). The main heat conductors are acoustic phonons (harmonic, low frequency, atoms in the unit cell are moving in phase). Optical phonons (anharmonic, higher frequency, atoms move in opposite phases) are not effective in transporting heat because of their low velocity, but their interaction with acoustic phonons can be relevant [75].

A good approximation for the lattice thermal conductivity is derived from classical kinetic theory (compare 3.12) [74, 75]:

$$\kappa_{lat} = \frac{1}{3} C_v l v_s \tag{3.16}$$

C_v denotes specific heat with constant volume V, l is the mean free path of the phonons, and v_s the speed of sound.

A similar expression can be optained, starting from the phonon distribution function, that describes the average number of phonons $N^0_{\vec{q}}$ with a wave vector $\vec{q}$ and frequency $\omega_{\vec{q}}$ in equlilibrium by Bose-Einstein statistics (see Equation 3.17), and Boltzman transport theory [74, 75]:

$$N^0_{\vec{q}} = \frac{1}{exp\left(\hbar\omega_{\vec{q}}/k_B T\right) - 1} \tag{3.17}$$

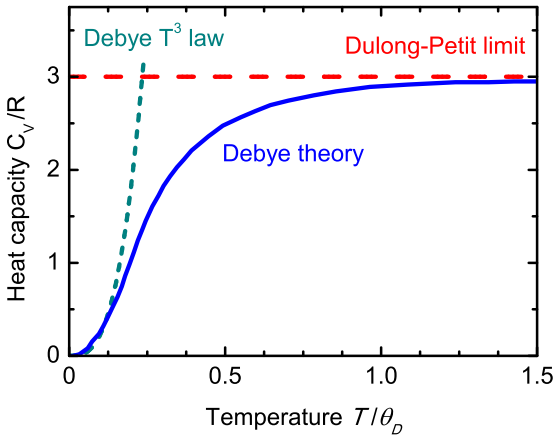

Figure 3.5: Debye theory for specific heat of solids. At high temperatures the Dulong-Petit limit is reached, at low temperatures the Debye T^3 law is valid.

Debye [79] assumed an average phonon velocity that is equal to the velocity of sound for all phonon branches and defined the Debye frequency, as a cut off such that the total number of distinguishable phonon modes is equal to 3 times the number of atoms in the solid ($3N = \int_0^{\omega_D} f(\omega) d\omega$) [74]:

$$\kappa_{lat} = \frac{3k_B}{2\pi^2 \nu} \left(\frac{k_B}{\hbar}\right)^3 T^3 \int_0^{\Theta_D/T} \tau_q(x) \frac{x^4 e^x}{(e^x - 1)^2} dx \tag{3.18}$$

The Debye temperature is defined as $\theta_D = \hbar\omega_D/k_B$. The differential lattice specific heat within the Debye approximation is accordingly [30, 74]:

$$C(x)dx = \frac{k_B}{2\pi^2\nu^3}\left(\frac{k_B}{\hbar}\right)^3 T^3 \frac{x^4 e^x}{(e^x-1)^2}dx \tag{3.19}$$

From this expression the T^3 dependence of the heat capacity of solids at low temperatures ($T \leq 40$K) is obvious. In this region phonon-phonon scattering is not relevant because of the small number of excited phonons and the very large wave number. At high temperatures ($T \geq \Theta_D$) the values approach the classical value of the Dulong-Petit law [30, 74].

$$C_V = 3R \tag{3.20}$$

The lattice thermal conductivity κ_{lat} therfore mainly depends on the phonon mean free path l, which can be dominated by phonon-phonon interaction.
Within the Debye model a sufficient describtion of crystalline solids is usually optained, at high temperatures the Dulong-Petit limit is a valid estimation for the heat capacity of solids.

3.2.3 Strategies to enhance the thermoelectric performance

Carrier concentration optimization

One basic approach to enhance the electronic properties and consequently ZT is to optimize the carrier concentration n [31, 32, 48]. Increasing n increases the electrical conductivity σ but decreases the Seebeck coefficient S while simultaneously increasing κ_{el}. Thus, a compromise for high power factors $S^2\sigma$ has to be found. Only the lattice thermal conductivity κ_{lat} can be manipulated individually, since it does not depend on the electronic structure [80] (see Chapter 3.2.2). The maximum of ZT typically occurs at carrier concentrations between 10^{19} and 10^{21} carriers cm^{-3} (depending on the material system), which is found in heavily doped semiconductors [32].

Excellent graphical illustrations of the interdependence of those parameters are found in review articles. For example, Snyder and Toberer [32] modeled the trends for Bi_2Te_3 on the basis of empirical data, and Minnich et al. examined n-type $Si_{80}Ge_{20}$ [48]. Hence, the basic concept of carrier concentration optimization is well known. It can be easily realized by electron or hole doping of thermoelectric n- or respectively p-type materials.

Band structure engineering

The band structure of a semiconductor has a significant impact on the carrier concentration and efective mass of the carriers. For metals and degenerated semiconductors as simple single parabolic band model can be applied. The slope of the densitiy of states (DOS) $f(E) \propto \sqrt{E}$ is flatter the further the Fermi energy lies within the conduction band. Consequently, E_F shifts less with temperature when electrons move from the valence band (VB) to the conduction band (CB) leading to enhanced S [65].

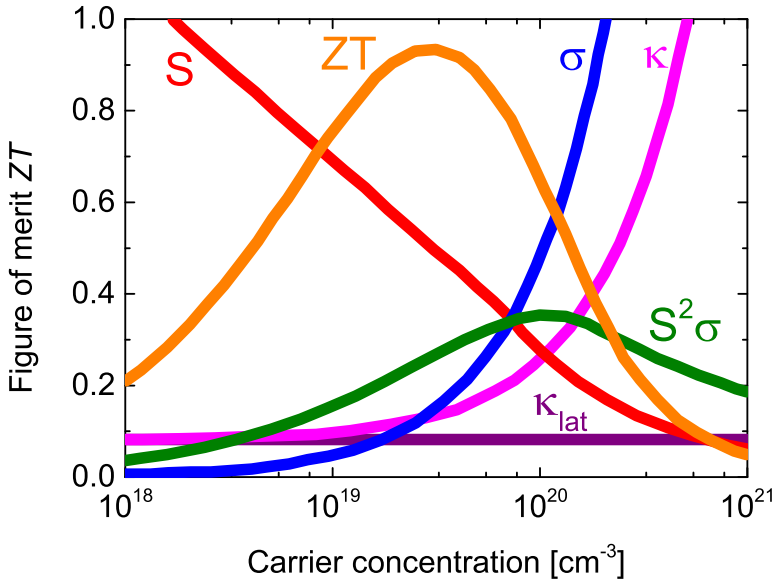

Figure 3.6: Carrier concentration optimization for a high figure of merit ZT. Adapted from reference [32].

In reality, TE materials exhibit more complex band structures, especially if atoms with valence electrons in d- or f- orbitals are included in the crystal structures [10, 33, 68, 81–84].

Figure 3.7 shows a favorable band structure for TEs. Electron states at E_F enable a desired electron flow. Sharp features at the edge of the valence band (VB) serve as an electron reservoir and lead to a steep slope of the VB at the fermi energy. Many thermally excited electrons have to occupy states above E_F. This leads to a huge change in chemical potential between cold and hot end of the TE material and therefore high seebeck voltages, plus a much higher electron mobility in the bands above E_F [81, 83–85].

As discussed in Chapter 3.2.1 steep slope of the DOS at the fermi level leads to a high Seebeck coefficient S. Also a complex band structure is beneficial to obtain large ZT. For n-type many minima in the conduction band, whereas for p-type many maxima in VB are beneficial. A theoretical description has been provided by *Mott* [69]. As a simplification one can imagine that each extremum of a occupied band contributes a certain amount to the thermopower and electrical conductivity [33].

$$Z_{max} \propto \gamma \frac{T^{3/2}\tau_z \sqrt{\frac{m_x m_y}{m_z}}}{\kappa_{lat}} e^{r+1/2} \tag{3.21}$$

with γ degeneracy of the extrema of the bands, m_i effective mass of the charge carriers in direction i, τ_z relaxation tion of the charge carriers that are moving in direction z, r bowing parameter.

Materials with high degeneracy at the VB edge, which can occur if fermi pockets are

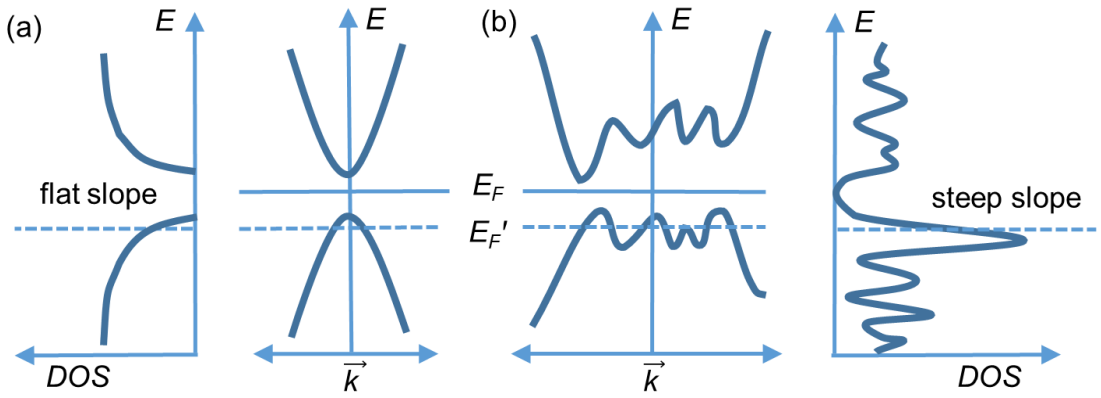

Figure 3.7: Bandstructure and DOS of semiconductors. The Fermi energy E_F is shifted in the valence band upon doping with holes indicated by E'_F. Comparision of single parabolic band model (a) with a favorable band structure for TEs (b). Adapted from [33, 66, 72].

generated at low symmetry points, lead to enhanced TE performance [83]. In particular, the effect of band structure engeneering on the TE performance of PbTe has been studied intensively [82, 83]. Heremans concept of resonant states also exploits this concept by creating sharp features of the band structure close to the fermi level by means of doping with impurity atoms [6, 68, 83–85]. Hence, adjusting the band structure by changing the slope and band degeneracy is a powerful tool to enhance the TE performance. Nevertheless, predictions are difficult and systematic experimenental investigations are not easily realized, since the degenaracy of bands can only be changed by also changing the crystal structure.

Lattice thermal conductivity

The electronic contribution to total thermal conductivity is related to the electrical conductivity by the Wiedemann Franz law, and can not be influenced separately. In contrast, the lattice thermal conductvity can be manipulated individually.

The ideal goal is demonstrated by the phonon glass electron crystal (PGEC) concept introduced by *Slack* [45]. In amporphous materials, like glasses, a minimum thermal conductivity is obtained since a rapid transport via phonons is not possible due to the lack of a long-range order. Heat is transported by a random walk of energy through the solid. On the other hand, this lowers the mobility of the charge carriers due to the increased electron or hole scattering as well as the effective mass because of broader bands. An ideal TE material consequently would combine electron crystal properties with a phonon glass. In materials with large unit cells, the mean free path of phonons is shortened because of the long and complicated way through the unit cell. The closest realization of the PGEC concept is achieved by rattlers in cages. In complex crystal structures, like clathrates and skutterudites, "guest atoms" are included, which "rattle"

upon thermal excitation and lead to a damping of the phonons [32, 33]. Succesful examples are Zintl compounds [57, 86–88], Skutterudites [35, 53, 89–92] and Clathrates [93–95].

A second approach is to start from a crystalline semiconductor with good electronic properties and reduce κ_{lat}. By creating point defects in solid solutions, like interstitials, vacancies or side substitution (alloying) with isoelectronical elements, disorder scattering is introduced. A large mass contrast is disrupting the phonon path, while the crystaline structure is preserved. Another way to reduce κ_{lat} is by boundary scattering, the phonons are scattered at artificially createted interfaces on the nano or micrometer-scale [32, 33, 96]. This can be realized either in multiphase composites mixed on the nanometer scale [47], by thin film superlattices [97–99] or intimately mixed composite structures [100, 101]. A very common approach is the nanostructuring process of bulk materials with already good electronic properties via ball milling followed by a rapid consolidation method like spark plasma sintering or hot pressing. For half-Heusler materials recently a microstructuring via intrinsic phase separation has come into focus of research. This is discussed in the following Chapters 3.3 and 3.4.

3.3 Phase separation

The concept of intrinsic phase separation to reduce the lattice thermal conductivity of half-Heusler compounds and improve their thermeoelectric performance is one of the key features of this work. An intrinsic microstructuring can be achieved via eutectic growth by rapid cooling from the melt.
Heat and mass transport (diffusion) are crucial factors during (alloy) solidification processes and determine the microstructuring. In the field of materials science, microstructural analysis is a key feature, since the macroscopic properties depend strongly on the microscopic structure. Developed historically from physical metallurgy, like processing of steel, nowadays the field expanded to engineering of novel functional materials, like ceramics, plastics, and electronic materials [102]. To understand the soldification and crystallization processes in metals and alloys a basic knowledge of thermodynamic principles and phase diagrams is essential [30, 102–105].

Depending on the material system and the desired structural properties and applications, a suittle processing procedure has to be chosen, usually followed by a heat treatment of the as-cast materials in order to improve the crystal orderering and reduce strain [30]. In particular, bulk half-Heusler compounds are conventionally prepared by arc melting or by mechanical alloying via high energy ball milling followed by a rapid consolidation method like spark plasma sintering or hot pressing [7, 107, 108].

The rate of temperature deduction during the solidification process from the melt determines the shape of the microstructuring. The emitted heat of fusion can be dissipated eighter via the liquid or solid phase, depending on the temperature gradients at the interfaces. Fast heat dissipations within the solid phase, results in a uniform crystal growth with sperical grains, whereas slow heat dissipations, e. g. in super-cooled melts, leads to

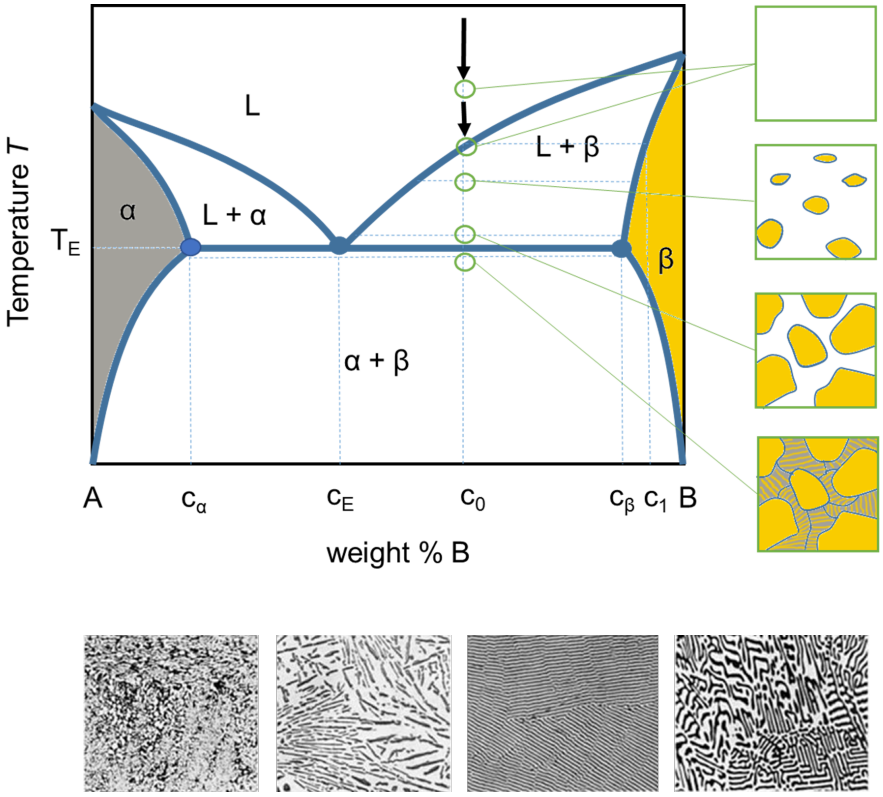

Figure 3.8: Eutectic phase diagram and evolution of the microstructure during the solidification process of a hyper-eutectic alloy. Adapted from [102, 103]. Examples for typical eutectectic rres in binary alloys are illustrated at the bottom (200× magnification). Displayed are 40Sn-50In (globular structure), Al-13Si (acicular structure), Al-33Cu (lamellar structure), Mg-37Sn ("Chinese-script") from left to right [106].

a unstable solidification front and the formation of dentrites [102, 103]. If two or more constituents are alloyed, phase diagrams have to be considered. Information about which thermodynamically stable phases are obtained from the melt can be gained [106, 109]. Particulary, composite materials by eutectic structuring can be designed. The benefit of ternary eutectic growth has already been successfully demonstrated for other TE materials, like nanostructured Ag-Pb-Te [110], microstructured PbTe-Sb_2Te_3 composites [111] and spinodal demixing in $Ge_{0.6}Sn_{0.1}Pb_{0.3}Te$ [112].

In the undoped TiNiSn half-Heusler alloys a spontaneus demixing in a Ni-rich TiNiSn and Ni-deficient $TiNi_2Sn$ full-Heusler phase can be observed [113]. Half-Heusler compounds, that are relevant for thermoelectric applications, consist of three up to five or six different elements. However, in phase-separated samples, mostly a seperation in two stable phases is observed, as demonstrated for the *n*-type (Ti/Zr/Hf)NiSn system by

Schwall [114], *Krez* [115], and *Schmitt* [116], for $TiCo_{1-x}Mn_xSb$ by *Graf et al.* [117], and for (Ti/Zr/Hf)$CoSb_{1-x}Sn_x$ in the present work.

Accordingly, the processes during solidification can be considered as a pseudo-binary system. A microstructuring that is typical for eutectics is observed (compare Figure 3.8). The miscibility gap between the compositions leads to a dentritic microstructure. The experimental results were recently confirmed by theoretical calculations by an abinitio based mean-field model which provides phase diagrams of the alloys by *Mena et al.* (Ti,Y)CoSb materials (Y = Sc, V, Mn, Fe) show a miscibility gap, which leads to spontaneous demixing within a spinodal region [118].

The solidification process can therefore be explained with the help of an eutectic phase diagram (see Figure 3.8). The eutectic reaction is defined as a simoultaneous precipitation of two or more phases via a eutectic reaction:

$$L \longleftrightarrow \alpha + \beta \tag{3.22}$$

A melt with the eutectic composition c_E is solidified into a solid with widely different morpholigies (see Figure 3.8). Normal eutectic growth, meaning that the two phases grow at the same rate and with a close cooperation and hence with a common interface in the melt, results in lammelar or rod-shaped structures. In contrast, if no cooperation between the phases exists and one grows faster (degenerate eutectic mechanism), the structuring is determined by the growth mechanism of the faster growing phase. The kinetics at the interface are the crucial factor for the growth mechanism [103].

If a melt with hyper-eutectic composition ($c_\beta \geq c_0 \geq c_E$) is cooled, first the solid solution phase β with composition c_1 grows, when the liquidus temperature is reached. Consequently the composition of the melt is depleted in element B. When the eutectic temperature T_e is reached, the melt immediately solidifies in the phases α and β in the typical eutectic structure. Analogous process occur, when coooling a sub-eutectic composition c_0 ($c_\alpha \leq c_0 \leq c_E$).

In the (Ti/Hf)$CoSb_{1-x}Sn_x$ system two stable half-Heusler phases are formed. One rich in Ti and Sn (abreviated as TiCoSn for simplification) and the other rich in Hf and Sb (HfCoSb, matrix). By the rapid cooling during the arc melting process, first HfCoSb is solidified until the eutectic temperature is reached and then TiCoSn and the residual HfCoSb solidify suddenly in the eutectic structure. Since both have the same crystal structure, presumably a common interface during the solidfication process exists (normal growth mechanism). The greater the Hf content of the system, the greater is the amount of HfCoSb phase, and the less is the amount of TiCoSn phase. With this knowlede the microstructuring and lattice thermal conductivity can be engineered (compare Chapter 8).

3.4 Half-Heusler compounds as TE materials

Half-Heusler compounds have recently gained attention as promising materials for TE applications in the medium temperature range such as in the recovery of industrial and automotive waste heat [1–8]. The advantage of Heusler compounds are their excellent

electronic properties [7, 10] and high thermal and mechanical stability [5], as well as their low toxicity, elemental abundance and relatively low costs [6, 8, 9]. These are very important issues from the economical point of view.

3.4.1 Heusler compounds

In 1903 Fritz Heusler discovered an exciting material, Cu_2MnAl, that behaved like a ferromagnet even though non of its constituents is magnetic by itself [119, 120]. Since then a vast collection of more than 1000 compounds were discovered and Heusler compounds experienced a growing interest due to the huge variety and tunability of physical properties ranging from semiconductors over metals and magnets to topological insulators and superconductors, opening up a large field of applications, like spintronics, opto-electronics, magneto-calorics, magneto-electronic shape-memory and last but not least thermoelectrics [7, 121–124].

Heusler compounds are ternary intermetallic compounds consisiting of two transition metals X, Y and one main group element Z eighter in 2:1:1 stoichiometry or 1:1:1, which is also referred to as half-Heusler compounds. Their properties can be predicted by simple valence electron counting rules [121, 125].

As demonstrated in Figure 3.9 almost the entire periodic system can serves as a tool box for designing a material with the desired properties.

Two substructure types can be distinguished according to their composition:
Heusler compounds X_2YZ crystallize in the cubic $L2_1$ structure type ($Fm\bar{3}m$, space group no. 225, Cu_2MnAl prototype) [7, 120, 126–133]. Their crystal structure consists of four interpenetrating fcc sublattices. X occupies the $8c$ ($(\frac{1}{4},\frac{1}{4},\frac{1}{4})$ and $(\frac{3}{4},\frac{3}{4},\frac{3}{4})$) Wycoff positions, X $4a$ (0,0,0) and Z $4b$ $(\frac{1}{2},\frac{1}{2},\frac{1}{2})$. A rock salt structure is formed by the least and most electropositive element Y and Z and the tetrahedral holes are stuffed with X. Beyond that several disorder structure types are known, which impact the magnetic and transport properties [7].

Half-Heusler compounds XYZ crystallize in the non-centrosymmetric cubic $C1_b$ structure (MgAgAs-type, space group $F\bar{4}3m$ (216)) [7, 125, 134]. It can be derived from the $L2_1$ structure by removing half of the atoms on the $8c$ lattice side, so that only half of the tetrahedral holes are occupied with Y (Wycoff position $4c$ $(\frac{1}{4},\frac{1}{4},\frac{1}{4})$, leading to three occupied interpenetrating fcc sublattices.
Alternatively, it can be seen as zinc blende substructure ($F\bar{4}3m$) YZ and then stuffing the octahedral holes with X so that X and Z, or equivalently X and Y, form a rock salt structure [135]. Within the Zintl concept the chemical bonding can be described as a covalent zinc blende sublattice $[YZ]^{n-}$ filled with positive ions X^{n+}. This simple model applies well to the (8-N) valence electron (VE) compounds like LiAlSi. For $3d$ element containing compounds, the chemical bonding is a little more sophisticated, but qualitativly still in good agreement [7, 134, 136]. Nevertheless, with this molecular orbital approach the stability of 8 VE ($s^2 + p^6$) or 18 VE ($d^{10} + s^2 + p^6$) half-Heusler compounds can be explained, since in this case only the bonding orbitals in the $[YZ]^{n-}$ sublattice are occupied [7, 125]. These are closed shell, nonmagnetic and semiconducting

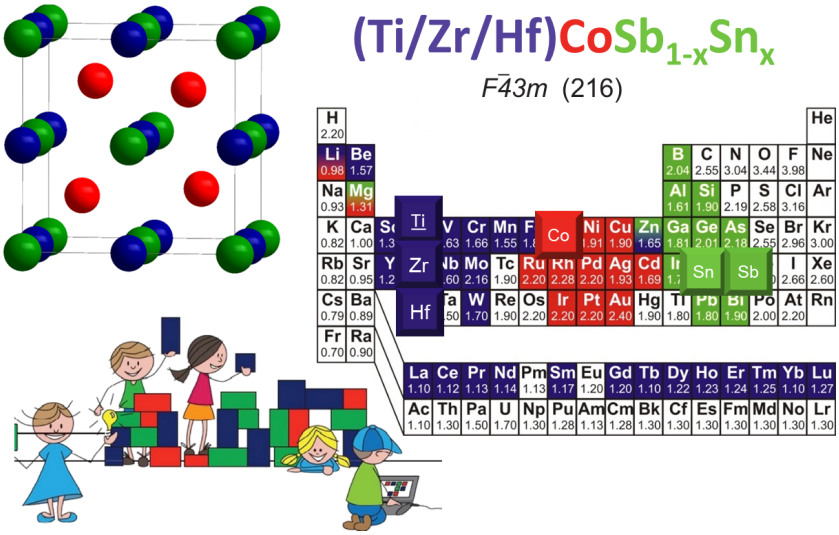

Figure 3.9: Crystal structure of half-Heusler compounds. According to the color code a huge variety of half-Heusler compounds can be formed from the periodic table of the elements. The highlighted TiCoSb system is investigated in detail. Two lattice positions were substituted: Sb with Sn for *p*-type doping and isoelectronic alloying of Ti with its heavier homologues Zr and Hf. Copyright 2003-2015, Max-Planck-Society, Munich.

or semimetallic compounds [137, 138].

3.4.2 Band structure considerations

The band gap of half-Heusler compounds can be tuned in a wide range by choosing compounds with appropriate hybridization strenght (by the lattice parameter) and magnitude of spin-orbit coupling (by the atomic charge) [139]. By choosing a suitable composition from the "tool box" presented in Figure 3.9 the band gap can be tuned from light Li-based members to gapless semiconductors containing heavy elements (Au,Pt,Sb, or Bi), with a zero direct gap at the Γ point making them possible candidates for topological insulators [7, 10]. The optimum band gap for TE materials is about $6k_BT$ to $10k_BT$ or sometimes even larger, depending whether the material exhibits a direct or indirect-band gap and on the specific mechanism of electron scattering. For applications in the mid-temperature range, the ideal band gap can be estimated with this formula to 0.57 eV to 0.86 eV at 1000 K [140–142].
18 VE half-Heusler compounds based on light transition metals e. g. TiNiSn, TiCoSb and VFeSb, exhibit exactly such a narrow band gap in the densitity of states (DOS). The size of the gap is related to a large extent to the hybridization between the *d*-states of the transition metals X and Y. In particular TiCoSb has an indirect band gap between Γ

and X point of 1.06 eV and a direct band gap at Γ of 1.83 eV [10], whereas for the indirect band gap in TiNiSn values between 0.45 eV [143–145] and 0.61 eV [146] are reported. However, the band gap is influenced by disorder. Structural disorder due to antiside defects leads to discrepancies of the calculated band gap from the experiment. This usally leads to an overestimation of the band gap by theoretical predictions [146, 147]. Additionally, antiside disorder leads to in-gap states close to the fermi level, comparable to resonant states. This explains, why ZrNiSn and TiCoSb are excellent TE materials and both intrinsically n-type semiconductors [10, 21, 33, 148].

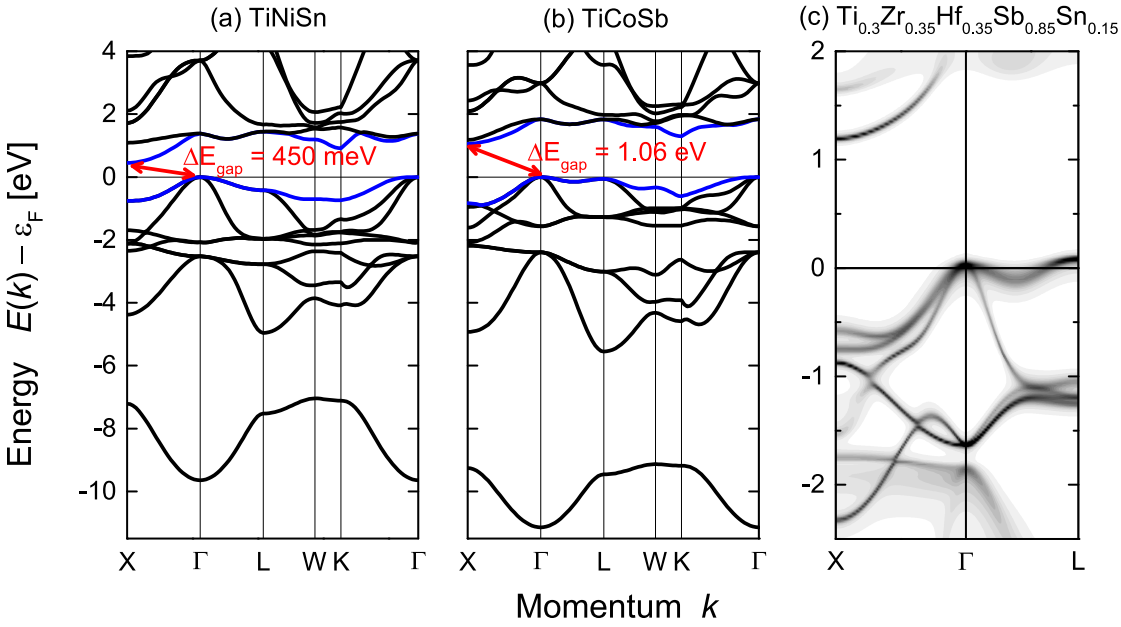

Figure 3.10: Electronic band structure of undoped (a) TiNiSn and (b) TiCoSb. Valence and conduction band are highlihgted in blue. Both are semiconductors with a indirect band gap ΔE_{Gap} from Γ to X. The effect of p-doping and allyoing in TiCoSb is displayed in (c). Note that a smaller section of the bandstructure was chosen. Ab initio calculations were provided by Dr. G. H. Fecher (MPI CPfS, Dresden), see References [10, 148] for details.

Consequently, TiCoSb is a much better starting material for p-type doping than TiNiSn. The larger band gap is beneficial to surpress the onset of bipolar conduction (see Chapter 3.2.1). No bipolar conduction is observed in the TiCoSb system up to 900 K, whereas the Seebeck coefficient in Sc doped ZrNiSn already shows a rollover around 600 K limiting the further enhancement by doping with holes [147].

Additionally, the band structure of TiCoSb exhibits several pockets with high degeneracy in the valence band (compare Chapter 3.2.1). Upon doping with holes the fermi level is shifted in this band, which leads to large positive Seebeck coefficents. Figure 3.10 (c) displays the effect of p-type doping and isolectronic allyoing on the band structure of TiCoSb. A composition with optimum Sn content was chosen (see Chapter 7). The

bands are smeared out due to disorder scattering of the charge carriers. Apart from that, the structure and degeneracy of the valance band remains intact, as well as the size of the band gap. The fermi energy is shifted into the valence band, crossing it twice at the Γ and L point. This is very favorable for a good TE performance leading to high σ and high S.

3.4.3 State-of-the-art

State-of-the-art half-Heusler compounds for TE applications in the mid-temperature range are based on the MNiSn system for the n-type and MCoSb for the p-type. M is either Ti, Zr, or Hf or a combination of these elements (see Figure 3.11). A great advantage of half-Heusler compounds is the possibility to substitute each of the three occupied fcc sublattices individually. This offers a huge variety of possibilities to enhance the TE performance. For example, it is possible to tune the number of charge carriers by substitution of the Z-position element by another main-group element and simultaneously introduce disorder by isolectronic alloying on the X- and Y-position elements resulting in mass fluctuations, which can decrease the thermal conductivity κ [7]. In general, half-Heusler compounds exhibit excellent electronic properties, reflected in high power factors in the range of 2–6×10^{-3}Wm^{-1}K^{-2} [6–9]. Thus, the main obstacle to further improving their TE performance is their relatively high thermal conductivity.

A record figure of merit ZT of 1.5 for the n-type (Ti/Zr/Hf)NiSn was already reported in 2005 [149, 150] Its outstanding TE efficiency can be explained by an intrinsic phase separation, as highlighted by *Schwall* and *Balke* in 2013 [14]. Ever since, the concept of an intrinsic phase separation to improve the TE performance of half-Heusler compounds has become a focus of research. In particular, the n-type (Ti/Zr/Hf)NiSn system has been investigated in this regard [11–16, 114–116] leading to several patent applications [17–20].

In contrast, the benchmark for state-of-the-art p-type material was for a long time ZT = 0.5 for a ingot of $Zr_{0.5}Hf_{0.5}CoSb_{0.8}Sn_{0.2}$ [21] reported by *Culp et al.* in 2008. A breakthrough was achieved by Yan et. al. in 2011 by a nanostructuring approach via ball milling followed by a rapid consolidation method, leading to 50 % reduction of lattice thermal conductivity, and almost doubling the ZT to 0.8 [2]. Further enhancements were achieved via this effective but elaborative, time and energy consuming synthesis route by isoelectronic substitution of Zr and Hf by Ti [3, 151].

This work investigates how the concept of phase separation can be applied to the p-type material system (Ti/Zr/Hf)$CoSb_{1-x}Sn_x$. Isolectronic alloying of Ti with its heavier homologues Zr and Hf can be used to introduce an intrinsic phase separation (see Chapter 3.3). Mandatory is the alloying of Ti with Hf, whereas Zr only plays a minor role. Second, the charge carrier concentration can be optimized by substitution of Sb with Sn. Previously, the best p-type half-Heusler compounds were achieved by a 20% substitution of Sb by Sn in MCoSb [2–4, 21, 22]. Yet, as demonstrated in Chapter 7, 15% Sn is the optimum. Based on these two concepts a fine tuning of the TE performance can be realized via adjusting the Ti to Hf ratio (see Chapter 8).

Meanwhile, the excellent compatibility of the herein presented p-type TiCoSb based

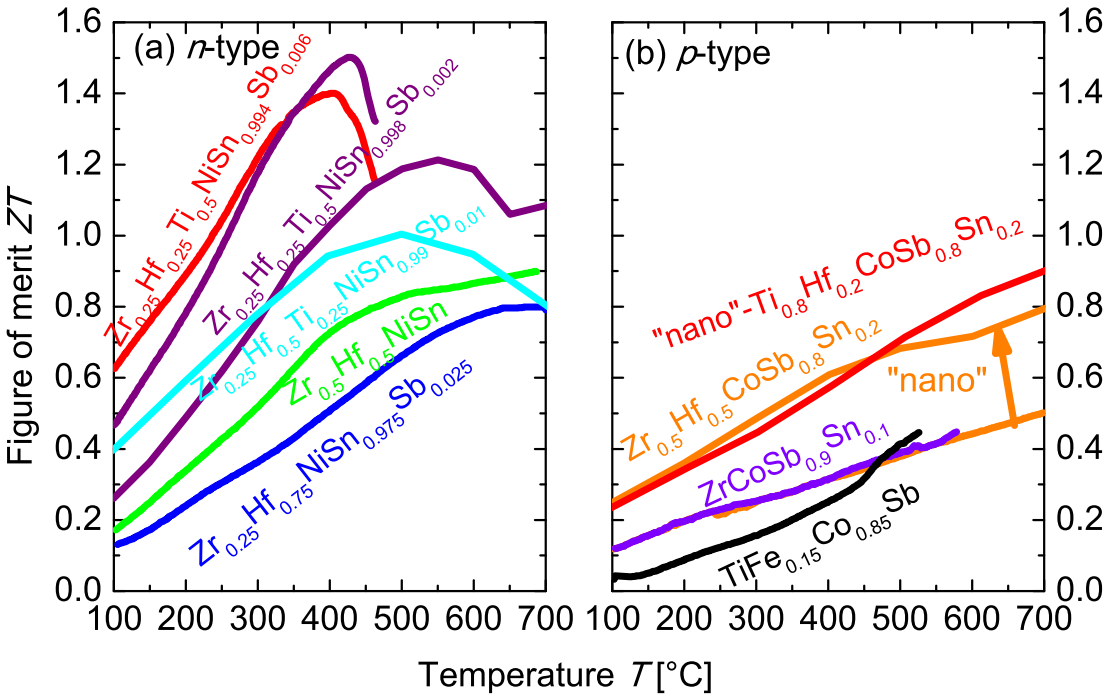

Figure 3.11: State-of-the-art half-Heusler compounds for TE applications dated 2012. (a) n-type based on TiNiSn [14, 149, 150, 152–154], (b) p-type based on TiCoSb [21, 155, 156]. "nano" refers to nanostructuring of the sample via ball milling [2, 3]. Progress in *p*-type system see Figure 10.1 in Chapter 10.

and *n*-type TiNiSn based materials as well as the possibility for an industrial upscaling has been proven and thermoelectric modules have been fabricated. *Bartholomé et al.* built TE modules based on half-Heusler compounds from material synthesized in kg-batches [5]. The material performance is in line with the published values for comparable material compositions and exhibits peak ZT-values of 0.7 for the *n*-type and 0.5 for the *p*-type samples. The modules built from these materials have a maximum power output of 2.8 W with a total module area of 25×25 mm^2, resulting in the highest values for the power density of 3.2 W/cm^2 and a Z-value of 3.7×10^{-4} K^{-1} for half-Heusler modules published so far. The long-term stability and reproducibility of these modules could be verified by the authors.

These investigations eludicate another important issue regarding the requirements for an TE material, that is the long-term stability under operating conditions. For the *n*-type materials, very recently, the stability of the submicrostructuring and thermoelectric properties under thermal cycling conditions was proven [157]. Finally, it could be shown, that the *p*-type materials are stable regarding their structural and thermoelectric properties during an extensive long-term stability test under working conditions (see Chapter 9) as well.

4 Experimental details

4.1 Sample preparation

Half-Heusler compounds can be prepared easily by a conventional sintering method. Polycrystalline ingots are obtained by arc melting of stoichiometric amounts of the elements on a water cooled crucible under a Ti getter purified argon gas atmosphere. This is followed by a heat treatment in an evacuated quartz tube in order to promote the crystalline order. The rapid cooling during the solidification process is key to achieve a microstructuring via intrinsic phase separation in the n-type TiNiSn system [114–116]. For the preparation of TiCoSb based compounds, a modification of the fabrication method is required due to the high-vapor pressure of Sb. Two different fabrication methods were investigated and a standard fabrication method was established. Details of this study can be found in Chapter 5.

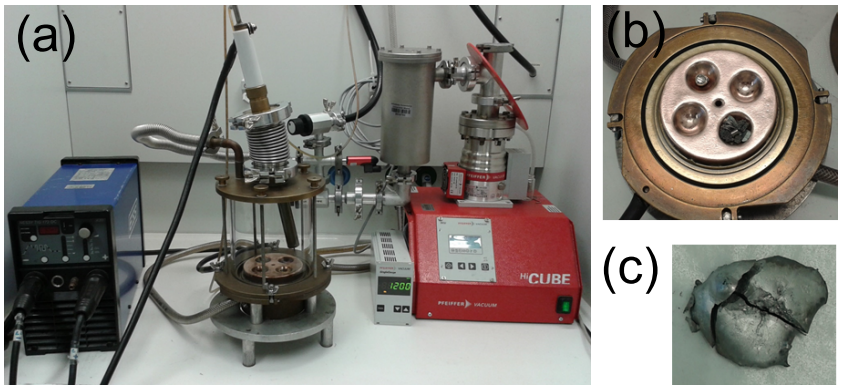

Figure 4.1: (a) Arc melter with High Voltage generator in blue on the left side and high vaccum pump on the right. (b) Water-cooled copper heart with Ti sponge and sample. (c) Crushed ingot after the second melting steps.

For the standard arc melting procedure, stoichiometric amounts of the elements were weighted in and melted three times under an argon gas atmosphere (10^{-4} mbar) with a current just large enough to provide rapid melting of the elements (approximately 50 – 75 A). The ingots were flipped and remelted three times on each side. Next, they were crushed, and the weight loss due to the evaporation of Sb during the arc melting process was compensated by adding Sb. The melting steps were then performed two more times with intermediate crushing and addition of Sb.
This routine was followed for the preparation of all samples except for the reproducibility study (see Chapter 5). Ingots of approximately 10 –15 g were obtained and subsequently annealed in quartz ampules under vacuum at 900°C for 7 days to promote the crystal ordering and then quenched in ice water.

For the reproducibility study, samples using the same procedure but without Sb addition and with addition of an averaged amount of Sb were prepared to analyze the sensitivity of the thermoelectric properties to the correct stoichiometry.

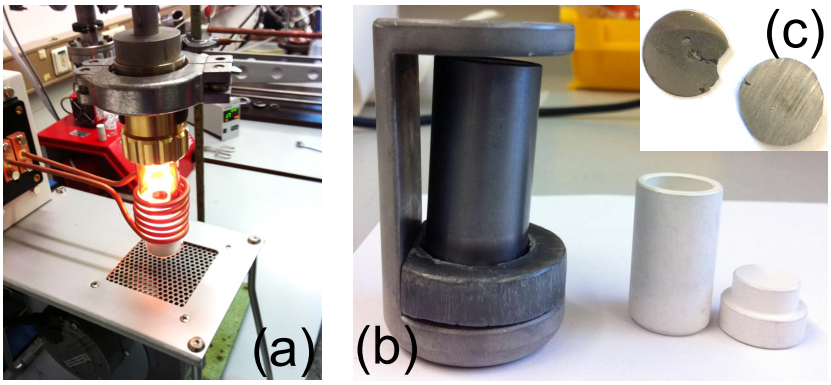

Figure 4.2: Induction furnace during the melting process (a). Sample holder with Boron nitride crucible (b). Sample after inductive melting, cut in the middle (c).

For comparison, ingots were prepared by inductive melting in an argon atmosphere at a low pressure of approximately 1.0 mbar. Special care was taken to prevent the evaporation of Sb. Therefore, a specially designed lidded BN crucible coated with Y_2O_3 was used, and the temperature was observed carefully with a pyrometer. The temperature can be regulated by controlling the power output of the high-frequency generator. The best results were obtained using a quick melting process (within 3 min) and a power of 1.0 to 4.3 kW and then holding the temperature close to the melting point at 1400 – 1500°C for 30 min.

The ingots were cut in discs and bars by a diamond saw for the characterization of the thermoelectric properties and microstructural investigations.

4.2 Structural investigations

The crystal structure of all the samples was analyzed by powder X-ray diffraction (PXRD) at room temperature. Depending on the research facilities different instruments were used. At the JGU Mainz, PXRD with Mo K_α ($\lambda = 0.7093$ Å) radiation was performed on a Bruker AXS D8 Advance in reflection mode. A Seifert XRD 3000TT in Bragg-Brentano geometry with an automatic divergence slit was used to obtain PXRD patterns with Cu K_α radiation ($\lambda = 1.5418$ Å). At the MPI CPfS Dresden, the samples were investigated with Cu $K_{\alpha 1}$ ($\lambda = 1.540598$ Å) radiation using an image-plate Huber G670 Guinier camera equipped with a Ge(111) monochromator operating in the range $10° \leq 2\theta \leq 100°$.

To investigate the phase separation in detail the samples were analyzed using high-resolution X-ray powder diffraction with synchrotron radiation with $\lambda = 1.65307$ Å. The experiments were performed at the XPD beamline at the bending magnet D10 at the Brazilian Synchrotron Light Laboratory (LNLS). Detailed beamline characteristics are given by *Ferreira et al.* [158].

Metallographically prepared cross sections of the samples of approximately 4×1 mm^2 were investigated by scanning electron microscopy (SEM) and energy dispersive X-ray spectroscopy (EDX). The phase distribution was documented by optical microscopy (Zeiss, Axioplan), as well.
The semi-quantitative determination of the chemical composition and the recording of the qualitative element distribution were realized by using the element specific X-ray intensities measured with an energy dispersive detector (Bruker, XFlash SDD 30 mm) that was attached to the SEM (Philips XL30 with LaB_6 cathode). An acceleration voltage of 25 kV and spot mode were used for the determination of the chemical compositions of the phases. The PB-Phi(Rho-z) matrix correction model was applied for calculation of the composition (Bruker, Quantax 400 software package Ver. 1.9.4).
Element-specific EDX mappings in Chapter 8 were obtained by recording hypermaps with enhanced count rates over an interval of 60 min, and the element-distribution images were extracted from the deconvoluted intensities of the X-ray lines. In case of Hf, the M_α line instead of the L_α line was selected to represent the Hf distribution due to the better spatial resolution obtained in the former case. For all other elements, the same X-ray lines were used for the quantification and the element distribution images.
In order to monitor the long-term stability of the microstructure (see Chapter 9), back-scattered electron (BSE) images were recorded by an JEOL JSM-7800F field emission scanning electron microscope with an accelaration voltage of 18.0 kV. An overview of the microstructure of the samples was obtained by recording 12 single images and combining them.
SEM and EDX analysis in Chapters 5, 6, and 7 were performed at the JGU Mainz with a FEI Nova NanoSEM 630 equipped with a EDX detector. To determine the composition of the phases a standardless ZAF correction was applied for quantitative evaluation by means of the EDAX software.
In addition to EDX spectroscopy, the stoichiometry of the samples was analyzed by inductively coupled plasma optical emission spectrometry (ICP-OES).
Due to importance of the mechanical stability of the materials for the fabrication of TE modules, the mechanical properties were tested by Vickers hardness measurements with a Struers Dura-Scan-20, applying a force between 0.1 kg fs and 0.3 kgfs on the polished and coplanar samples.

4.3 Thermoelectric properties

The transport properties at low temperatures (2 – 350 K) were determined by a Physical Properties measuerment system (PPMS, Quantum Design, San Dieago, CA). The Ther-

mal Transport Option (TTO) was used to measure the Seebeck coefficients S, electrical conductivity σ and thermal conductivity κ by a four point probes method (see Figure 4.3 (a)). Therefor the sample bars were contacted with gold stripes and a silver paste.

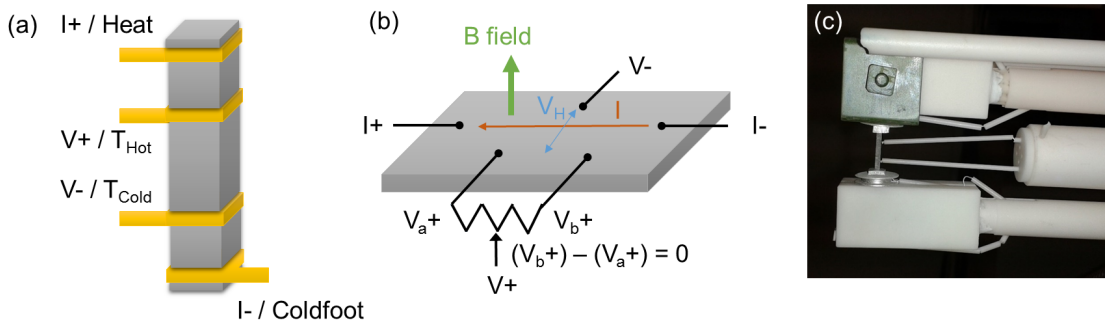

Figure 4.3: (a) Schematic drawing of the sample preparation for the PPMS TTO Option. Au-coated Cu-leads are wrapped around the sample and bonded with epoxy resin. (b) Contacting for 5-wire Hall measurement with the ACT Option. (c) Sample bar in an LSR-3 (Linseis) with the force-fitted contacts by two platinum electrodes on top and bottom and a thermocouple in the middle. The set-up is placed in a heatable oven under He atmosphere.

Five-Wire Hall measurements were performed with the AC Transport Option (AC-T) to determine the Hall coefficients R_H and resistivity ρ (see Figure 4.3 (b)). From these values the carrier concentration

$$n_H = -\frac{1}{R_H e} \tag{4.1}$$

and mobility

$$\mu_H = \frac{\sigma}{n_H e} \tag{4.2}$$

with e elementary charge, were determined.

The samples' carrier concentration n at room temperature and above was determined by Hall measurements using the IPM-HT-Hall-900K system developed and constructed by Fraunhofer IPM in Freiburg, Germany.

In the mid- and high-temperature range (100 – 700°C), the electrical conductivity σ and Seebeck coefficient S were measured simultaneously by an LSR 3 (Linseis) in He atmosphere by a force-fitting four-point probe method as shown in Figure 4.3 (c).

The thermal conductivity κ was calculated using the relation:

$$\kappa = \alpha \, \rho \, C_p \tag{4.3}$$

The values α were measured by means of the laser flash method using the Netzsch LFA 457 instrument (see Figure 4.4(a)). The density ρ was calculated from the mass and volume of the cut bars. The specific heat capacities C_p were estimated by means of the Dulong–Petit law (Equation 3.20). The accuracy of the calculated values was confirmed by measurements of the as-cast and annealed samples by a differential scanning calorimeter (DSC8500 Netzsch, see Figure 4.4(b)).

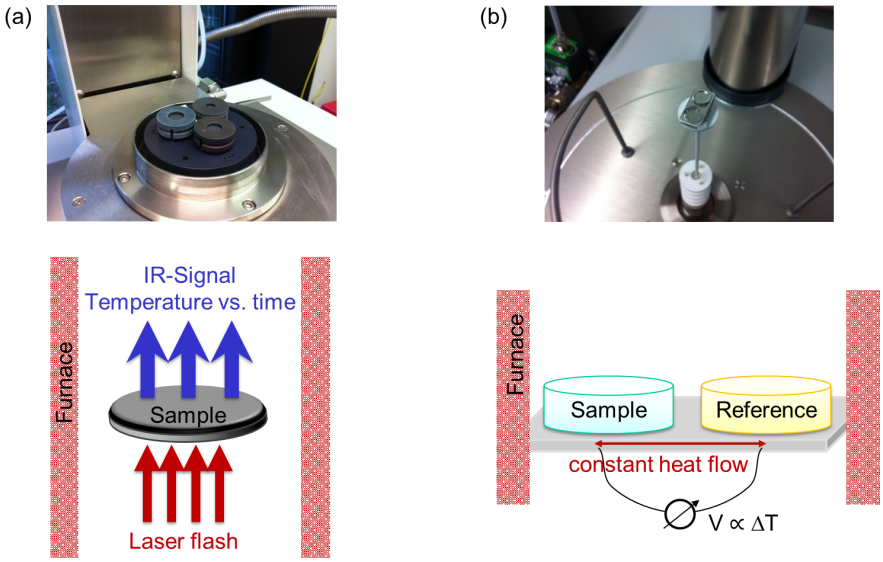

Figure 4.4: Instruments and schematic drawings of the measurment principles for the determination of the thermal conductivity. (a) LFA (Netzsch) - The threefold rotatable sample holder is placed in an oven, flushed with protective gas or under vacuum. The diffusivity α is proportional to the time derivative of temperature. (b) DSC (Netzsch) - Sample and reference (empty) pans are placed on an integrated sensor and heated simultaneously under protective gas. With a thermocouple the temperature difference between sample and reference is detected.

Finally, the figure of merit ZT was calculated according to Equation 3.4. The uncertainties were 3% for the electrical conductivity and thermal diffusivity, 5% for the Seebeck coefficient, and 3% for the geometrical density measurements, thereby leading to a 5% uncertainity in thermal conductivity, 10% in power factors $S^2\sigma$, and 11% in the ZT values by propagation of errors. The transport properties were measured during heating to 700°C and cooling for verification that there was no degradation in the various sample properties.

5 Reproducibility study

Intrinsic phase separation is an important key point to achieve low thermal conductivities in half-Heusler compounds. This concept is already well established for the n-type systems (Ti/Zr/Hf)NiSn [17–19]. Due to the high vapor pressure of Sb the transfer of the conventional sintering method to the p-type (Ti/Zr/Hf)$CoSb_{0.8}Sn_{0.2}$ system is not straight forward. The influence of different preparation procedures on the quality and reproducibility of the samples was analyzed leading to the development of a reliable fabrication method. As an example the compound $Ti_{0.3}Zr_{0.35}Hf_{0.35}CoSb_{0.8}Sn_{0.2}$ was investigated and the repeatability was ensured by having an additional person[1] performing the experiment independently.

5.1 Experimental details

The reproducibility of the sample preparation for p-type (Ti/Zr/Hf)$CoSb_{0.8}Sn_{0.2}$ was investigated by employing two synthesis methods, arc melting and inductive melting. Three different approaches were applied to handle the weight loss due to the high vapor pressure of Sb during the arc melting process: In the first, the missing amount was added (samples AM-A1, AM-A2, and AM-B2); in the second, the weight loss was not compensated (AM-A3), and in the third, an average value of Sb obtained from the previous experiments was added (AM-B2). For comparison, samples were fabricated by inductive melting, one with the correct nominal composition (IM-B1) and a second with 5 at.% less Sb, $Ti_{0.3}Zr_{0.35}Hf_{0.35}CoSb_{0.75}Sn_{0.2}$ (IM-B2). Two different persons (A and B) performed the experiments to eliminate the impact of the experimenter on the results.

5.2 Results and discussion

The crystal structure of all the samples was analyzed by PXRD, the obtained diffraction patterns show very little difference between samples fabricated by the two methods. Figure 5.1(a) compares arc melted samples with and without the addition of Sb to samples fabricated by inductive melting. The reflections of samples with an Sb deficiency are shifted to slightly higher scattering angles 2θ compared to those of samples with the correct stoichiometry. In samples prepared by inductive melting, β-Sn impurities were detectable. Nevertheless, the thermoelectric properties should be very sensitive to the correct stoichiometry. Evaporation of Sb produces unoccupied lattice sites, which should increase the resistivity. At the same time, the Seebeck coefficient is increased. This agrees well with the measurements of the transport properties at room temperature as shown in Table 5.1). The choice of production method has a very obvious effect on

[1] The synthesis was performed by a student (Person B), that I (Person A) supervised during a research module in the group of Prof. C. Felser (Forschungsmodul in Anorganischer Chemie im Rahmen des Diplomstudiengangs Chemie).

Table 5.1: Reproducibility of $Ti_{0.3}Zr_{0.35}Hf_{0.35}CoSb_{0.8}Sn_{0.2}$ using different fabrication methods. Listed are sample codeconsisting of fabrication procedure, arc melting (AM) or inductive melting (IM) and the experimenter A and B, and the thermoelectric properties κ [$WK^{-1}m^{-1}$], S [μVK^{-1}], σ [$10^{-4}Sm^{-1}$], $S^2\sigma$ [$10^{-3}Wm^{-1}K^{-2}$], and ZT at 300 K determined with a PPMS.

Sample code	Compensation for weight loss	κ	S	σ	$S^2\sigma$	ZT
AM-A1	Sb added	2.96	124.1	8.00	1.23	0.12
AM-A2	Sb added	2.17	130.0	6.41	1.08	0.15
AM-A3	no Sb added	2.32	166.9	0.82	0.23	0.03
AM-B1	Sb added	2.80	122.1	8.18	1.22	0.13
AM-B2	average mass of Sb added	2.68	139.4	6.36	1.23	0.14
IM-B1	correct stoichiometry	2.89	174.2	2.67	0.81	0.09
IM-B2	5 at.% less Sb	2.56	120.6	1.67	0.24	0.03

the figure of merit ZT as displayed in Figure 5.1(b)]. Samples produced by arc melting with the addition of the missing amount of Sb all exhibit the same values. Further, the sample with the addition of an average amount of Sb shows the same characteristics. An off-stoichiometric amount of Sb – either produced on purpose by inductive melting or by not adding Sb during the arc melting process – yielded the lowest ZT values. The sample with the correct stoichiometry produced by inductive melting exhibits ZT values between those two extremes. This could be the result of Sn impurities, which are metallic. Further, the bars for the measurements were cut from the middle of the sample, and owing to the long melting time in the induction furnace, the Sb could recrystallize on the surface of the sample, causing an Sb deficiency in the middle.

Optical microscopy with polarized light (Figure 5.2) shows some voids and cracks in the samples fabricated by inductive melting, which made cutting very difficult. Due to the slow cooling rate, Sb is evaporating during the consolidation process which leads to microcracks and voids. Apart from that the samples are homogenous since no phase contrast is visible. SEM images show that those samples undergoe an intrinsic phase separation, but in contrast to samples produced by arc melting, islands of the secondary half-Heusler phase are formed around the voids instead of forming an interconneting network. A detailed discussion of the intrinsic phase separation and the composition of the phases is given in Chapter 6.

From these results, it is obvious that to obtain homogeneous and dense ingots, the quick arc melting process in combination with crushing of the samples between the individual melting steps and the replacement of evaporated Sb must be used. By following this procedure, reproducible thermoelectric properties can be obtained.

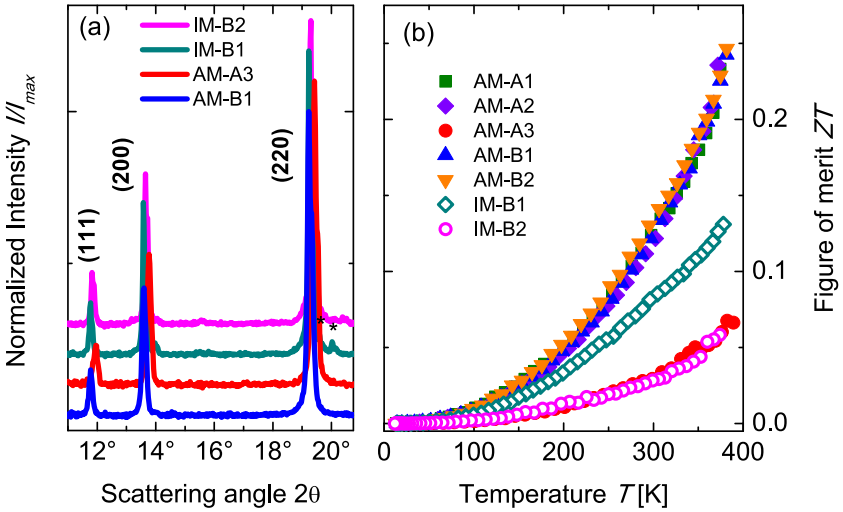

Figure 5.1: Reproducibility study of the fabrication process. (a) Comparison of PXRD patterns obtained with Mo K_α radiation of samples prepared by inductive melting and by arc melting. (b) Figure of merit ZT of all samples prepared by various fabrication procedures (see Table 5.1 for details).

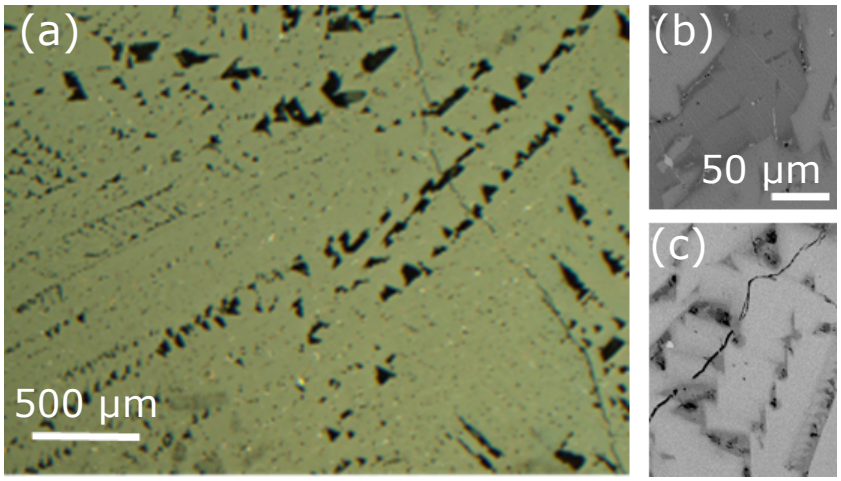

Figure 5.2: Impact of the fabrication process on the microstructure of the samples. (a) Optical microscopy of inductive melted sample $Ti_{0.3}Zr_{0.35}Hf_{0.35}CoSb_{0.8}Sn_{0.2}$ (IM-B2). BSE images of arc melted AM-B1 (b), and inductive melted IM-B2 (c) samples.

5.3 Conclusion

To summarize, the influence of different fabrication procedures on the thermoelectric performance of *p*-type half-Heusler compounds was investigated. The detailed study was performed on $Ti_{0.3}Zr_{0.35}Hf_{0.35}CoSb_{0.8}Sn_{0.2}$ proving that the modified standard arc melting fabrication delivers reproducible results. It was demonstrated that the microstructuring by an intrinsic phase separation in the (Ti/Zr/Hf)$CoSb_{1-x}Sn_x$ system can be reproduced reliably. The average of the standard deviation of the ZT values measured at temperatures of 100 to 380 K is only 6.5%, which lies in the range of the measurement errors; therefore, the results can be considered accurate.
This standard fabrication process was applied to synthesize all other samples in this work. Starting from this, the thermoelectric performance of this system was enhanced by analyzing the impact of substitution on two different lattice sides. First, the influence of the isoelectronic substitution of Ti by its heavier homologues Zr and Hf in order to achieve an intrinsic phase separation as a novel approach to optimize the thermoelectric properties of *p*-type Half-Heusler compounds (Ti/Zr/Hf)$CoSb_{0.8}Sn_{0.2}$ was investigated. Second, the carrier concentration was optimized via substitution of Sb by Sn in the system $Ti_{0.3}Zr_{0.35}Hf_{0.35}CoSb_{1-x}Sn_x$.

6 Intrinsic phase separation

The relatively high thermal conductivity is an obstacle to implementing Heusler TE's. The total thermal conductivity consists of an electronic and a lattice contribution. In general, the phonon contribution can be reduced effectively by point and mass defect scattering by forming a solid solution or by additional boundary scattering through a reduction of the grain size or phase separation. For example, the lattice thermal conductivity of *p*-type MCoSb compounds can be reduced by embedding nanoparticles such as HfO_2 inclusions [22]. The most successful improvement of the TE properties of state-of-the-art *p*-type materials involves the artificial reduction of the grain size via ball milling [3, 21]. The authors claim that the ZT improvement of 60% from 0.5 to 0.8 in $Zr_{0.5}Hf_{0.5}CoSb_{0.8}Sn_{0.2}$ comes from a simultaneous increase in the Seebeck coefficient and a significant decrease in thermal conductivity due to the nanostructuring. The benchmark of $ZT = 1.0$ in $Hf_{0.8}Ti_{0.2}CoSb_{0.8}Sn_{0.2}$ was reached by replacing Zr with its heavier homologue Hf by a similar fabrication process [3]. Another concept to achieve high thermoelectric performance in bulk materials is phase separation on a micro- or nano-meter scale. Investigations have mainly focused on the PbTe, PbSe, and PbS systems [159]. For example, the precipitation of a second phase in PbTe + 12% PbS led to a reduction of approximately 50% of the lattice thermal conductivity to 0.45 W $m^{-1}K$ [80]. Recently, ZT values up to 2 were reported for *p*-type $Ge_{0.87}Pb_{0.13}Te$ as a result of sub-micron phase separation [160].

As a novel approach for improvement of the thermoelectric performance of *p*-type half-Heusler compounds, the impact of an intrinsic phase separation was investigated. A successful recipe for achieving intrinsic phase separation in the *n*-type material based on the TiNiSn system is isoelectronic partial substitution of Ti with its heavier homologues Zr and Hf [16, 161–163]. Recently, the outstanding thermoelectric properties of a *n*-type material with ZT up to 1.4 based on doped $Ti_{0.5}Zr_{0.25}Hf_{0.25}NiSn$ [149, 150] were explained by *Schwall* and *Balke* [14]. The samples exhibited a microstructure composed of three coexisting $C1_b$ phases that were rich in either Ti or Hf. As demonstrated in Chapter 5 this concept can be transfered to the *p*-type $Ti_{0.3}Zr_{0.35}Hf_{0.35}CoSb_{0.8}Sn_{0.2}$ compound. This chapter investigates systematically how an intrinsic phase separation can be generated in the *p*-type system $M CoSb_{0.8}Sn_{0.2}$. By isoelectronic substitution on the M-position (M = Ti, Zr, Hf, $Ti_{0.5}Zr_{0.5}$, $Zr_{0.5}Hf_{0.5}$, and $Ti_{0.5}Hf_{0.5}$) the draft of a pseudo-ternary phase diagram was established and related to the structural and thermoelectric investigations.

6.1 Structural investigations

The $C1_b$ structure of all samples was confirmed by PXRD analysis of the powder samples. All samples were phase-pure despite a marginal amount of β-Sn (1.2%), which is close to the detection limit. Representative PXRD measurements of $HfCoSb_{0.8}Sn_{0.2}$ and

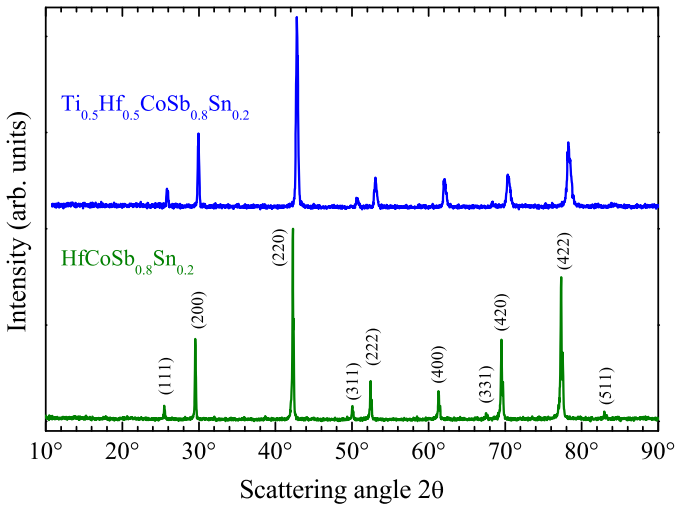

Figure 6.1: Representative PXRD patterns with CuK_α radiation of samples with M = $Ti_{0.5}Hf_{0.5}$ and M = Hf.

$Ti_{0.5}Hf_{0.5}CoSb_{0.8}Sn_{0.2}$ are shown in Figure 6.1. The position of the main (220) reflection of $Ti_{0.5}Hf_{0.5}CoSb_{0.8}Sn_{0.2}$ is shifted to a higher scattering angle due to the decrease of the lattice parameter upon substitution of Hf by Ti, as one would expect on the basis of the atomic radii of the elements. The reflections at higher scattering angles ((400), (420), and (422)) are sharper for $HfCoSb_{0.8}Sn_{0.2}$, whereas in the case of $Ti_{0.5}Hf_{0.5}CoSb_{0.8}Sn_{0.2}$ the peaks are broader and asymmetric.

This is a strong indication of the existence of a second phase with a slightly different lattice parameter (see Figure 6.2 for the EDX results). Investigation of the analogous *n*-type Heusler compound $Ti_{0.5}Zr_{0.25}5Hf_{0.25}NiSn$ by synchrotron radiation revealed a splitting of the main reflex (220) into a triple peak corresponding to three Heusler phases [14]. Therefore, it is reasonable that the same effect could occur in the *p*-type system.

As shown in Table 6.1, the overall composition of all samples as analyzed by EDX spectroscopy agrees well with their nominal composition, which indicates that no significant loss of Sb took place. Samples without substitution at the M position (M = Ti, Zr or Hf) show a homogeneous distribution of all elements apart from some minor variations of the Sn and Sb content. Further, the alloying of Zr and Hf did not result in phase separation because the chemical behavior of both atoms is very similar and they have nearly the same atomic radii caused by the Lanthanide contraction. This confirms the results previously reported by *Culp et al.* [21]. The secondary electron (SE) image of $Zr_{0.5}Hf_{0.5}CoSb_{0.8}Sn_{0.2}$ (see Figure 6.2a) shows the typical microstructure of the samples with M = Ti, Zr, Hf or $Zr_{0.5}Hf_{0.5}$. The matrix with composition $Zr_{0.45}Hf_{0.55}Co_{0.95}Sb_{0.9}Sn_{0.1}$ is interspersed with some darker regions of $Zr_{0.5}Hf_{0.5}CoSb_{0.7}Sn_{0.3}$. Additionally, some very bright spots, which can be identified

Table 6.1: Composition and phases of the samples $M\mathrm{CoSb_{0.8}Sn_{0.2}}$ as determined by EDX spectroscopy, and experimental density ρ [g/cm^3] and Vickers hardness HV0.3.

M	Composition	Phases	ρ	HV0.3
Ti	$\mathrm{Ti_{0.97}Co_{0.99}Sb_{0.79}Sn_{0.25}}$	$\mathrm{Ti_{1.01}Co_{0.97}Sb_{0.91}Sn_{0.1}}$	7.21	783
		$\mathrm{Ti_{0.91}Co_{1.19}Sb_{0.23}Sn_{0.67}}$		
Zr	$\mathrm{Zr_{1.01}Co_{0.96}Sb_{0.77}Sn_{0.25}}$	$\mathrm{Zr_{1.02}Co_{0.96}Sb_{0.87}Sn_{0.16}}$	7.69	810
		$\mathrm{Zr_{1.01}Co_{0.96}Sb_{0.15}Sn_{0.88}}$		
Hf	$\mathrm{Hf_{1.07}Co_{0.93}Sb_{0.80}Sn_{0.20}}$	$\mathrm{Hf_{1.11}Co_{0.92}Sb_{0.83}Sn_{0.14}}$	10.17	882
		$\mathrm{Hf_{0.89}Co_{1.28}Sb_{0.07}Sn_{0.76}}$		
$\mathrm{Ti_{0.5}Zr_{0.5}}$	$\mathrm{Ti_{0.49}Zr_{0.50}Co_{0.94}Sb_{0.89}Sn_{0.18}}$	$\mathrm{Ti_{0.45}Zr_{0.56}Co_{0.96}Sb_{0.94}Sn_{0.09}}$	7.43	716
		$\mathrm{Ti_{0.64}Zr_{0.38}Co_{0.98}Sb_{0.89}Sn_{0.13}}$		
$\mathrm{Zr_{0.5}Hf_{0.5}}$	$\mathrm{Zr_{0.47}Hf_{0.56}Co_{0.94}Sb_{0.84}Sn_{0.19}}$	$\mathrm{Zr_{0.47}Hf_{0.56}Co_{0.93}Sb_{0.88}Sn_{0.15}}$	9.22	846
		$\mathrm{Zr_{0.52}Hf_{0.51}Co_{0.97}Sb_{0.72}Sn_{0.28}}$		
$\mathrm{Ti_{0.5}Hf_{0.5}}$	$\mathrm{Ti_{0.52}Hf_{0.56}Co_{0.98}Sb_{0.65}Sn_{0.29}}$	(I) $\mathrm{Ti_{0.65}Hf_{0.31}Co_{1.21}Sb_{0.23}Sn_{0.61}}$	9.38	868
		(II) $\mathrm{Ti_{0.38}Hf_{0.70}Co_{0.98}Sb_{0.84}Sn_{0.1}}$		

as Sn inclusions, are visible.
Contrarily, the mixing of Ti with Zr results in areas with slightly more Ti ($\mathrm{Ti_{0.6}Zr_{0.4}}$) or slightly more Zr ($\mathrm{Ti_{0.4}Zr_{0.6}}$). Still the composition changes continuously and no clear phase boundaries are observed. This effect is enhanced when Ti is alloyed with Hf. The secondary electron image of $\mathrm{Ti_{0.5}Hf_{0.5}CoSb_{0.8}Sn_{0.2}}$ in Figure 6.2b shows separation into a two-phase microstructure: a dendritic structure consisting of a Hf- and Sb-rich Heusler phase (phase II), with an approximate composition of $\mathrm{Ti_{0.4}Hf_{0.7}CoSb_{0.85}Sn_{0.1}}$, in a Ti- and Sn-rich matrix $\mathrm{Ti_{0.65}Hf_{0.3}Co_{1.2}Sb_{0.2}Sn_{0.6}}$ (phase I). The bright spots are again identified as Sn inclusions, whereas the black spots are Hf.

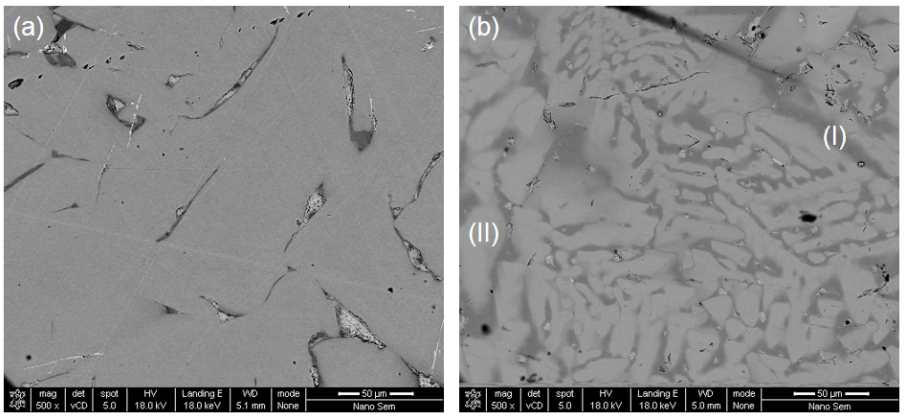

Figure 6.2: Secondary electron image of $\mathrm{Zr_{0.5}Hf_{0.5}CoSb_{0.8}Sn_{0.2}}$ (a) in comparison to $\mathrm{Ti_{0.5}Hf_{0.5}CoSb_{0.8}Sn_{0.2}}$ (b).

Since the mechanical stability of a TE material is very important for application and processing, the Vickers hardnesses of the compounds were investigated at room

temperature. The values are presented in Table 6.1. All compounds show relatively high intrinsic hardness, which corresponds to the previously reported values for the *n*-type material based on *M*NiSn [164]. This is favorable for the co-processing of the *n*- and *p*-type materials in a TE device.

6.2 Thermoelectric properties

The temperature dependence of the thermal conductivity κ, electrical conductivity σ, and Seebeck coefficients S of $M\mathrm{CoSb_{0.8}Sn_{0.2}}$ (M = Ti, Zr, Hf, $\mathrm{Ti_{0.5}Zr_{0.5}}$, $\mathrm{Zr_{0.5}Hf_{0.5}}$, and $\mathrm{Ti_{0.5}Hf_{0.5}}$) are plotted in Figure 6.3. The thermal conductivity of nonsubstituted compounds (M= Ti, Zr, or Hf) decreased with increasing temperature and exhibited the highest values. The values of κ decreased for solid-solution alloying of $M = \mathrm{Ti_{0.5}Zr_{0.5}}$ and $\mathrm{Zr_{0.5}Hf_{0.5}}$ due to the mass differences of Ti, Zr, and Hf atoms. This reduced the lattice thermal conductivity through chemical disorder scattering. The nearly constant value of κ for the composition $\mathrm{Ti_{0.5}Hf_{0.5}}$ over the whole temperature range is remarkable indicating a glass-like behaviour. With a value of 3.2 W/(m*K) a reduction of 39% compared to $\mathrm{TiCoSb_{0.8}Sn_{0.2}}$ at 700 °C was achieved. In this case, the presence of the intrinsic microstructure leads to additional boundary scattering at the interfaces and hence to a reduction of the lattice thermal conductivity. Comparable small values reported in the literature were only achieved by micro- or nano-structuring using a ball-milling process [2–4] or by the embedding of nanoinclusions [155, 165]. For comparison, the transport properties of nanostructured compounds made by Yan et al. [3] with the composition $\mathrm{Ti_{0.5}Hf_{0.5}CoSb_{0.8}Sn_{0.2}}$ are plotted.

All samples show metallic behavior as the electrical conductivity σ decreases with increasing temperature (Figure 6.3b). The composition $\mathrm{TiCoSb_{0.8}Sn_{0.2}}$ exhibited the lowest value of σ. The values increased upon substitution of Ti with the heavier homologous Zr and Hf, indicating an increase in the charge carrier concentration.

All measured Seebeck coefficients are positive, indicating *p*-type transport behavior. The temperature dependency shows an almost linear increase. The maximum was not reached in the experimental temperature range, which is very attractive for high-temperature applications. Contrary to the electrical conductivity, the highest Seebeck coefficient of 289.9 $\mu\mathrm{VK^{-1}}$ (at 600 °C) was obtained for $\mathrm{TiCoSb_{0.8}Sn_{0.2}}$. Alloying of Zr and Hf does not effect the Seebeck coefficient significantly. The corresponding values of S for M = Zr, Hf, and $\mathrm{Zr_{0.5}Hf_{0.5}}$ are similar. In contrast, the alloying of Zr and Hf by Ti enhances the Seebeck coefficient and reaches a value of 244.7 $\mu\mathrm{VK^{-1}}$ at 600 °C for $M = \mathrm{Ti_{0.5}Hf_{0.5}}$, whereas the unsubstituted $\mathrm{ZrCoSb_{0.8}Sn_{0.2}}$ and $\mathrm{HfCoSb_{0.8}Sn_{0.2}}$ only achieve a value of 208.1 $\mu\mathrm{VK^{-1}}$ and 209.8 $\mu\mathrm{VK^{-1}}$ respectively.

The calculation of the power factor $S^2\sigma$ reveals that both effects nearly compensate for each other. As shown in Figure 6.4a, the absolute values are between 1.94×10^{-3} $\mathrm{WK^{-2}m^{-1}}$) for $\mathrm{Ti_{0.5}Zr_{0.5}}$ and 3.38×10^{-3} $\mathrm{WK^{-2}m^{-1}}$) at 700 °C for Hf.

By combining the electronic properties with the previously discussed thermal conductivity, we obtained a maximal ZT of approximately 0.9 at 700°C for $\mathrm{Ti_{0.5}Hf_{0.5}}$ and $\mathrm{Zr_{0.5}Hf_{0.5}}$. Comparable high ZT values for *p*-type Heusler systems have only been re-

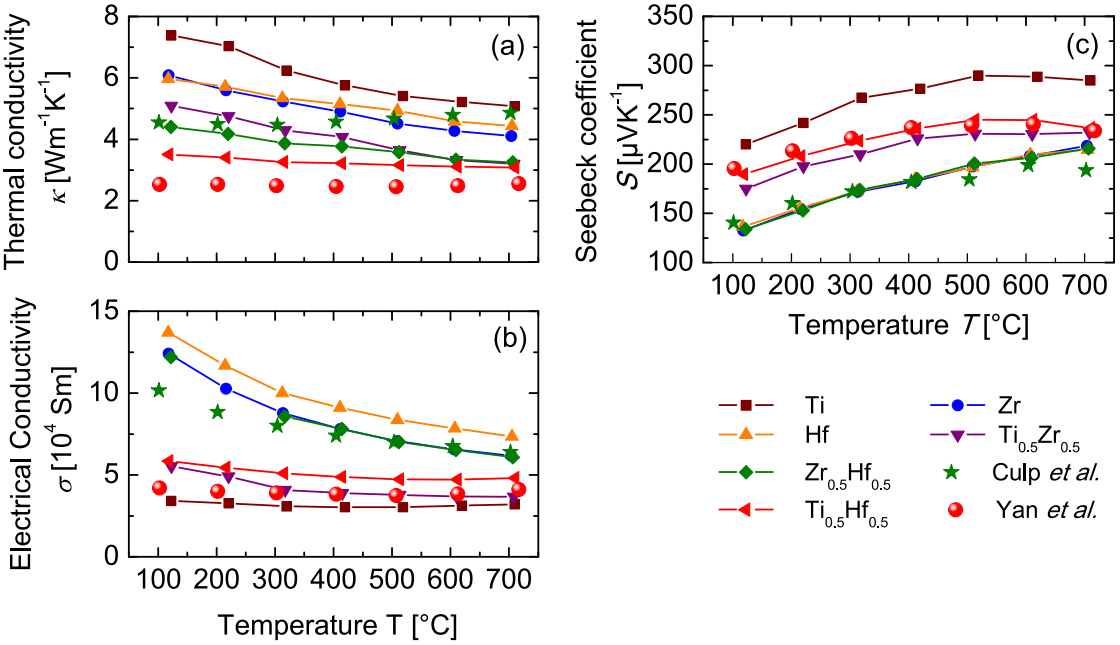

Figure 6.3: (a) Thermal conductivity κ, (b) electrical conductivity σ, and (c) Seebeck coefficient S as a function of temperature for MCoSb$_{0.8}$Sn$_{0.2}$ with the indicated composition of M. Comparison with values reported in the literature for M = Zr$_{0.5}$Hf$_{0.5}$ ($\star$ ingot sample [21]) and M = Ti$_{0.5}$Hf$_{0.5}$ ($\bullet$ nanostructured sample [3]).

ported for a nanostructure approach via ball milling [2, 3]. More promising is that the value of the Heusler compound obtained in the current study is comparable with the record p-type value based on SiGe alloying, as shown in Figure 6.4(b) [56]. Here it is important to keep in mind that the basic cost of the Heusler TE is approximately 60% lower than that of SiGe [64].

6.3 Conclusions

An intrinsic phase separation in the p-type Heusler system (Ti/Zr/Hf)CoSb$_{0.8}$Sn$_{0.2}$ was obtained by applying isoelectronic alloying analogous to the n-type system [14]. Mandatory was the partial substitution of Ti with Hf, which resulted in nanostructuring of the system consisting of at least two stable Heusler phases – one rich in Ti and Sn and the other rich in Hf and Sb. Similar to the TiNiSn system a dendritical phase separation was observed. Subsequently, the thermal conductivity was reduced to 3.2 Wm^{-1}K^{-1} in Ti$_{0.5}$Hf$_{0.5}$CoSb$_{0.8}$Sn$_{0.2}$, which is an improvement of approximately 40% as compared to TiCoSb$_{0.8}$Sn$_{0.2}$. This led to a maximum ZT of 0.9 at 700 °C, i.e. a 80% enhancement in peak ZT from 0.5 to 0.9 compared to the best published value of an ingot p-type Half-Heusler compound [2]. Thus far, comparable good thermoelectric p-type materials

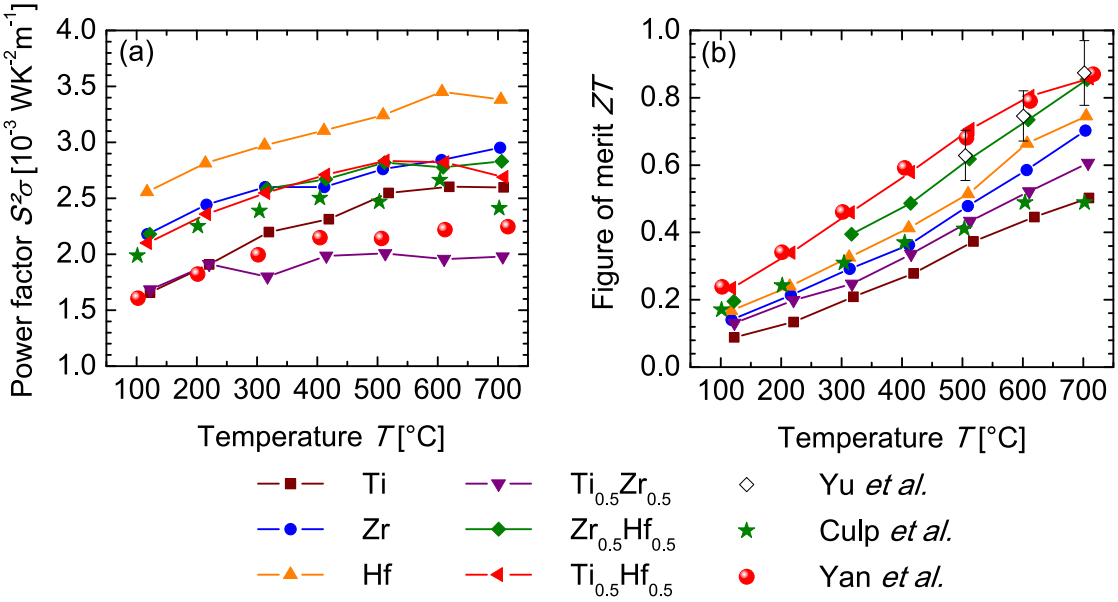

Figure 6.4: (a) Power factor PF and (b) Figure of merit ZT as a function of temperature for MCoSb$_{0.8}$Sn$_{0.2}$ with the indicated composition of M. Comparison with values reported in the literature for M = Zr$_{0.5}$Hf$_{0.5}$ ($\star$ ingot sample) [21], M = Ti$_{0.5}$Hf$_{0.5}$ ($\bullet$ nanostructured sample [3]), and the best SiGe-based p-type material (Si$_{95}$Ge$_5$)$_{0.65}$(Si$_{70}$Ge$_{30}$P$_3$)$_{0.35}$ ($\diamond$) [56].

of this structure type with a $ZT \geq 0.8$ have only been realized by a nanostructuring process via ball milling of premelted ingot samples followed by a rapid consolidation method, like hot pressing. The herein-presented simple arc-melting fabrication method reduces the fabrication time as compared to this multi-step nanostructuring process, as well as the high cost due to the spark plasma sintering or hot pressing step.
The high mechanical stability of the investigated half-Heusler compounds is favorable for the construction of thermoelectric modules. The Vickers hardness values are close to those of the n-type material, leading to good co-processability of both materials. This initial proof-of-concept can serve as a very useful starting point for the design of new materials for high-temperature thermoelectric applications.

7 Carrier concentration optimization

The well-established concept of intrinsic phase separation was transferred sucessfully to the *p*-type $M\mathrm{CoSb_{0.8}Sn_{0.2}}$ system (see Chapter 6) and the reproducibility of the used fabrication method by arc melting was proved (see Chapter 5). As a next step the the thermoelectric properties of the system are optimized by adjusting the carrier concentration within the series $\mathrm{Ti_{0.3}Zr_{0.35}Hf_{0.35}CoSb_{1-x}Sn_x}$ with x = 0.1, 0.15, 0.2, 0.3, 0.4, and 0.5 using partial substitution of Sb by Sn. This wide range of substitution was chosen to demonstrate the dependency of the thermoelectric properties on the carrier concentration.

Only a few systematic investigations of the optimum doping level in the $M\mathrm{CoSb_{1-x}Sn_x}$ system have been reported in the literature. In particular, samples with 15% Sn substitution are rare [4, 156, 166]. A common statement is, that the most effective *p*-doping for MCoSb is a substitution of 20% – 30% Sn for Sb [6].
In 2007, Sekimoto et al. investigated the series $\mathrm{ZrCoSb_{1-x}Sn_x}$ with x = 0, 0.05, 0.1, and 0.15 [156]. They obtained a maximum power factor of 3.0×10^{-3} $\mathrm{WK^{-2}m^{-1}}$ at 717 K for x = 0.15 and a maximum ZT of 0.45 at 948 K for x = 0.1. Their sample of $\mathrm{ZrCoSb_{0.85}Sn_{0.15}}$ exhibited almost the same ZT values, indicating that a Sn content of 10% – 15% is appropriate for improving the ZT of ZrCoSb. In contrast, in 2008 Ponnambalam et al. considered the electrical resistivity of 4.7 mΩcm for $\mathrm{Ti_{0.5}Zr_{0.5}CoSb_{0.85}Sn_{0.15}}$ a value too high for thermoelectric applications. Therefore, they did not pursue samples doped with 15% Sn further by varying the Ti and Zr content [166]. In 2013, Maji et al. reported on $\mathrm{Zr_{0.5}Hf_{0.5}Co_{0.4}Rh_{0.6}Sb_{1-x}Sn_x}$/CoSb composites with x = 0, 0,15, 0.2, 0.25, and 0.4 [4]. However, they found that the electronic and thermal transport properties are strongly influenced by the presence of CoSb inclusions rather than the substitution level x of Sn. Another review concluded that for MCoSb, substituting 20% – 30% Sn for Sb is the most effective *p*-doping [6].
All the recent progress in this material system seems to be based on a study by *Culp et al.* [21] in 2008, which reported an optimum ZT of 0.5 at 1000 K for x = 0.2 in the $\mathrm{Zr_{0.5}Hf_{0.5}CoSb_{1-x}Sn_x}$ (x = 0, 0.1, 0.2, 0.3, 0.5) system. The ingot samples were produced by arc melting with a 5% Sb excess. A breakthrough was reached by reducing the thermal conductivity via a nanostructuring approach by ball milling, which yielded a ZT of 0.8.[2] All subsequent enhancements rely on this recipe and then focus on the investigation of the composition M, leaving the Sn content untouched [3, 151]. For all the *p*-type thermoelectric materials within the TiCoSb system with a ZT close to or greater than 0.5, one finds only one study that plots the Seebeck coefficient S and electrical conductivity σ versus the carrier concentration n, namely, a study of $\mathrm{TiCo_{1-x}Fe_xSb}$ by *Wu et al.* in 2007 [155]. Recent publications instead moved on to other systems such as NbFeSb [167] and $\mathrm{V_{0.6}Nb_{0.4}FeSb}$ [168].

7.1 Structural investigations

Phase analysis by PXRD using a Mo K_α lab source confirmed the $C1_b$ structure. All samples show a broadening of the reflections due to the presence of two or sometimes even three half-Heusler phases. Samples with $x \geq 0.3$ contain a small amount of impurities (compare Table 7.1). As previously discussed [59], the resolution of an PXRD lab machine gives a hint of the presence of different half-Heusler phases, but it is not sufficient to clearly distinguish them. As an example, the sample with $x = 0.15$ was investigated using synchrotron radiation (see Figure 7.1). A very small amount of β-Sn was detected, and the characteristic splitting of the reflections by phase separation into half-Heusler phases with very similar lattice parameters was observed.

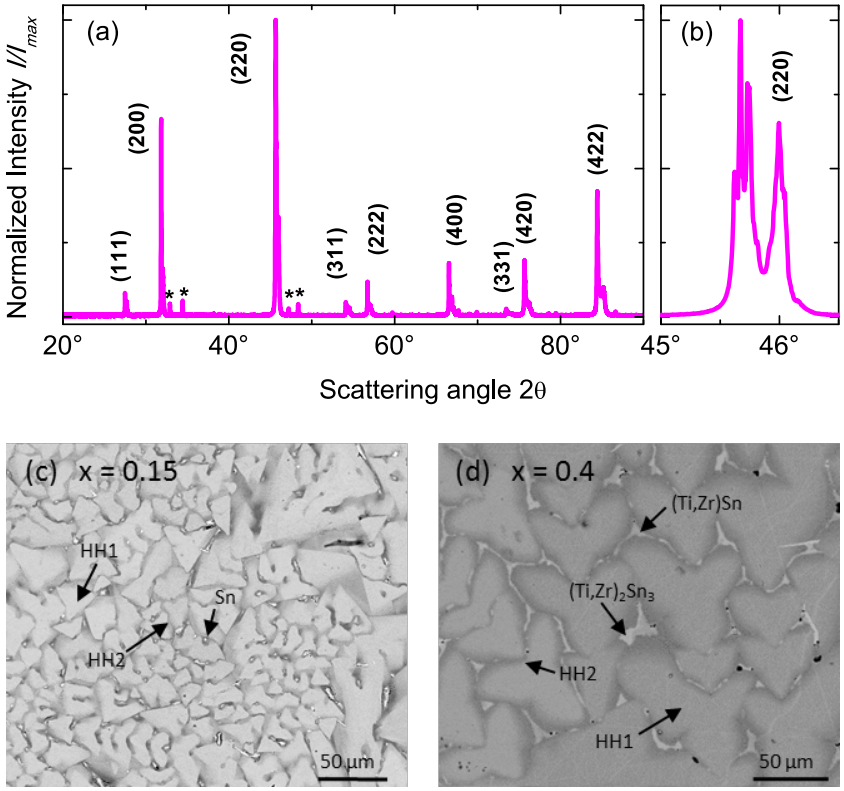

Figure 7.1: PXRD of $Ti_{0.3}Zr_{0.35}Hf_{0.35}CoSb_{0.85}Sn_{0.15}$ using synchrotron radiation (a) with enlargement of the main reflection (220) (b). Secondary electron imaging of the sample with x = 0.15 (c) and x = 0.4 (d).

EDX analysis confirmed the correct overall stoichiometry of all the compounds (see Table 7.1). Secondary electron images of samples with $x = 0.1$, 0.15, and 0.2 show a microstructure consisting of an Sb- and Zr/Hf-rich matrix (HH1) and an additional half-Heusler phase rich in Ti and Sn (HH2) compared to the nominal composition. The HH2 phase typically exhbits a slight excess of Co, which presumably occupies the vacant lattice positions like in the related $L2_1$ structure Co_2TiSn [59, 169, 170]. In

the sample with $x = 0.2$, three different half-Heusler phases can be identified. The typical microstructure is displayed in Figure 7.1(c). Very small inclusions of Sn and Hf were detected as impurity phases. Samples with $x \geq 0.3$ exhibit additional binary $(Ti/Zr/Hf)_xSn_y$ phases. This explains the additional reflection at $2\theta = 15.75°$ in the corresponding PXRD patterns. The network of the second half-Heusler phase is formed around these islands (compare Figure 7.1(d)). In summary, our structural investigations proved that all the samples underwent an intrinsic phase separation, but to achieve a phase separation into solely half-Heusler phases, the substitution level of Sn cannot exceed 20%. More Sn leads to the inclusion of additional binary phases on a micrometer scale.

Table 7.1: EDX analysis of the $Ti_{0.3}Zr_{0.35}Hf_{0.35}CoSb_{1-x}Sn_x$ samples. Indicated are overall composition, composition of the matrix (HH1), additional half-Heusler (HH2, HH3) phases, and observed inclusions of impurity phases.

		Ti	Zr	Hf	Co	Sb	Sn
$x = 0.1$	Overall	0.27	0.33	0.43	0.97	0.92	0.09
	HH1	0.21	0.36	0.48	0.96	0.92	0.06
	HH2	0.45	0.28	0.31	0.99	0.86	0.11
	Impurities	Hf					
$x = 0.15$	Overall	0.31	0.34	0.39	0.94	0.88	0.15
	HH1	0.19	0.39	0.45	0.93	0.95	0.08
	HH2	0.65	0.17	0.15	1.10	0.35	0.59
	Impurities	Sn					
$x = 0.2$	Overall	0.30	0.34	0.39	0.94	0.83	0.21
	HH1	0.18	0.40	0.45	0.93	0.95	0.09
	HH2	0.60	0.15	0.24	1.09	0.29	0.65
	HH3	0.17	0.28	0.58	1.00	0.95	0.04
	Impurities	Sn, Hf					
$x = 0.3$	Overall	0.27	0.36	0.39	0.93	0.78	0.28
	HH1	0.27	0.36	0.41	0.93	0.81	0.24
	Impurities	$(Zr,Hf)Sn_2$, $(Zr,Hf)_2Sn_3$					
$x = 0.4$	Overall	0.29	0.31	0.44	0.98	0.59	0.38
	HH1	0.16	0.38	0.52	0.98	0.81	0.16
	HH2	0.41	0.17	0.38	1.16	0.26	0.62
	Impurities	(Ti,Zr)Sn, $(Zr,Hf)_2Sn_3$					
$x = 0.5$	Overall	0.38	0.35	0.28	0.84	0.25	0.90
	HH1	0.38	0.26	0.35	1.05	0.36	0.60
	HH2	0.45	0.18	0.30	1.12	0.23	0.71
	Impurities	$(Ti,Zr)_3Sn_2$, $ZrSn_2$					

7.2 Transport properties

Substitution of Sn for Sb in *p*-type $Ti_{0.3}Zr_{0.35}Hf_{0.35}CoSb_{1-x}Sn_x$ introduces holes in the system; therefore, the concentration of the main charge carriers is increased. Even

though EDX analysis revealed small amounts of binary impurity phases for samples with $x \geq 0.3$, the carrier concentration increases systematically with increasing substitution level x as shown in Figure 7.3(a). However, these do not affect the net charge carrier concentration. For comparison, the nominal carrier concentration was calculated for each composition with assuming that the doping of one Sn atom introduces one hole to the system starting from the experimentally determined n of the sample with $x = 0.1$. Since the experimentally estimated carrier concentration is in good agreement with the calculation, it reflects the intrinsic electronic state of the main phase.

As one expects from the increased carrier concentration, the electrical conductivity σ increases with increasing substitution level x (see Figure 7.2). The temperature dependence shows a decrease of σ with increasing temperature, indicating metal-like behavior of samples with $x = 0.1 - 0.2$. The sample with $x = 0.3$ shows a maximum around 200°C. Whereas the sample with $x = 0.5$ shows a semiconducting behavior. Samples with $x \geq 0.3$ contain additional binary impurity phases (compare Table 7.1) indicating that a maximum substitution level is reached with 20% Sn. The presence of these inclusions reduces the mobility by scattering of the main charge carriers leading to different electronic properties as in the samples with solely half-Heusler phases.
The Seebeck coefficients (see Figure 7.2(b)) are highest for $x = 0.1$ and decrease with increasing Sn content, as one can expect from the interrelation of the electronic transport properties.
The thermal conductivity increases with increasing Sn content (see Figure 7.2(c)), and the temperature dependence is also effected. Samples with $x = 0.10 - 0.2$ show a decrease with increasing temperature, whereas samples with $x = 0.3$ show nearly temperature-independent behavior, and the thermal conductivity of samples with $x = 0.4$ and 0.5 increases. To explain this behavior, the lattice thermal conductivity κ_{lat} was calculated by subtracting the electronic contribution estimated by assuming the Wiedemann–Franz law (Equation 3.14) from the total thermal conductivity. The Lorentz number L was approximated by Equation 3.15. All samples showed a decrease in κ_{lat} with increasing temperature, suggesting that they are in the range where the lattice thermal conductivity is dominated by the phonon-phonon scattering. The temperature dependence of κ_{lat} for samples with $x \geq 0.3$ is much weaker than for samples with $x \leq 0.2$, leading to a nearly glass-like behavior. Nevertheless, the increase in the total thermal conductivity κ is mainly due to the increasing electronic contribution for $x \geq 0.3$.

To visualize the effect of the substitution level x, the thermoelectric properties at 610°C versus the carrier concentration n are plotted in Figure 7.3(b). The figure shows, that $Ti_{0.3}Zr_{0.35}Hf_{0.35}CoSb_{1-x}Sn_x$ can be regarded as a model system for the interdependence of the thermoelectric properties via the carrier concentration, like the illustrations found in fundamental review articles on thermoelectric materials [32, 48]. It proves that the best compromise for high power factors is reached at $x = 0.15$, which yields the maximum figure of merit $ZT = 0.79$. This is an enhancement of 40% compared to 0.57 for $x = 0.1$ or $x = 0.2$. The thermoelectric properties were improved significantly simply by filling the gap between those two substitution levels. The conformity of the experimental data with the theoretical predictions is picture-book like, suggesting that unlike the more complicated MNiSn system [11] a single parabolic band-model can be

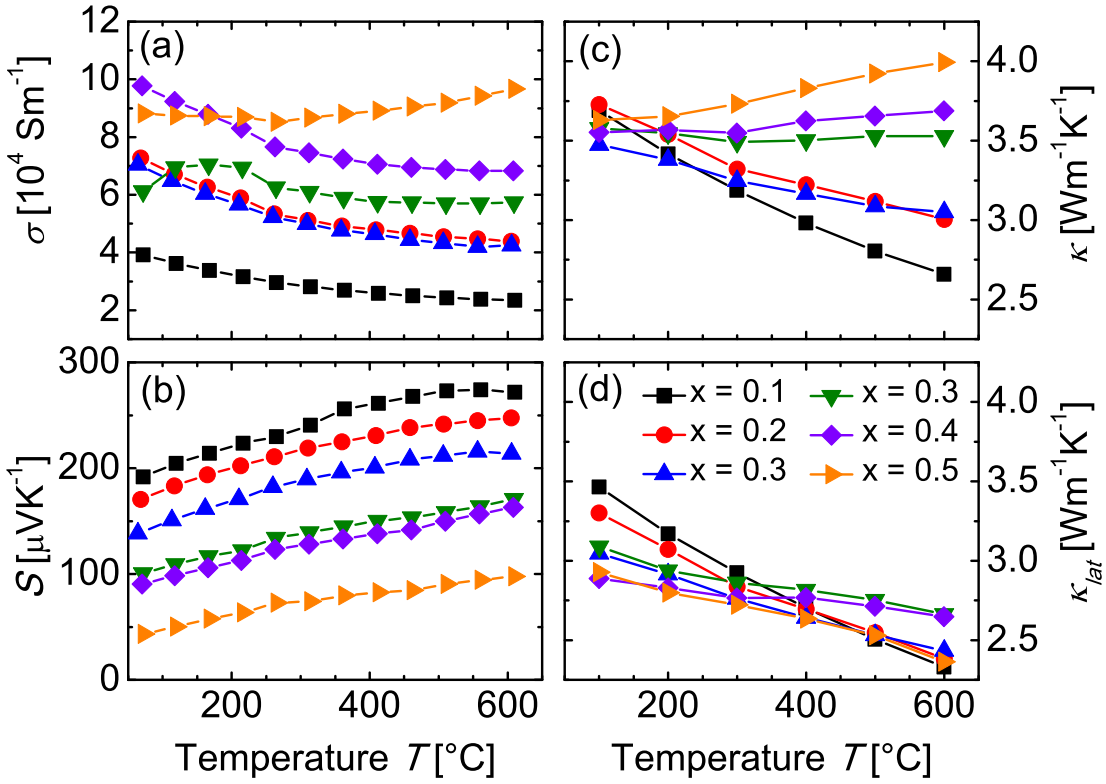

Figure 7.2: (a) Electrical conductivity σ, (b) Seebeck coefficient S, (c) thermal conductivity κ, and (d) lattice thermal conductivity κ_{lat} as a function of temperature for $Ti_{0.3}Zr_{0.35}Hf_{0.35}CoSb_{1-x}Sn_x$.

assumed to tune the carrier concentration. It is a powerful tool to further enhance the thermoelectric performance in this system with a given composition M.

7.3 Conclusion

The carrier concentration in the p-type half-Heusler compound $Ti_{0.3}Zr_{0.35}Hf_{0.35}CoSb_{1-x}Sn_x$ was optimized, which is a fundamental approach to enhance the performance of thermoelectric materials. The experimentally very simple approach of plotting the transport properties against the carrier concentration is a powerful tool to further enhance the thermoelectric performance of $MCoSb_{1-x}Sn_x$. The optimum carrier concentration is reached with a substitution level $x = 0.15$ of Sn, which yields the maximum power factor, 2.69×10^{-3} $Wm^{-1}K^{-2}$, and maximum figure of merit ZT of 0.8 are reached at $x = 0.15$. This corresponds to a carrier concentration of 1.4×10^{21} cm^{-3}. To verify the intrinsic phase separation, this sample was analyzed in detail by SEM, EDX analysis, and high resolution PXRD with synchrotron radiation. By adjusting the carrier concentration, an enhancement of about 40% in the power factor and figure of merit ZT was

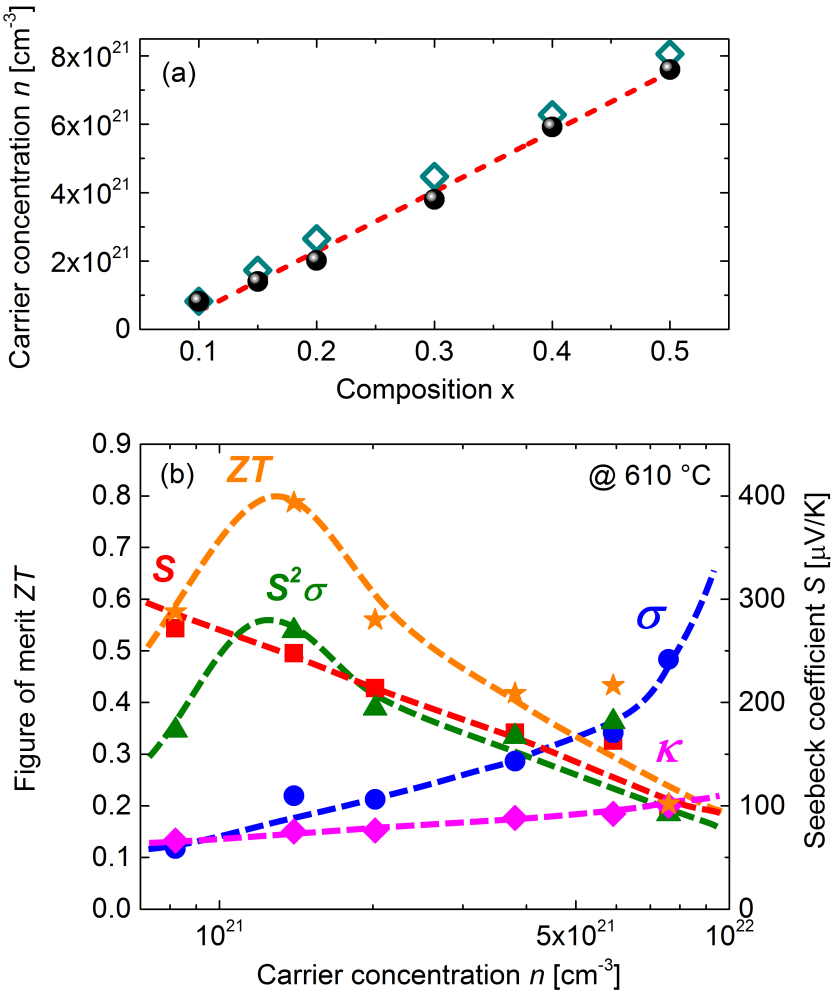

Figure 7.3: (a) Carrier concentration n as a function of substitution level x in $Ti_{0.3}Zr_{0.35}Hf_{0.35}CoSb_{1-x}Sn_x$ (●) in comparison with the calculated nominal carrier concentration (◇) and (b) thermoelectric properties as a function of the carrier concentration n at 610°C. Plotted are Seebeck coefficients (S ■ in the range from 0 to 450 μVK^{-1}), electrical conductivity σ (●, 0 – 18×10^{-4} Sm^{-1}), power factors $S^2\sigma$ (▲, 0 – 4.5×10^{-3} $Wm^{-1}K^{-2}$), thermal conductivity κ (♦, 0 – 18 $WK^{-1}m^{-1}$), and figure of merit ZT (★, 0 – 0.9).

achieved compared to samples with $x = 0.1$ or 0.2 simply by choosing a substitution level between those of these two samples. Thus, a Sn content of 15% as a starting point for subsequent enhancements by varying the composition M is suggested, instead of using the previous $Zr_{0.5}Hf_{0.5}CoSb_{0.8}Sn_{0.2}$, which has a ZT of 0.5 at 1000 K [21]. Based on this approach, the efficiency of phonon scattering as well as the electronic properties can be improved further by a fine-tuning of the Ti to Hf ratio, as demonstrated in the next Chapter.

8 Fine tuning of thermoelectric performance

A fine tuning of thermoelectric performance in phase-separated half-Heusler compounds via the adjustment of the Ti to Hf ratio in $Ti_{1-x}Hf_xCoSb_{0.85}Sn_{0.15}$ is possible and the resulting TE properties correlate to the results of the structural investigations. Two succesful recipes to enhance the thermoelectric performance, namely carrier concentration optimization and reduction of thermal conductivity, have been combined and applied to the *p*-type (Ti/Zr/Hf)$CoSb_{1-x}Sn_x$ system. An intrinsic micrometer-scale phase separation increases the phonon scattering and reduces the lattice thermal conductivity. To accomplish this, alloying of Ti together with Hf is mandatory. A substitution of 15% Sb by Sn optimizes the electronic properties. Starting from this, further improvement of the thermoelectric properties has been achieved by a fine tuning of the Ti to Hf ratio. A detailed study of the *p*-type half-Heusler compounds $Ti_{1-x}Hf_xCoSb_{0.85}Sn_{0.15}$ using high-resolution synchrotron powder X-ray diffraction and element mapping electron microscopy succeded in a record thermoelectric figure of merit for *p*-type half-Heusler compounds of $ZT \approx 1.2$ at 710°C in $Ti_{0.25}Hf_{0.75}CoSb_{0.85}Sn_{0.15}$. The phase separation approach can form a significant alternative to nanostructuring processing, saving time, energy consumption and increasing the thermoelectric efficiency.

Table 8.1: Composition of the matrix (I) and second half-Heusler phases (II) of the samples $Ti_{1-x}Hf_xCoSb_{0.85}Sn_{0.15}$ as determined by EDX spectroscopy. Experimental density ρ [g cm^{-3}], carrier concentration n_H [10^{21} cm^{-3}], and Hall mobility μ_H [10^2cm^{2}V^{-1}s^{-1}] at 300 K.

Nominal composition	Phase	EDX	ρ	n_H	μ_H
$TiCoSb_{0.85}Sn_{0.15}$	I	$Ti_{1.07}Co_{0.98}Sb_{0.91}Sn_{0.05}$	7.312	0.780	1.734
	II	$Ti_{0.97}Co_{1.18}Sb_{0.28}Sn_{0.57}$			
$Ti_{0.75}Hf_{0.25}CoSb_{0.85}Sn_{0.15}$	I	$Ti_{0.79}Hf_{0.25}Co_{0.97}Sb_{0.94}Sn_{0.04}$	8.161	1.093	2.325
	II	$Ti_{0.95}Hf_{0.09}Co_{1.06}Sb_{0.36}Sn_{0.55}$			
$Ti_{0.5}Hf_{0.5}CoSb_{0.85}Sn_{0.15}$	I	$Ti_{0.44}Hf_{0.55}Co_{1.02}Sb_{0.94}Sn_{0.05}$	8.983	0.995	2.794
	II	$Ti_{0.80}Hf_{0.21}Co_{1.07}Sb_{0.33}Sn_{0.59}$			
$Ti_{0.25}Hf_{0.75}CoSb_{0.85}Sn_{0.15}$	I	$Ti_{0.17}Hf_{0.79}Co_{1.01}Sb_{0.98}Sn_{0.06}$	9.849	0.916	3.492
	II	$Ti_{0.60}Hf_{0.38}Co_{1.09}Sb_{0.27}Sn_{0.66}$			
$Ti_{0.15}Hf_{0.85}CoSb_{0.85}Sn_{0.15}$	I	$Ti_{0.10}Hf_{0.86}Co_{1.03}Sb_{0.94}Sn_{0.07}$	9.705	1.237	4.282
	II	$Ti_{0.47}Hf_{0.48}Co_{1.11}Sb_{0.29}Sn_{0.65}$			
$HfCoSb_{0.85}Sn_{0.15}$	I	$Hf_{0.93}Co_{1.02}Sb_{0.97}Sn_{0.08}$	10.581	1.480	4.965
	II	$Hf_{0.86}Co_{1.19}Sb_{0.26}Sn_{0.69}$			

8.1 Microstructure investigations

The investigations of the samples by PXRD, SEM, and EDX spectroscopy confirmed that samples containing Ti and Hf undergo an intrinsic phase separation into two half-Heusler phases. The composition of the matrix (phase I) and the second half-Heusler phase (phase II) as determined by EDX spectroscopy are indicated in Table 8.1.

In general, the matrix is rich in Hf and Sb whereas the second phase is rich in Ti and Sn when compared with the nominal composition. Moreover, this second phase has a slight excess of Co. It can be assumed that the Co atoms occupy the vacant tetrahedral holes in the structure that is similar to the $L2_1$ Heusler compound Co_2TiSn [170]. This assumption is supported by a recent report on the in-situ growth of Heusler quantum dots in the half-Heusler $Ti_{0.5}Hf_{0.5}CoSb_{0.8}Sn_{0.2}$ matrix [165]. In addition, very small amounts of the pure elements Ti, Sn or Hf or a binary Ti_ySn_z were detected. These results agree well with the previous investigations of the phase separation in the $(Ti/Zr/Hf)CoSb_{0.8}Sn_{0.2}$ system (see chapter 6)

The typical microstructure of the samples is displayed in the backscattered electron images (BSE) in Figures 8.1(a)-(f). The amount and shape of the second half-Heusler phase depends on the ratio of Ti to Hf. Samples with $0.75 \geq x \geq 0.25$ show a fine network of the second phase within the matrix. The most distinctive formation is observed for the composition with $x = 0.25$. Upon decreasing the amount of Ti further ($x = 0.85$), the amount of the second half-Heusler phase becomes too less to form an interconnecting network.

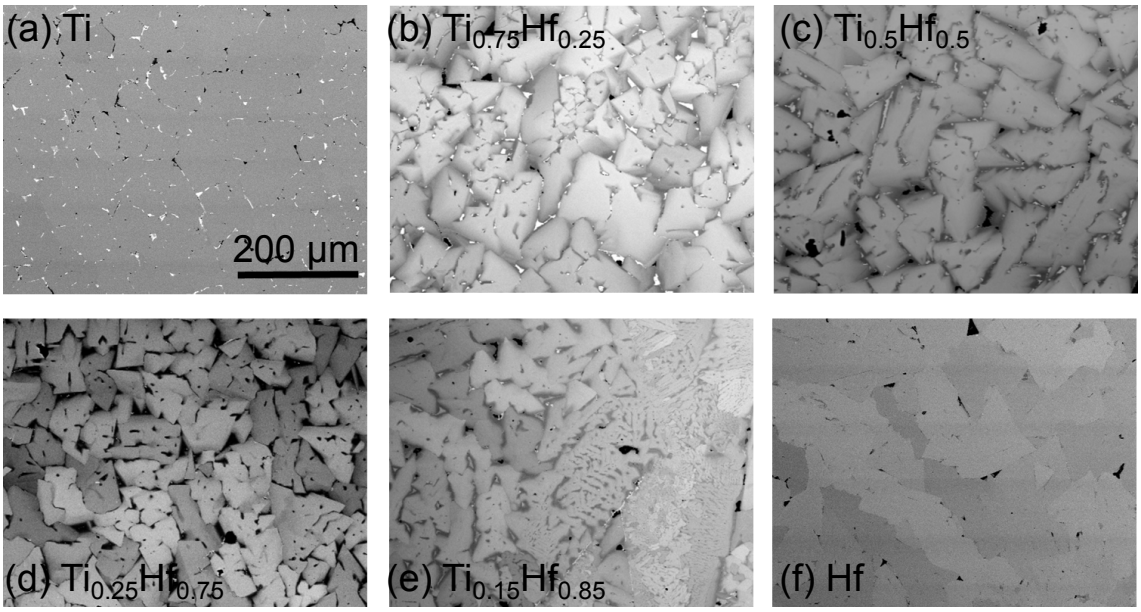

Figure 8.1: Backscattered electron images of $Ti_{1-x}Hf_xCoSb_{0.85}Sn_{0.15}$ with the indicated ratios of Ti to Hf. The matrix (mid-scale grey) is interlaced by a second half-Heusler phase (dark regions), and the bright spots indicate Sn inclusions.

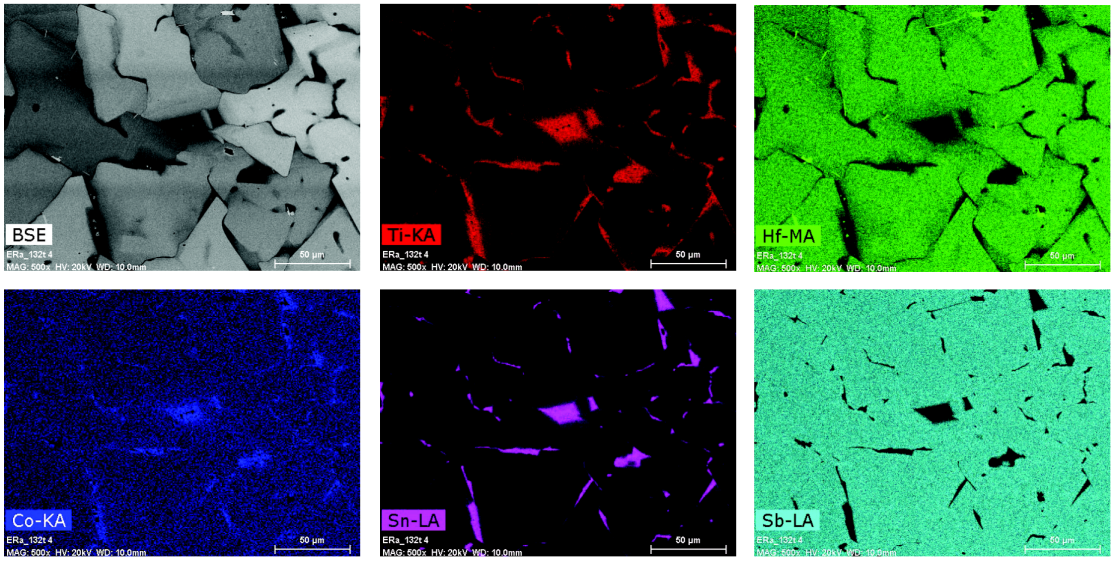

Figure 8.2: Element-specific EDX mapping of the sample $Ti_{0.25}Hf_{0.75}CoSb_{0.85}Sn_{0.15}$.

The element-specific EDX mappings (see Figure 8.2 for the sample with x = 0.25) confirm that the second half-Heusler phase is rich in Ti and Sn and exhibits a slight excess of Co. The images of the distributions of these three elements all appear similar, whereas the element-specific mappings for Hf and Sb appear as "negatives" of the images of the other three elements.

X-ray diffraction patterns of the substitution series $Ti_{1-x}Hf_xCoSb_{0.85}Sn_{0.15}$ using a Cu$K_{\alpha 1}$ lab source confirmed the presence of half-Heusler structure $C1_b$ in all compounds despite the presence of a marginal amount of β-Sn close to the detection limit. Figure 8.3(a) shows the representative PXRD pattern of $HfCoSb_{0.85}Sn_{0.15}$ with the indexed reflections. However, high-resolution PXRD with synchrotron radiation revealed the existence of a multiphase state in samples with $0.25 \leq x \leq 0.85$, thus confirming phase separation into different half-Heusler phases, as observed by EDX analysis. Samples with a single element Ti ($x = 0$) or Hf ($x = 1$) exhibited sharp and symmetric Bragg reflections, thereby indicating the presence of only one phase with the $C1_b$ structure. The reflections for a composition of $x = 0.15$ show very little broadening of the peaks. In contrast, the splitting of the main reflection (220) becomes very obvious for samples with $0.25 \leq x \leq 0.75$ [see Figure 8.3(b)] due to the presence of several half-Heusler phases. For example, the fitting of the powder pattern of $Ti_{0.5}Hf_{0.5}CoSb_{0.85}Sn_{0.15}$ requires at least the presence of five different half-Heusler phases with very similar lattice parameters a [see Figure 8.3(c)]. As an initial step, the compositions of the two half-Heusler phases, that were distinguishable by EDX spectroscopy (see Table 8.1), were used to refine the lattice parameters from the PXRD patterns. Since the composition varies slightly in the matrix as well as in the second half-Heusler phase, this leads to the observation of

a multiphase state in the high-resolution PXRD patterns. Subsequently, more phases with the $C1_b$ structure were added to model the shape of the (220) reflection correctly.

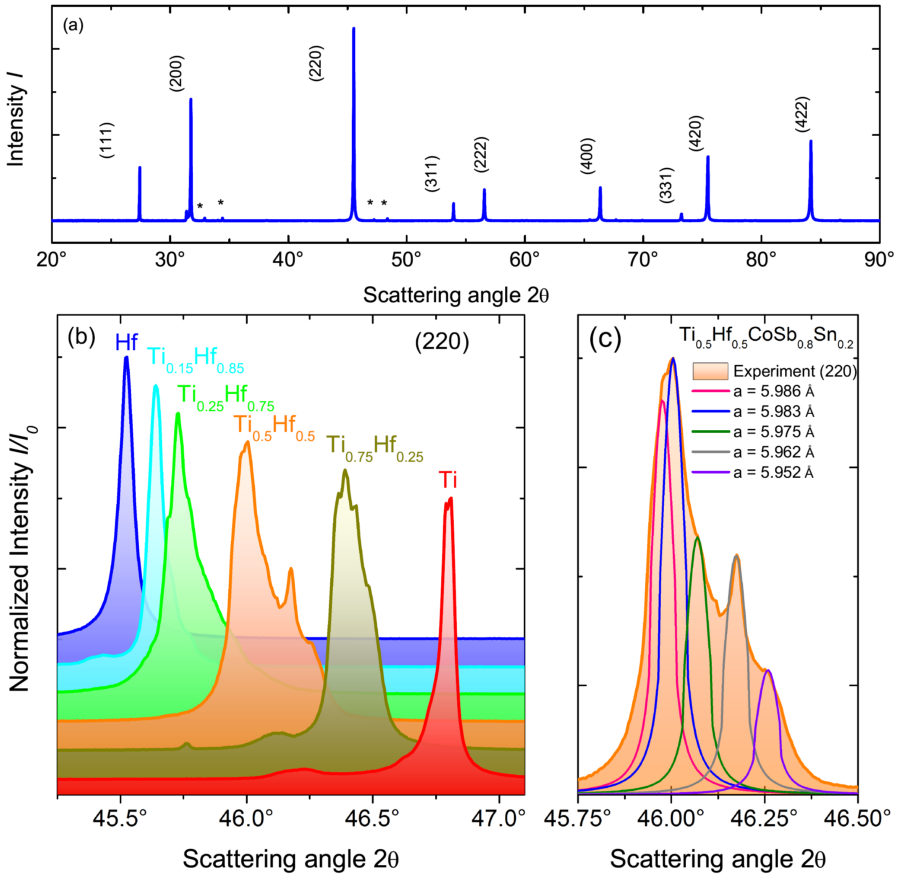

Figure 8.3: PXRD patterns obtained using synchrotron radiation (λ =1.65307 Å). (a) $HfCoSb_{0.85}Sn_{0.15}$ (* indicates β-Sn), (b) main reflection (220) of $Ti_{1-x}Hf_xCoSb_{0.85}Sn_{0.15}$ with the indicated ratios of Ti to Hf, and (c) fitting of the (220) reflections for $Ti_{0.5}Hf_{0.5}CoSb_{0.85}Sn_{0.15}$.

8.2 Thermoelectric properties

The thermal conductivity plots of the investigated compounds are displayed in Figure 8.4. These values are highest for single-phase samples with $x = 0$ and $x = 1$. The thermal conductivity is effectively suppressed by the intrinsic phase separation and depends on the microstructuring of the samples. All samples with a Hf content of $0.25 \leq x \leq 0.75$ exhibit very similar thermal conductivities. The values are nearly temperature-independent, thereby indicating a glass-like behavior. A slightly higher thermal conduc-

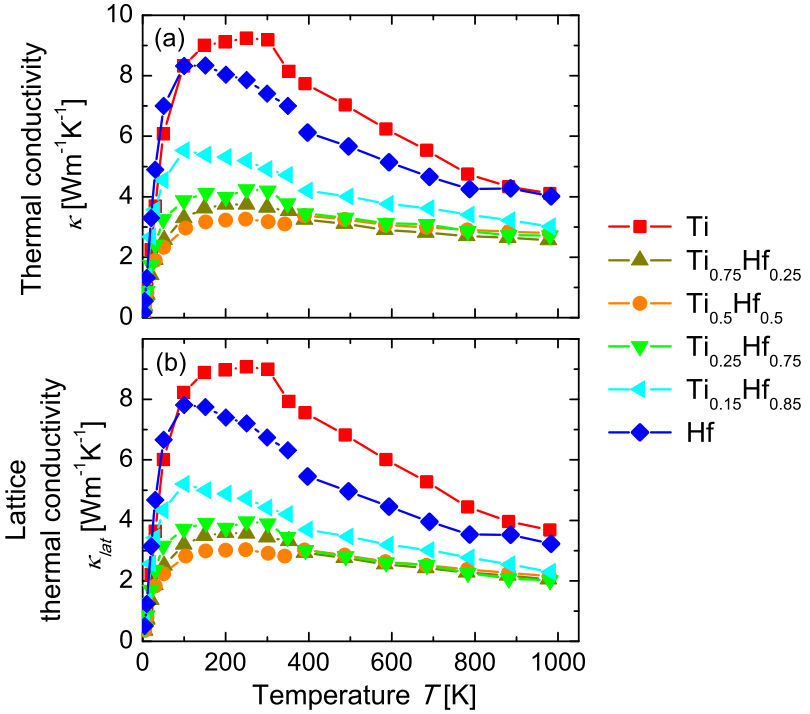

Figure 8.4: (a) Thermal conductivity κ, and (b) lattice thermal conductivity κ_{lat} as functions of temperature for $Ti_{1-x}Hf_xCoSb_{0.8}Sn_{0.15}$ for the indicated ratios of Ti to Hf. Data up to 350 K were obtained from TTO PPMS measurements, high-temperature data were calculated from LFA measurements.

tivity was observed for samples with $x = 0.85$. To further examine the impact of the substitution level, the lattice thermal conductivity by applying the Wiedemann–Franz law was calculated. The Lorentz number was estimated with equation 3.15. As displayed in Figure 8.4(b), the lowest κ_{lat} values were reached by the samples with $x = 0.25$ (2.01 $Wm^{-1}K^{-1}$ at 980 K), $x = 0.5$ (2.16 $Wm^{-1}K^{-1}$), and $x = 0.75$ (2.05 $Wm^{-1}K^{-1}$). The formation of a interconneting network of second half-Heusler phase within the matrix, leads to an effective reduction of the lattice thermal conductivity. In contrast samples with Hf content of $x = 0.85$ exhibited the highest lattice thermal conductivity among all phase-separated samples (2.30 $Wm^{-1}K^{-1}$ at 980 K).

In this samples the amount of the secondary half-Heusler phase is so small, that it cannot form a interconnecting network through the matrix anymore. This agrees well with the results from the high-resolution PXRD. The shape and width of the (220) reflection for $x = 0.85$ is similar to that of the single phase samples in contrast to the splitting of the main reflection for samples with $0.25 \leq x \leq 0.75$. Therefore, phonon scattering is most effective in the sample with $x = 0.75$ corresponding to a reduction of 45% in the lattice thermal conductivity when compared with that of the single-phase $TiCoSb_{0.85}Sn_{0.15}$.

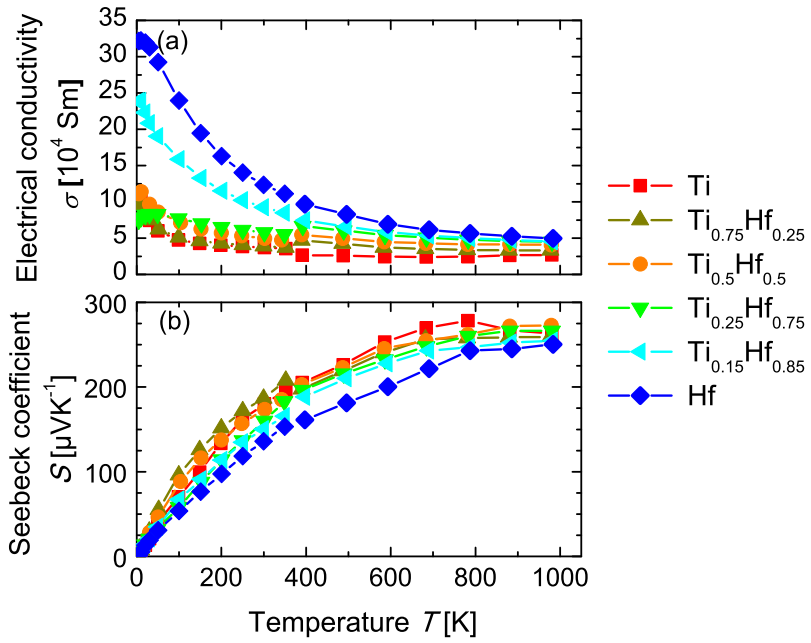

Figure 8.5: (a) Electrical conductivity σ and (b) Seebeck coefficient S as functions of temperature for $Ti_{1-x}Hf_xCoSb_{0.85}Sn_{0.15}$ with the indicated ratio of Ti to Hf. Data up to 350 K were obtained from TTO PPMS measurements, high-temperature from LSR measurements.

Figure 8.5(a) shows the temperature dependency of the electrical conductivity σ, for all the samples. All samples exhibit a metallic behavior, i.e., the conductivity decreases with increasing temperature. Upon substitution of Ti with its heavier homologue Hf, σ is enhanced. Due to the interrelation of the Seebeck coefficient with σ, the Seebeck coefficients also shows a decrease upon substitution. The maximum Seebeck coefficient was observed for $TiCoSb_{0.85}Sn_{0.15}$, with a value of 278 μVK^{-1} at 780 K. This maximum is shifted to higher temperatures upon substitution of Ti by Hf. Even though the substitution is isoelectronic, it changes the electronic structure and consequently affects the carrier concentration and effective mass of the charge carriers. The carrier concentration n_H and mobilities μ_H at room temperature are listed in table 8.1. Substitution of Ti by its heavier homologue Hf leads to an increase of n_H as well as of μ_H. Certainly, the impact is small as compared to doping with holes by replacing Sb with Sn, that leads to an increase in n_H with a factor 4 times the substitution level [171]. Regardless, in the cleary phase-separated samples with $x = 0.5$ and 0.75, n_H as well as μ_H are smaller than one would expect, if one assumes a linear increase with substitution level x. As a consequence the Seebeck coeffiecients are decreased with increasing Hf content, but the phase separation attenuates this effect. In contrast, the electrical conductivity is not affected by the phase separation because the increasing mobility is compensating for the carrier concentration.

The calculation of the power factor $S^2\sigma$ reveals that the optimal electronic properties are obtained for samples with a Hf content of 50% and more. At 980 K, power factors between 2.93 $mWK^{-2}m^{-1}$ ($x = 0.15$) and 3.18 $mWK^{-2}m^{-1}$ ($x = 0.25$) are reached. These values correspond to a power factor enhancement of 89% with respect to that of $TiCoSb_{0.85}Sn_{0.15}$ (1.68 $mWK^{-2}m^{-1}$ at 980 K).

Figure 8.6 visualizes that fine-tuning of the Ti–Hf ratio has a significant impact on the figure of merit ZT. By simply mixing Ti and Hf together in a 50% ratio, ZT shows a immediate improvement by 42% compared to the sample with only Hf. Since both samples exhibit similar power factors, this improvement is due to reduction in the lattice thermal conductivity by intrinsic phase separation. Adjustment of the ratio of Ti to Hf enhances ZT further. The selection of the optimal electronic properties in combination with the lowest thermal conductivity leads to the maximum figure of merit of $ZT \approx 1.2$ at 710°C for $Ti_{0.25}Hf_{0.75}CoSb_{0.85}Sn_{0.15}$. This value clearly exceeds the benchmark of $ZT \approx 1$ for device applications [6]. This result can be considered as very significant for bulk p-type half-Heuslers. When compared with the previous state-of-the-art material, e.g., $Ti_{0.12}Zr_{0.44}Hf_{0.44}CoSb_{0.8}Sn_{0.2}$ [151] with $ZT = 0.98$ at 700°C, this value corresponds to an improvement of 19%. Considering only ingot samples prepared by a simple arc melting fabrication process as in reference [21], the enhancement of the figure of merit exceeds 125% by our combined approach of phase separation and carrier concentration adjustment.

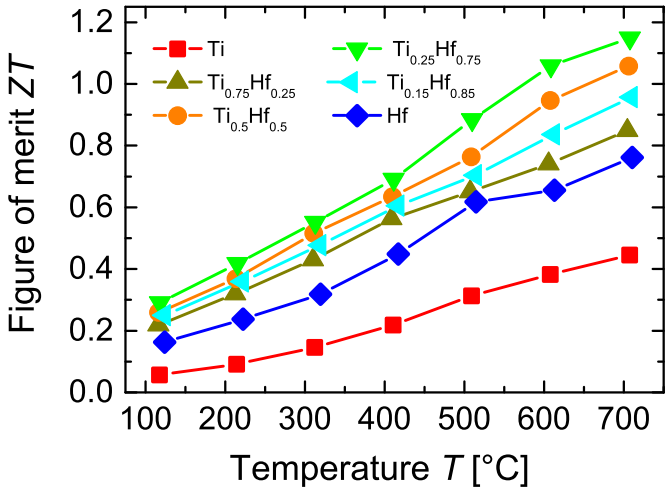

Figure 8.6: Figure of merit ZT as a function of temperature for $Ti_{1-x}Hf_xCoSb_{0.8}Sn_{0.15}$ for the indicated ratios of Ti to Hf.

8.3 Conclusions

Two concepts were successfully applied to improve the thermoelectric properties of the *p*-type TiCoSb system. Starting from $Ti_{0.5}Hf_{0.5}CoSb_{0.8}Sn_{0.2}$, it was shown that phase separation ($ZT = 0.9$ at 710°C [23]) affords thermoelectric properties that are similar to those obtained with nanostructuring approach involving ball milling [3]. In the second step, the optimization of the carrier concentration led to an improvement of about 25% as regards the figure of merit in $Ti_{0.5}Hf_{0.5}CoSb_{0.85}Sn_{0.15}$ ($ZT = 1.05$). Based on these two concepts a fine tuning of the Ti to Hf ratio for optimum phonon scattering in combination with optimum electronic properties, a record ZT of 1.2 at 710°C was achieved with the composition $Ti_{0.25}Hf_{0.75}CoSb_{0.85}Sn_{0.15}$. When compared with the ZT value of the previous state-of-the-art *p*-type half-Heusler material, $Ti_{0.12}Zr_{0.44}Hf_{0.44}CoSb_{0.8}Sn_{0.2}$ [151] with a $ZT \approx 1.0$ at 700°C, this value corresponds to an improvement of 20%. In conclude, a bulk *p*-type half-Heusler material with TE performance as good as the state-of-the art *n*-type $Ti_{0.5}Zr_{0.25}Hf_{0.25}NiSn_{0.998}Sb_{0.002}$ ($ZT = 1.2$ at 560°C) [14] was realized. As both materials are compatible and perform well together in one TE module [5], TE devices based on phase-separated half-Heusler compounds are very promising for applications in the mid-temperature range.

9 Long-term stability upon thermal cycling

The recovery of industrial and automotive waste heat are possible fields of applications for thermoelectric devices based on half-Heusler compounds in the mid-temperature range. In both cases, the operation conditions impose thermal stress upon the material. For example, a thermoelectric generator integrated to an automotive exhaust pipe operates in the temperature range from 100 to 700°C, being heated and cooled multiple times during the driving process [172]. However, these systematic investigations mainly focus on the impact of thermal cycling upon the thermoelectric generators. For example, the evaluation of a thermoelectric module consisting of a W-doped Heusler Fe_2VAl alloy [173] and the long-term stability of half-Heusler modules produced in large quantities [5] were reported.
In general, the durability of the entire thermoelectric module, especially in terms of the stability of the electrical contacts, is tested. The increase in internal resistance with increasing contact resistance as a result of the formation of microcracks in the vicinity of leg-solder interface is very common [174]. Inexplicably, the effect of thermal cycling on the thermoelectric material itself is mostly neglected. A few investigations of bismuth tellurides [175, 176] and skutterudites [177, 178] can be found. The most detailed study on thermocyclic stability has the actual purpose of finding a standard reference material for Seebeck coefficient measurements comparing constantan to SiGe [179].
Very recently, the long-term stability of *n*- and *p*-type half-Heusler materials based on $Ti_{0.3}Zr_{0.35}Hf_{0.35}NiSn$ was investigated by *Krez et al.* [157]. The properties were stable even after 500 cycles of repeated heating and cooling from 100 to 600°C and the dendritic microstructure consisting of Ti-poor and Ti-rich half-Heusler phases was stable under the long-term cycling. Regardless, there is still room for improvement because the maximum ZT values reported by Krez et al. are 0.7 at 600°C for *n*-type and 0.4 at 400°C for *p*-type.

The materials properties were optimized sucessfully for state-of-the-art *p*-type half-Heusler compounds, which are all found within the $(Ti/Zr/Hf)CoSb_{1-x}Sn_x$ system [2, 3, 59, 151] in Chapters 6, 7, and 8. Towards applications the stability under cycling conditions is an important aspect, that should not be neglected. Therefore, the reliability of the thermoelectric performance was tested on a laboratory scale.
Three different compositions, $Ti_{0.5}Hf_{0.5}CoSb_{0.8}Sn_{0.2}$ [23], $Ti_{0.5}Hf_{0.5}CoSb_{0.85}Sn_{0.15}$ [59], and $Ti_{0.12}Zr_{0.44}Hf_{0.44}CoSb_{0.8}Sn_{0.2}$ [151], were chosen for comparison and investigated the impact of repeated heating and cooling on the thermoelectric performance and structural properties in detail.

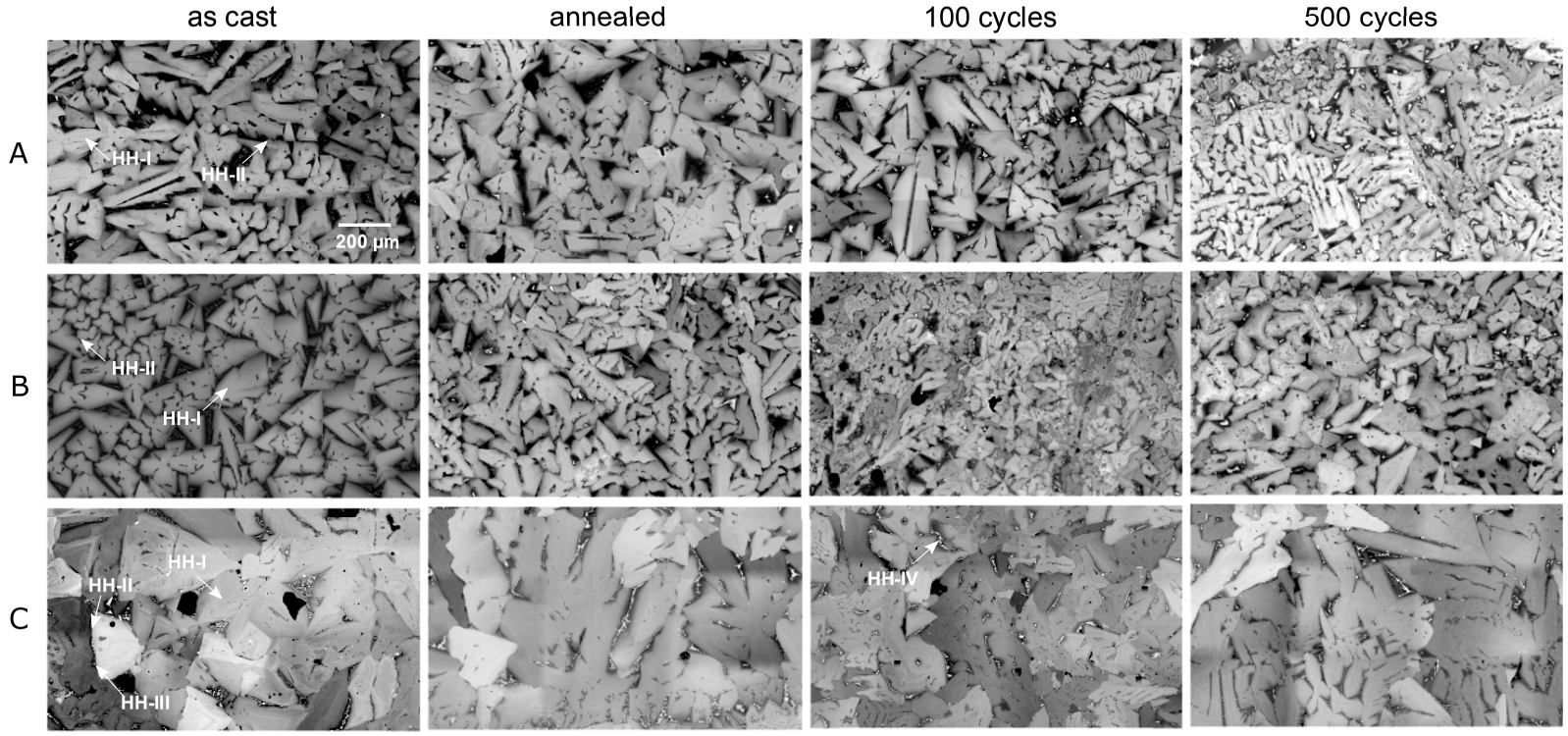

Figure 9.1: BSE images displaying the evolution of the microstructure upon thermal cycling of sample (A) $Ti_{0.5}Hf_{0.5}CoSb_{0.8}Sn_{0.2}$, (B) $Ti_{0.5}Hf_{0.5}CoSb_{0.85}Sn_{0.15}$, and (C) $Ti_{0.12}Hf_{0.44}Zr_{0.44}CoSb_{0.8}Sn_{0.2}$.

9.1 Experimental details

Ingots of 15 g with compositions of $Ti_{0.5}Hf_{0.5}CoSb_{0.8}Sn_{0.2}$ (A), $Ti_{0.5}Hf_{0.5}CoSb_{0.85}Sn_{0.15}$ (B), and $Ti_{0.12}Zr_{0.44}Hf_{0.44}CoSb_{0.8}Sn_{0.2}$ (C) were prepared by arc melting of stoichiometric amounts of the elements (see Chapter 4). The as-cast samples were cut into discs and bars suitable for the characterization of the thermoelectric properties. Subsequently, they were annealed in quartz glass ampules under vacuum at 900°C for 7 days followed by quenching in ice water. Afterwards, the long-term stability and thermoelectric performance was investigated under thermal cycling conditions. To accomplish this, the sample pieces were packed into quartz glass ampules under vacuum and a heat treatment of repeating heating and cooling steps was performed. Each cycle consisted of heating from 100°C to 700°C, holding the temperature at 700°C for 10 min and then cooling to 100°C. Heating and cooling rates were 10 K/min. For each composition, the experiments were performed for four samples from two different batches to ensure the repeatability.

Structural investigations by PXRD and SEM in combination with EDX spectroscopy, as well as determination of the thermoelectric properties, were performed for the as-cast samples after annealing and after 50, 100, and 500 cycles. For each measurement of the transport properties the same piece of the sample was used. After finishing 500 cycles, those pieces were also prepared for the structural investigations by PXRD and SEM.

9.2 Stability under thermal cycling conditions

9.2.1 Structural properties

Structural investigations by SEM and EDX as shown in Figure 9.1 prove that all samples undergo an intrinsic phase separation into two half-Heusler phases. The characteristic microstructure is already obtained in the as-cast samples and is not effected by the consequent annealing step. The composition of the phases, as analized by EDX spectroscopy, does not change upon the prolonged heat treatment. The numbers given in Tabel 7.1 represent an average of the data obtained after every step of the cycling process. The standard deviations lie between 0.005 and 0.04, which is within the error range of the method. Samples A and B both exhibit a matrix (HH-I) rich in Hf and Sb as compared to the nominal composition, which is interlaced by a second half-Heusler phase rich in Ti and Sn (HH-II). Remarkably, it is found that the phases in A and B have nearly the same composition, indicating that those are stable phases. Only the ratio of the phases differs (see Table 9.1). Sample B contains less HH-II phase, which correlates to the minor amount of Sn compared to sample A. On the other hand, A contains more Sn inclusions (bright spots). Nevertheless, the phase separation is stable under thermal cycling conditions, even though the excess Sn inclusions tend to accumulate over time in sample A, indicating that an amount of 20% Sn can be considered as overdoped. In summary, for long-term stability, a reduced amount of only 15% Sn is desirable. Apart from that, the BSE images of both compositions look identical and the amount of second

half-Heusler phase remains constant over the heat-treatment period.
Sample C also displays a microstructure consisting of a half-Heusler matrix interspersed with a second Heusler phase. The composition of the matrix HH-I as analyzed by EDX spectroscopy is close to the nominal composition with a little excess of Hf and Sb, whereas the second half-Heusler phase HH-II is rich in Ti and Sn. Nevertheless, additional inclusions (bright spots) of two more half-Heusler phases (HH-III and HH-IV) are observed. No Sn was detected; instead, binary $Zr(Ti/Hf)_xSn_y$ phases (dark inclusion next to HH-III and HH-IV phases) are found. The amount of the HH-II phase in C is less than in A and B, and hence no interconneting network is formed. Upon thermal cycling the microstructure coarsens, leading to a contraction of the HH-II phase around the islands of HH-III and HH-IV. The chosen composition $M = Ti_{0.12}Zr_{0.44}Hf_{0.44}$ is not favorable for achieving an intrinsic phase separation that is stable under thermal cycling conditions. Instead, alloying of Ti with Hf is the key [23]; partial substitution by Zr does not have any advantage. Replacement of Ti by Zr even increases the materials' price because the current metal price for Zr is about 3.5 times higher than that for Ti [180].
The overall composition of all samples as tested by ICP-OES is the same as the initial nominal composition even after 500 cycles. This proves that no evaporation of Sb takes place once the stable half-Heusler phases are formed.

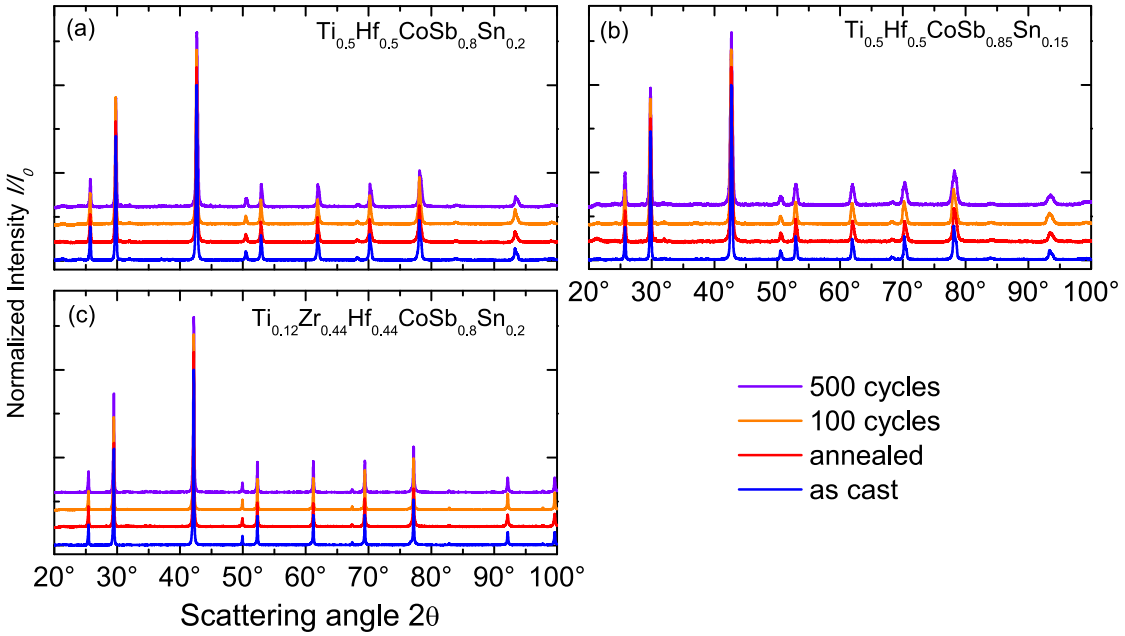

Figure 9.2: PXRD patterns with Cu $K_{\alpha 1}$ radiation of the samples (a) $Ti_{0.5}Hf_{0.5}CoSb_{0.8}Sn_{0.2}$, (b) $Ti_{0.5}Hf_{0.5}CoSb_{0.85}Sn_{0.15}$, and (c) $Ti_{0.12}Zr_{0.44}Hf_{0.44}CoSb_{0.8}Sn_{0.2}$. Displayed are the experimental patterns of as cast, annealed and samples after 100 and 500 cycles. Reflections are indexed according to the half-Heusler structure ($F\bar{4}3m$).

Table 9.1: Composition of the matrix HH-I and second half-Heusler phases HH-II of the samples as determined by EDX spectroscopy, as well as additional half-Heusler phases (HH-III and HH-IV) detected in sample C. Vickers hardness HV0.1 and overall composition determined by ICP-OES after 500 cycles. Listed are lattice parameters a of the half-Heusler phases obtained from PXRD and the area fraction of the HH-II phase (determined from BSE images, indicated in %) as a function of the heat treatment.

(A) $\mathbf{Ti_{0.5}Hf_{0.5}CoSb_{0.8}Sn_{0.2}}$

HH-I	$Ti_{0.44}Hf_{0.62}Co_{0.92}Sb_{0.92}Sn_{0.11}$	
HH-II	$Ti_{0.76}Hf_{0.31}Co_{0.95}Sb_{0.47}Sn_{0.52}$	
ICP-OES	$Ti_{0.51}Hf_{0.46}Co_{1.02}Sb_{0.81}Sn_{0.17}$	
HV0.1	910	
	HH-I	HH-II
as cast	$a = 5.9860$ Å	5.9658 Å (36.6 %)
annealed	$a = 5.9866$ Å	5.9775 Å (36.4%)
100 cycles	$a = 5.9883$ Å	5.9761 Å (37.8%)
500 cycles	$a = 5.9781$ Å	5.9729 Å (37.2%)

(B) $\mathbf{Ti_{0.5}Hf_{0.5}CoSb_{0.85}Sn_{0.15}}$

HH-I	$Ti_{0.42}Hf_{0.65}Co_{0.91}Sb_{0.95}Sn_{0.08}$	
HH-II	$Ti_{0.73}Hf_{0.31}Co_{1.02}Sb_{0.43}Sn_{0.52}$	
ICP-OES	$Ti_{0.49}Hf_{0.50}Co_{1.01}Sb_{0.84}Sn_{0.13}$	
HV0.1	892	
	HH-I	HH-II
as cast	$a = 5.9829$ Å	5.9605 Å (33.0%)
annealed	$a = 5.9811$ Å	5.9590 Å (34.2%)
100 cycles	$a = 5.9843$ Å	5.9581 Å (35.2%)
500 cycles	$a = 5.9810$ Å	5.9548 Å (32.6%)

(C) $\mathbf{Ti_{0.12}Zr_{0.44}Hf_{0.44}CoSb_{0.8}Sn_{0.2}}$

HH-I	$Ti_{0.09}Zr_{0.44}Hf_{0.53}Co_{0.91}Sb_{0.89}Sn_{0.14}$		
HH-II	$Ti_{0.34}Zr_{0.31}Hf_{0.41}Co_{1.01}Sb_{0.29}Sn_{0.65}$		
HH-III	$Ti_{0.64}Zr_{0.36}Hf_{0.31}Co_{0.67}Sb_{0.14}Sn_{0.89}$		
HH-IV	$Ti_{0.04}Zr_{0.06}Hf_{0.92}Co_{0.93}Sb_{0.99}Sn_{0.06}$		
ICP-OES	$Ti_{0.12}Zr_{0.44}Hf_{0.44}Co_{1.01}Sb_{0.79}Sn_{0.21}$		
HV0.1	830		
	HH-I	HH-II	HH-III/IV
as cast	$a = 6.0483$ Å	6.0467 Å (20.4%)	6.0593 Å
annealed	$a = 6.0488$ Å	6.0465 Å (20.8%)	6.0682 Å
100 cycles	$a = 6.0473$ Å	6.0385 Å (19.9%)	6.0590 Å
500 cycles	$a = 6.0464$ Å	6.0391 Å (21.5%)	6.0682 Å

Phase analysis of the PXRD patterns confirm that all samples – as-cast as well as annealed and after all thermal cycling steps – crystallize in the half-Heusler structure (space group F$\bar{4}$3m) and the reflections are broadend owing to the phase separation into two half-Heusler phases (see Figure 9.2). In the $Ti_{0.5}Hf_{0.5}CoSb_{0.8}Sn_{0.2}$ (A) and $Ti_{0.5}Hf_{0.5}CoSb_{0.85}Sn_{0.15}$ (B) samples, a small amount of β-Sn close to the detection limit can be identified. In contrast, the PXRD of $Ti_{0.12}Zr_{0.44}Hf_{0.44}CoSb_{0.8}Sn_{0.2}$ (C) exhibits additional reflections around $2\theta = 34°$, which can be assigned to the binary $Zr(Ti/Hf)_xSn_y$ phases found by EDX spectroscopy. The refinement of the powder patterns confirm the phase separation into two half-Heusler phases, as found in the SEM/EDX studies. The compositions as determined by EDX spectroscopy were used as a starting point and the lattice parameters were refined (see Table 9.1). No change of the lattice parameters is observed upon thermal cycling, confirming the stability of the detected half-Heusler phases.
Vickers hardeness measurements after 500 cycles show that all samples have high mechanical stability, in good agreement with values of n-type half-Heusler materials [164]. This is favorable for the coprocessing of both materials into a thermoelectric module.

9.2.2 Thermoelectric performance

The thermal conductivity of sample A, as displayed in Figure 9.3, is nearly temperature independent, indicating a glass-like behavior. Even though the values are slightly higher than those of a nanostructured ball-milled sample reported in the literature [3], the lattice thermal conductivities coincide with each other. This is attributed to the higher electronic contribution to the thermal conductivity. The thermal conductivities can be regarded as unaffected by the heat treatment because all values lie within the measurement error.
The as-cast sample of composition B exhibits a higher thermal conductivity κ before annealing than after annealing, but the values stabilize and lie within the measurement error after annealing and further heat treatment leads values as low values as those for sample A. Sample C has the highest thermal and lattice thermal conductivity as compared to A und B, even though it contains the heavier homologue Zr replacing Ti. This can be explained by the less effective microstructure of the sample. Additionally, the coarsening of the microstructure upon thermal cycling causes a slight increase of the lattice thermal conductivity after 500 cycles.

All samples show metal-like behavior as the electrical conductivity decreases with increasing temperature [see Figures 9.4 (a)–(c)]. The electrical conductivity of sample A shows a step at 232°C, which corresponds to the melting point of Sn. The height of the step is reduced upon progressive heat treatment. Also, the total value of the electrical conductivity is reduced and approaches the value of sample B. Presumably, the excess Sn melts upon thermal cycling and is stepwise removed from the system, forming small inclusions as observed by SEM or even transported to the surface of the sample. Subsequently, the stable half-Heusler phases remain and the composition and structure approach that of sample B. This assumption is supported by the fact that the electrical conductivity values of sample B are amazingly stable upon thermal cycling.

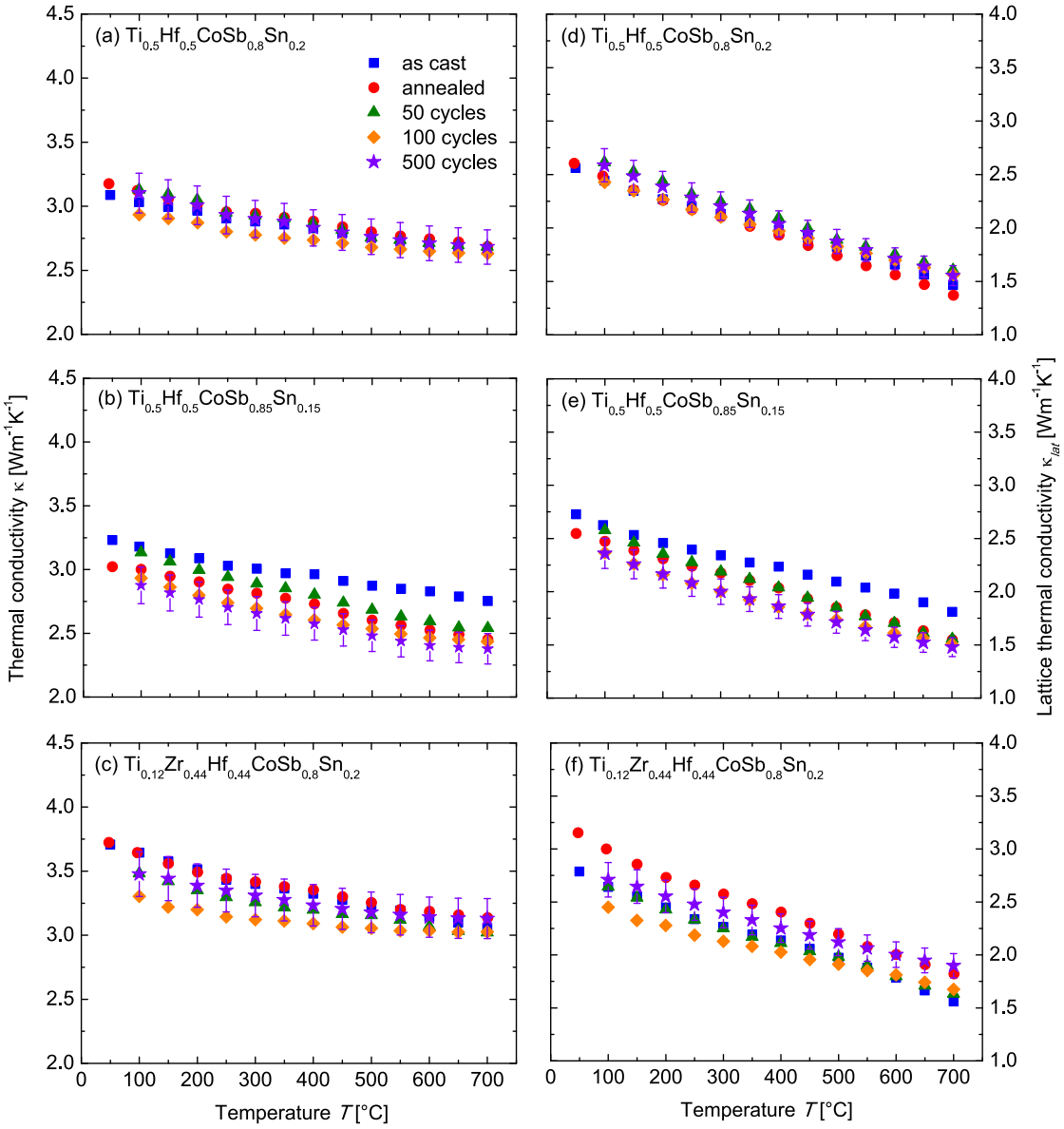

Figure 9.3: Effect of the heat treatment upon (a)–(c) thermal conductivity κ and (d)–(f) lattice thermal conductivity κ_{lat} as a function of temperature. For clarity, only error bars for the measurement after 500 cycles are displayed.

Owing to the interrelation of the Seebeck coefficient with the electrical conductivity, the analogous trends for both samples A and B can be observed in the Seebeck coefficients [see Figure 9.4 (d)–(f)]. The Seebeck coefficients of A are enhanced upon heat treatment, and the height of the step at 232°C is reduced, leading to similar values after 500 cycles for samples A and B. For sample B, a small effect of the inital annealing is observed. Afterwards, the values remain stable within the error range, reaching a maximum of 269 μVK^{-1} in both samples.
In contrast, sample C exhibits an electrical conductivity σ that is nearly two times higher than those of A and B and has a stronger temperature dependence. Owing to the substitution of Ti with its heavier homologue Zr, the band structure is altered and hence the effective mass and mobilities of the main carriers are affected, leading to different transport properties. Nonetheless, they are more strongly influenced by the heat treatment. Values comparable to those reported in the literature for a ball-milled sample [151] are only reached after 500 cycles. Seebeck coeficients reach the same maximum as in sample B of 269 μVK^{-1} at 700°C after 50 and 100 cycles, but they are reduced about 10% to 246 μVK^{-1} after 500 cycles. The performance, especially at high temperatures, is not very stable, which is reflected in the huge variance of the measurement values. The measurements were repeated several times in order to confirm this unusual behavior.

The dependence of the electrical conductivity and Seebeck coefficients upon the thermal cycling are reflected in the power factors $S^2\sigma$ [see Figures 9.5 (a)–(c)]. The values for sample A vary upon heat treatment and approach the values of sample B, which are again very stable. Their deviation is even smaller than the errors obtained by error propagation, apart from the as-cast sample due to its slightly higher Seebeck coefficient. Both reach a maximum of 2.9×10^{-3} Wm^{-1}K^{-2} after 500 cycles. The temperature dependence of the power factors is very weak and a broad maximum is obtained. Taking into account values from 90% of the maximum (2.6×10^{-3} Wm^{-1}K^{-2}), this maximum spans from 460 to 700°C for sample A and even from 320 to 700°C for sample B. This is very desirable for applications because it expands the utilizable temperature to a very wide range.
Again, the power factors of sample C vary strongly with heat treatment. Even though after 50 cycles a maximum of 4.1×10^{-3} Wm^{-1}K^{-2} is reached at 675 °C, this value is reduced about 25% to 3.1×10^{-3} Wm^{-1}K^{-2} after 500 cycles.
As a consequence, the figure of merit ZT [see Figures 9.5 (d)–(f)] is most stable upon thermal cycling for sample B, but sample A reaches the same values with progressing heat treatment. Both achieve a maximum ZT of 1.1 at 700°C. The figure of merit of sample C reaches a maximum of 1.4 after 50 cycles but then it decreases again to 1.0 after 500 cycles, which is caused by a reduction of the power factor and a concurrent increase of the lattice thermal conductivity. It is very doubtful whether the performance would stabilize upon further thermal cycling.

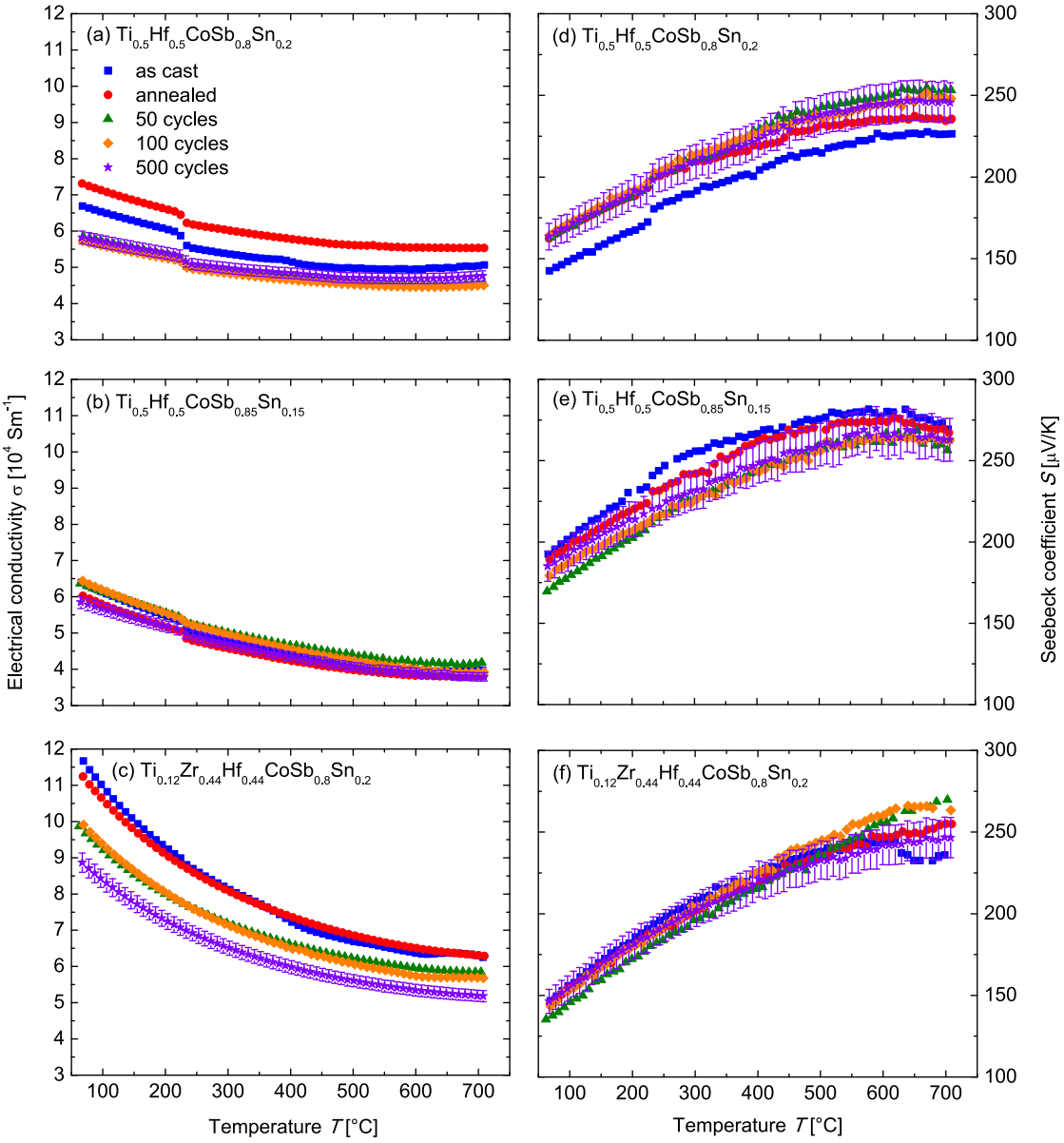

Figure 9.4: Effect of the heat treatment upon (a)–(c) electrical conductivity σ and (d)–(f) Seebeck coefficients S as a function of temperature. For clarity, only error bars for the measurement after 500 cycles are displayed.

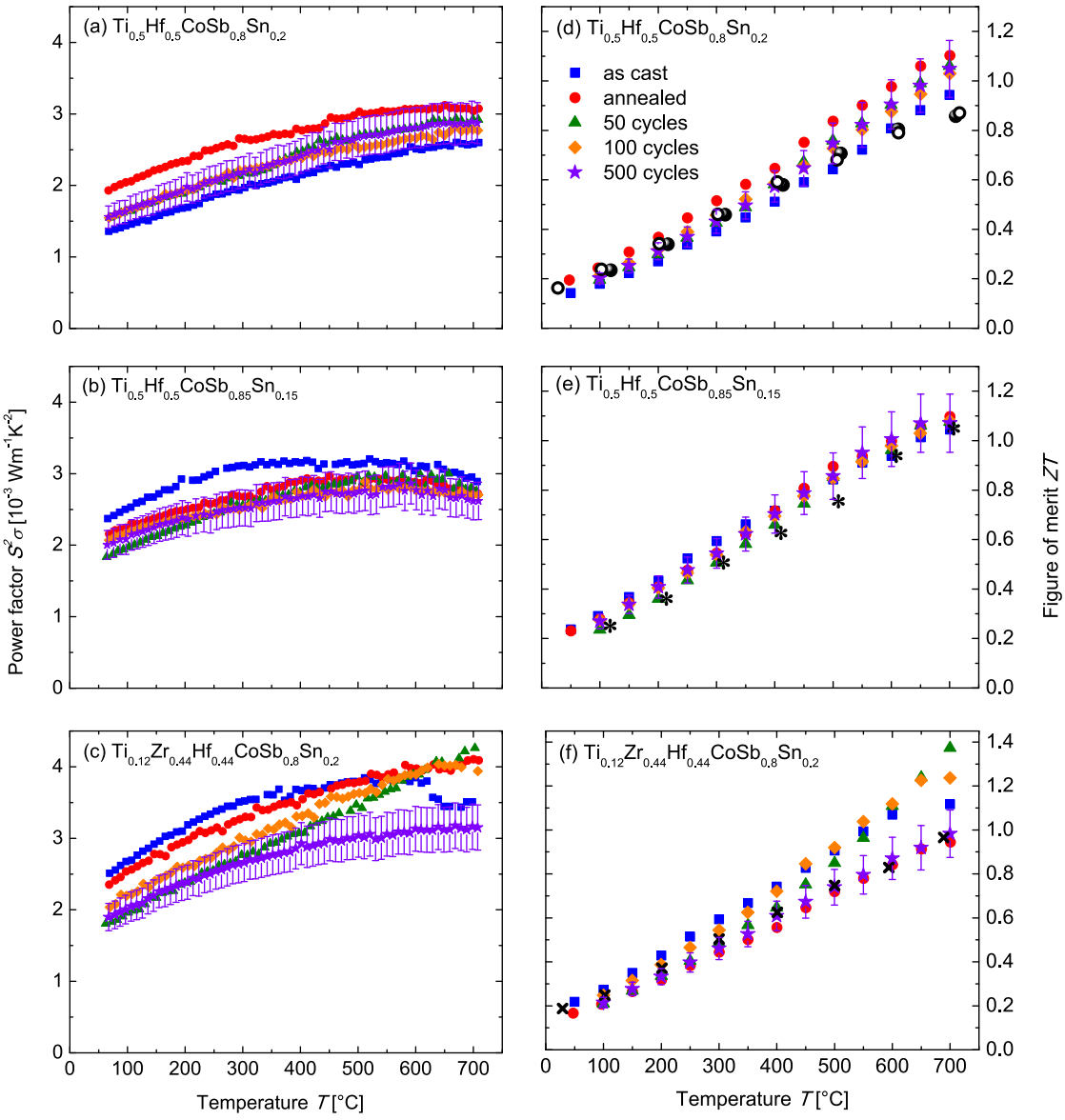

Figure 9.5: Effect of the heat treatment upon (a)–(c) the power factor $S^2\sigma$ and (d)–(f) the figure of merit ZT as a function of temperature and comparison with literature data • [23], see also Chapter 6, ∘ [3], ∗ [59], see also Chapter 8, × [151]. For clarity, only error bars for the measurement after 500 cycles are displayed.

To emphasize the impact of thermal cycling upon the thermoelectric performance, the figure of merit ZT as a function of thermal treatment is displayed in Figure 9.6(a)–(c). Sample A ($Ti_{0.5}Hf_{0.5}CoSb_{0.8}Sn_{0.2}$) stabilizes after cycling, reaching a maximum of ZT = 1.1 at 700°C. The figure of merit of sample B ($Ti_{0.5}Hf_{0.5}CoSb_{0.85}Sn_{0.15}$) is amazingly stable over the whole temperature range, as visualized by lines nearly perfectly parallel to the x-axis. The maximum ZT of 1.1 at 700°C is reached reliably even after 500 cycling steps. The standard deviation of the ZT values measured at the same temperature after progressive heat treatment is between 2–3%. This is significantly smaller than the measurement error of 11%, whereas the standard deviation for sample A is approximately 9%. In contrast, sample C ($Ti_{0.12}Zr_{0.44}Hf_{0.44}CoSb_{0.8}Sn_{0.2}$), which up to now is the record holder for the highest ZT within the TiCoSb system, is clearly affected by the thermal cycling. This is reflected in the high standard deviation of the measurements of 13%. A minimum is observed after annealing and a maximum after 50 cycles. A ZT of 1.4 was obtained, which exceeds the previously reported ZT of 1.02 at 700°C [151] by about 37%. However, this is followed by a downward trend with increasing numbers of cycles corresponding to the ceasing of the degradation of the microstructural network upon repeated cycling. As a consequence, ZT is lowered to 1.0 and it is doubtful whether the thermoelectric properties would remain stable upon further heat treatment. Because all three samples have approximately the same amount of Hf, the partial substitution of Ti by the more expensive Zr is even disadvantageous in terms of the cost of the material [180].

9.3 Conclusion

The best and most reliable performance under thermal cycling conditions is obtained with the composition $Ti_{0.5}Hf_{0.5}CoSb_{0.85}Sn_{0.15}$. This agrees well with the results of the structural property investigations, indicating that the microstructure owing to the phase separation into two half-Heusler phases is stable. The structural and transport properties of $Ti_{0.5}Hf_{0.5}CoSb_{0.8}Sn_{0.2}$ upon prolonged heat treatment converge to the same properties as obtained for $Ti_{0.5}Hf_{0.5}CoSb_{0.85}Sn_{0.15}$. This indicates that a substitution level of 20% Sn on the Sb position is too high to be incorporated into the stable half-Heusler phases. However, the long-term stability of sample C ($Ti_{0.12}Zr_{0.44}Hf_{0.44}CoSb_{0.8}Sn_{0.2}$) is not warranted, even though it shows the best thermoelectric properties after 50 cycles with a maximum figure of merit ZT = 1.4 at 700°C. Repeated heating and cooling cycles lead to the degradation of the structural as well as the thermoelectric properties.

A substitution of 15% Sb by Sn is advantageous for long-term stability of the thermoelectric performance, as proven by the investigation of sample A ($Ti_{0.5}Hf_{0.5}CoSb_{0.8}Sn_{0.2}$) in comparison with sample B ($Ti_{0.5}Hf_{0.5}CoSb_{0.85}Sn_{0.15}$). This agrees well with the study regarding the carrier concentration optimization of the $Ti_{0.3}Zr_{0.35}Hf_{0.35}CoSb_{1-x}Sn_x$ system (see Chapter 7), which proved that a substitution with 15% Sn is optimum [171]. To conclude, composition B ($Ti_{0.5}Hf_{0.5}CoSb_{0.85}Sn_{0.15}$) showed the best and most stable performance under thermal cycling conditions. The intrinsic phase separation, which is

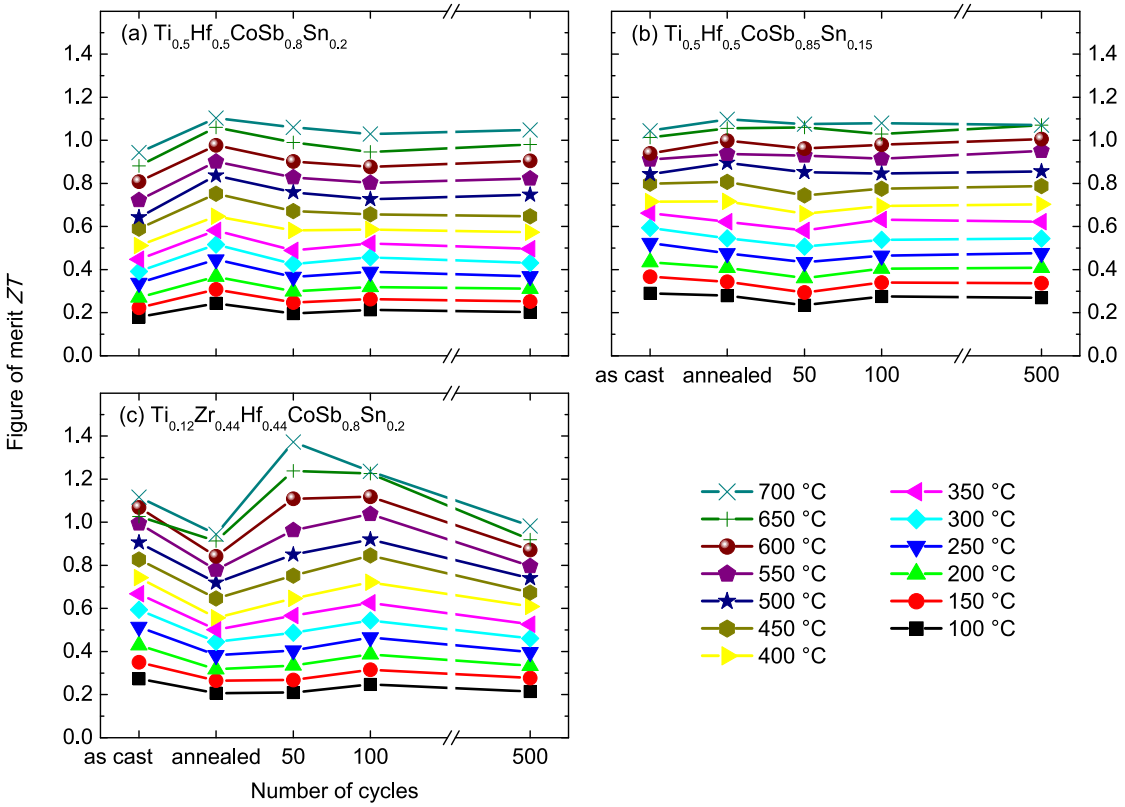

Figure 9.6: Figure of merit ZT as function of number of cycles - each line represents measurements at constant temperature after the various heat treatment steps (see legend).

responsible for the outstanding thermoelectric properties, is stable upon the repeated heating and cooling. A figure of merit $ZT \geq 1$ at 700°C is reached reliably even after 500 heating and cooling cycles. In combination with the high mechanical strength of the material and the broad maximum of the power factor from 320 to 700°C, this is very desirable for the fabrication of thermoelectric modules for applications in the mid-temperature range.

10 Summary and outlook

Half-Heusler compounds are very promising canditates for thermoelectric (TE) energy conversion in the mid-temperature range such as in automotive or industrial waste heat recovery. Attention was attracted to this material class by a record figure of merit $ZT = 1.4$ in the n-type (Ti/Zr/Hf)NiSn system in 2005 [149, 150]. The outstanding performance can be explained by an intrinsic phase separation [11, 14]. However, TE generators require a compatible pair of n- and p-type materials. The realization of a good p-type material in the TiNiSn system is limited due to its electronic band structure (Chapter 3.2.3). State-of-the-art p-type materials can be found in the (Ti/Zr/Hf)$CoSb_xSn_{1-x}$ system. The excellent compatibiltiy of both materials was already demonstrated in a TE Module [5]. To reach a benchmark $ZT \geq 1$ of the TE device, optimization of the p-type system was required. The maximum reported ZT was 0.8 in $Zr_{0.5}Hf_{0.5}CoSb_{0.8}Sn_{0.2}$ by a nanostructuring approach via ball milling [2].

In this work it was shown, that the performance of p-type half-Heusler compounds based on TiCoSb can be tuned by the intrinsic microstructuring via phase separation, generated by isoelectronic alloying of Ti with its heavier homologues Zr and Hf, and by charge carrier concentration variation via substitution of Sb with Sn.

Prior to this, a reproducible fabrication process to achieve an intrinsic phase separation was established (see Chapter 5). The influence of different fabrication procedures on the thermoelectric performance of p-type $Ti_{0.3}Zr_{0.35}Hf_{0.35}CoSb_{0.8}Sn_{0.2}$ was tested. A conventional arc melting preparation procedure leads to an intrinsic microstructuring of the sample and reproducible TE performance. The rapid cooling upon solidification leads to an eutectic microstructure of the sample, which reduces the lattice thermal conductivity by boundary scattering. This initial proof-of-concept served as a very useful starting point for the systematic enhancement of the TE properties.

First, the conditions to achieve phase separation were investigated in detail (see Chapter 6). By isoelectronic alloying of Ti with its heavier homologues Zr and Hf, a pseudo-ternary phase diagram of the (Ti/Zr/Hf)$CoSb_{0.8}Sn_{0.2}$ system was explored. Mandatory to achieve an intrinsic phase separation was the partial substitution of Ti with Hf, which resulted in microstructuring of the system consisting of at least two stable half-Heusler phases – one rich in Ti and Sn and the other rich in Hf and Sb. Similar to the (Ti/Zr/Hf)NiSn system a dendritical phase separation was observed leading to a reduction of the thermal conductivity to 3.2 $Wm^{-1}K^{-1}$ in $Ti_{0.5}Hf_{0.5}CoSb_{0.8}Sn_{0.2}$, which is an improvement of approximately 40% as compared to $TiCoSb_{0.8}Sn_{0.2}$. A maximum ZT of 0.9 at 700°C was reached, enhancing the peak ZT about 80% compared to the best published value of an ingot p-type half-Heusler compound [2]. Hence, the phase separation approach affords thermoelectric properties that are similar to those obtained with nanostructuring approach involving ball milling [3].

Second, the electronic properties were optimized by carrier concentration optimization in the $Ti_{0.3}Zr_{0.35}Hf_{0.35}CoSb_{1-x}Sn_x$ system (see Chapter 7). The maximum power factor of 2.69×10^{-3} $Wm^{-1}K^{-2}$ and maximum figure of merit ZT of 0.79 are reached at $x = 0.15$, which corresponds to a carrier concentration of 1.4×10^{21} cm^{-3}. This leads to enhanced thermoelectric properties compared to the previous state-of-the-art p-type half-Heusler compounds with a substitution level of 20 % Sn. By adjusting the carrier concentration, an enhancement of about 40% in the power factor and figure of merit ZT compared to samples with $x = 0.1$ or 0.2 was achieved simply by choosing a substitution level inbetween those two values. The plot of the transport properties against the carrier concentration illustrates that this system can serve as a model system for the fundamental concept of carrier concentration optimization to enhance ZT, like the well known simulated illustrations of the interrelation of carrier concentration with the TE properties [32, 48]. Thus, a Sn content of 15% was chosen for subsequent enhancements by varying the composition Ti/Zr/Hf instead of using the previous $Zr_{0.5}Hf_{0.5}CoSb_{0.8}Sn_{0.2}$ as a starting point [21]. Combining the optimum carrier concentration with the phase separation appraoch led to an improvement of about 25% as regards the figure of merit in $Ti_{0.5}Hf_{0.5}CoSb_{0.85}Sn_{0.15}$ ($ZT = 1.05$).

In the next step (see Chapter 8), a fine-tuning of the Ti-to-Hf ratio for optimal phonon scattering led to a record figure of merit for p-type half-Heusler compounds. The microstructure of the sample can be controlled by the composition and is correlated to the TE performance. The maximum ZT of 1.2 at 710°C was reached with the composition $Ti_{0.25}Hf_{0.75}CoSb_{0.85}Sn_{0.15}$, this corresponds to an improvement of 20% compared to best sample reported in the literature, $Ti_{0.12}Zr_{0.44}Hf_{0.44}CoSb_{0.8}Sn_{0.2}$ ($ZT \approx 1.0$ at 700°C) fabricated by the nanostructuring approach [151].

Last but not least, the long term stability of the samples was investigated (see Chapter 9). A heating and cooling cycle similar to the operation conditions in an automitove exhaust pipe was performed and the impact on the microstructuring and TE performance was investigated in detail. Three different compositions $Ti_{0.5}Hf_{0.5}CoSb_{0.8}Sn_{0.2}$, $Ti_{0.5}Hf_{0.5}CoSb_{0.85}Sn_{0.15}$, and $Ti_{0.12}Zr_{0.44}Hf_{0.44}CoSb_{0.8}Sn_{0.2}$ were compared. A substitution of 15% Sb by Sn is also advantageous for the long-term stability of the TE performance, since the structural and TE properties of $Ti_{0.5}Hf_{0.5}CoSb_{0.8}Sn_{0.2}$ converge to those of the sample with 15% Sn during the cycling process. In contrast, partial substitution with Zr leads to the occurence of more than two half-Heusler phases and is smearing out the phase interfaces. This leads to a degradation of the microstructuring and TE performance after more than 50 cycles. The material $Ti_{0.5}Hf_{0.5}CoSb_{0.85}Sn_{0.15}$ showed the best and most stable performance under thermal cycling conditions. The intrinsic phase separation, which is responsible for the outstanding thermoelectric properties, is stable upon the repeated heating and cooling. A figure of merit $ZT \geq 1$ at 700°C is reached reliably even after 500 heating and cooling cycles. This, in combination with the high mechanical strength of the material and the broad maximum of the power factor from 320°C to 700°C, is very desirable for the fabrication of thermoelectric modules working in the mid-temperature range.

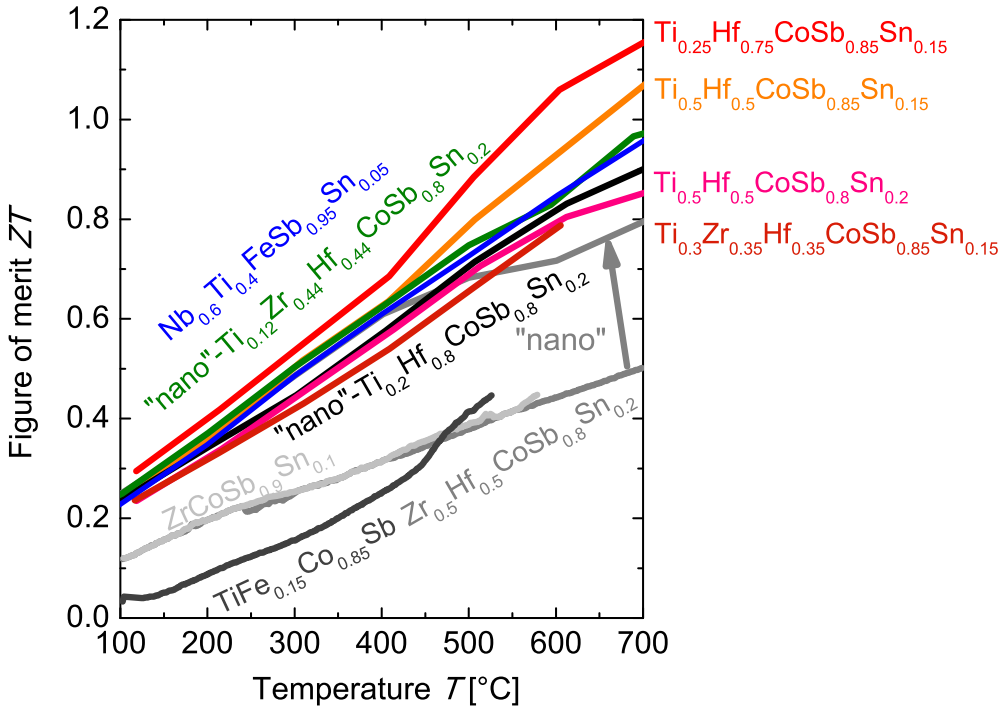

Figure 10.1: Improvements of state-of-the-art half-Heusler compounds for TE applications dated 2015 in comparison with data from 2012 in grey (see chapter 3.4). Enhancement by the ball milling approach are vizualized in green [151], new NbFeSb based compounds in blue [181]. Highlighted in red are the achievements of this work by intrinsic phase separation and carrier concentration optimzation.

In summary, the thermoelectric performance of p-type half-Heusler materials were improved in three steps. Reduction of the lattice thermal conductivity was reached by a intrinsic phase separation approach, carrier concentration optimization enhanced the electronic properties and a fine tuning of the microstructuring via Ti-to-Hf ratio optimization pushed the figure of merit to a record value of 1.2 at 700°C. In combination with the the state-of-the-art n-type $Ti_{0.5}Zr_{0.25}Hf_{0.25}NiSn_{0.998}Sb_{0.002}$ ($ZT = 1.2$ at 560°C) [14] a benchmark of $ZT \geq 1$ could be realized in a TE module based on phase-separated half-Heusler compounds. The proven long-term stability of both materials, as well as their high degree of hardness makes the fabrication of TEGs from half-Heusler materials very attractive. The only little flaw is the relatively high price for Hf [180], which is mandatory to achieve the phase separation and the outstanding TE performance. Future work could expand the concept of intrinsic phase separation to other systems, like VFeSb and NbFeSb, which have recently regained attention as p-type materials [167, 168, 181]. Support towards the understanding and design of intrinsically phase-separated TE materials could be obtained by theoretical calculations, like already demonstrated for the TiCoSb system [118].

11 Acknowledgement

This work would not have been possible without the inspiring, supporting and loving people, I met along my way.

Foremost, I want to express my sincere gratidue to my supervisor for her continious support, and her inexhaustible fundus of creativity and advice, while offering me the necessary scope for scientific and personal development. I am very thankful for the great possibility to work in two different research institutes, which was expanding my knowledge and professional experience significantly.

I am very grateful to my advisors, the leaders of the thermoelectric subgroups, at the JGU Mainz and at the MPI CPfS Dresden. Their guidance, advice, and encouragement was invaluable. Explicitly, I want to thank you, for lots of support and patience during the writing process of our first publication and the elaborate Hall data fitting, and , for your extraordinary good collaboration over the long distance to Dresden. I thank you both, for proof reading of my thesis and a great beamtime in Brazil.

I thank for support with theoretical calculations, physical explanations, and his patience in answering a "chemist's stupid questions". In this context, I also thank and for complementing the experimental results with theoretical calculations regarding the phase separation. It was a pleasure to see how theory meets the experiment.

I thank the former group members at the JGU in Mainz - particulary the members of the thermoelectric subgroup - who provided me with help and guidance, but also cheerful and informative "TelKos" during coffee breaks. Especially, I thank for giving me best possible start in the field, providing always selfless help and advice, and inspiring discussions. The design and setup of the induction furnace is also to his credit, and to the employees of the workshop of the Institute for Inorganic and Analytical Chemistry of the JGU Mainz, whom I also like to thank for fixing everything as soon as possible and making impossible requests possible.

I thank for helping out with all electrotechnical problems, and making my computer always run smoothly guaranteeing acces to my data from anywhere in the world. I also highly appreciate his and help with the bureaucracy.

I thank the numerous students working in our group for a cheerful and productive atmosphere in the lab, particulary my girls and - You are the best, without you, I would have been lost. I thank, for the great experimental work and his essential contribution to Chapter 5.

I thank and for a good time and beeing such a great team during the supervision of inorganic chemistry lab courses.
I thank for readily providing the PXRD machine of the Geoscience Institute whenever the Institutes own facilites could not be used.
I thank and for the introduction to the utilization of the Spark Plasma Sintering.
I thank for introdution and help with the FEI nanoSEM.

I thank all members of the thermoHeusler project for the fruitful collaboration. It was very inspiring too see the upscaling of our materials and fabrication of half-Heusler TE modules.

I thank and , , and for making my stay in Brazil at the LNLS and the URFGS such a great experience and sharing their treasure trove of expertise with the XPD and XAFS beamline, as well as the staff of LNLS Campinas, especially for help with the XPD experiments.

I thank my collegues at the MPI CPfS Dresden for including me easily in the group, helping me to get around the laboratory and spreading a good mood in the office - despite its unfavorable location. I enjoyed very much the international atmosphere at the institute.
Particulary, I thank the following members of the MPI CPfS: for specimen preparation for the microstructural examination and giving me acces and an introduction to the metallographical lab. , , and for SEM pictures, EDX measurements, especially for fulfilling my elaborative special requests for publications. and for ICP-OES analysis. and for heat capacity measurements by DSC and his straightforward support with the data treatement. for ACT and TTO PPMS measurements. and for PXRD measurements.

I gratefully aknowledge the financial support of this work, wich was provided by the DFG Priority Program 1386 Nanostructured Thermoelectric Materials under proposal BA 4171/2-2 and the thermoHEUSLER Project (Project No. 0327876D) of the German Federal Ministry of Economics and Technology (BMWi). Further support of this work was provided by the Brazilian Synchrotron Light Laboratory (LNLS) under proposal XPD - 17015 and by the DAAD (Project No. 57060637).

Invaluable is the support from my friends and family and words can not express my gratitute. I thank every single one of you - and I hope you know, that these lines are dedicated to you - for standing by me through all times.
Special thanks to and , and , and , and , and for providing me with a place to sleep during my numerous research and private visits in Mainz. Thanks to and , and for lending me their spare bicycles.

I am profoundly thankful to , , and for their permanent encouragement and long-distance support from Mainz to Dresden, as well as to for our sunday evenings, and for literally carrying me through my last year.

Finally, I would like to express my heartfelt gratitude to my mum. Her appreciation for education as the most valuable asset and continious encouragement was smoothing my way.

List of Symbols, Notations and Abbreviations

a	Lattice parameter
α	Thermal Diffusivity
AC-T	Alternating current transport
AM	Arc melting
BM	Ball milling
BSE	Back scattered electrons
CB	Conduction band
C_p	Heat capacity
ΔT	Temperature gradient
DOS	Density of states
DSC	Differential scanning calorimetry
e	Elementary charge
EDX	Energy dispersive X-Ray
E_G	Energy band gap
Fraunhofer IPM	Fraunhofer Institute for Physical Measurement Techniques, Freiburg
γ	Band degeneracy
h	Planck constant
HH	Half-Heusler
HV	Vickers hardness
I	Electrical current
ICP-OES	Inductively coupled plasma optical emission spectroscopy
IM	Inductive melting
JGU	Johannes Gutenberg-University, Mainz
k_B	Boltzman constant
κ	Thermal conductivity
κ_{el}	Electronic thermal conductivity
κ_{lat}	Lattice thermal conductivity
l	Mean free path
L	Lorentz number
LFA	Laser flash analysis
LNLS	Brazilian Synchrotron Light Laboratory, Campinas (Brazil)
LSR	Linseis Seebeck Resistivity
m^*	Effective mass
μ	Mobility

μ_H	Hall mobility
MPI CPfS	Max Planck Institute for Chemical Physics of Solids, Dresden
n	Charge carrier concentration
n_H	Hall charge carrier concentration
N	Occupation propability
Π	Peltier coefficient
PGEC	Phonon glass electron crystal
PPMS	Physical properties meassurement system
PXRD	Powder X-Ray diffaction
Q	Heat
$\vec{q}$	Wave vector
R	Gas constant
ρ	Density
R_H	Hall constant
S	Seebeck coefficient
$S^2\sigma$	Power factor
σ	Electrical conductivity
SE	Secondary electrons
SEM	Scanning electron microscopy
T	Temperature
TE	Thermoelectric
TEG	Thermoelectric generator
TTO	Thermal transport option
Θ_D	Debye Temperature
τ	Relaxation time
v	Velocity
VB	Valence band
VE	Valence electrons per unit cell
XPD	X-Ray Powder diffaction beamline at the LNLS
ZT	Figure of merit

List of Figures

List of Tables

Bibliography

[1] M. Schwall and B. Balke. *Appl. Phys. Lett.*, 98(4):042106, 2011.

[2] X. Yan, G. Joshi, W. Liu, Y. Lan, H. Wang, S. Lee, J. W. Simonson, S. J. Poon, T. M. Tritt, G. Chen, and Z. F. Ren. *Nano Lett.*, 11(2):556–60, 2011.

[3] X. Yan, W. S. Liu, H. Wang, S. Chen, J. Shiomi, K. Esfarjani, H. Z. Wang, D. Z. Wang, G. Chen, and Z. F. Ren. *Energ. Environ. Sci.*, 5(6):7543–7548, 2012.

[4] P. Maji, J. P. A. Makongo, X. Zhou, H. Chi, C. Uher, and P. F. P. Poudeu. *J. Solid State Chem.*, 202:70–76, 2013.

[5] K. Bartholomé, B. Balke, D. Zuckermann, M. Köhne, M. Müller, K. Tarantik, and J. König. *J. Electron. Mater.*, 43(6):1775–1781, 2014.

[6] S. Chen and Z. Ren. *Mater. Today*, 16(10):387–395, 2013.

[7] T. Graf, C. Felser, and S. S. P. Parkin. *Prog. Solid State Chem.*, 39(1):1–50, 2011.

[8] J.-W. G. Bos and R. A. Downie. *J. Phys. Condens. Matter*, 26(43):433201, 2014.

[9] W. Xie, A. Weidenkaff, X. Tang, Q. Zhang, J. Poon, and T. M. Tritt. *Nanomaterials*, 2(4):379–412, 2012.

[10] S. Ouardi, G. H. Fecher, C. Felser, M. Schwall, S. S. Naghavi, A. Gloskovskii, B. Balke, J. Hamrle, K. Postava, J. Pitora, S. Ueda, and K. Kobayashi. *Phys. Rev. B*, 86(4):045116, 2012.

[11] J. Krez, J. Schmitt, G. J. Snyder, C. Felser, W. Hermes, and M. Schwind. *J. Mater. Chem. A*, 2(33):13513–13518, 2014.

[12] H. Geng and H. Zhang. *J. Appl. Phys.*, 116(3):033708, 2014.

[13] K. Galazka, S. Populoh, L. Sagarna, L. Karvonen, W. Xie, A. Beni, P. Schmutz, J. u. r. Hulliger, and A. Weidenkaff. *Phys. Status Solidi A*, 211(6):1259–1266, 2014.

[14] M. Schwall and B. Balke. *Phys. Chem. Chem. Phys.*, 15(6):1868–1872, 2013.

[15] R. A. Downie, D. MacLaren, R. I. Smith, and J.-W. G. Bos. *Chem. Commun.*, 49(39):4184–4186, 2013.

[16] Y. Kimura, H. Ueno, and Y. Mishima. *J. Electron. Mater.*, 38(7):934–939, 2009.

[17] M. Schwall, B. Balke, and M. Köhne. Patent Application 20140127070 (May 08, 2014).

[18] S. Sakurada, N. Shutoh, and S. Hirono. US Patent Application US2005/0217715 A1 (October 06, 2005).

[19] N. Shutoh, S. Sakurada, N. Kondo, and N. Takezawa. US Patent Application US20050172994 A1 (August 11, 2005).

[20] M. Köhne, T. Graf, H. J. Elmers, and C. Felser. Patent Application 20130156636 (June 20, 2013).

[21] S. R. Culp, J. W. Simonson, S. J. Poon, V. Ponnambalam, J. Edwards, and T. M. Tritt. *Appl. Phys. Lett.*, 93(2):022105, 2008.

[22] C.-C. Hsu, Y.-N. Liu, and H.-K. Ma. *J. Alloys Compd.*, 597:217–222, 2014.

[23] E. Rausch, B. Balke, S. Ouardi, and C. Felser. *Phys. Chem. Chem. Phys.*, 16(46):25258–62, 2014.

[24] BINE Informationsdienst (FIZ Karlsruhe - Leibniz-Institut für Informationsinfrastruktur GmbH). "The market for wasted energy". http://www.bine.info/en/topics/energy-generation/cogeneration-plants-units/publikation/abwaerme-zu-strom-veredeln-1/der-markt-der-verschwendeten-energie/.

[25] International Energy Agency (IEA/OECD). World energy flow sankey diagram (2012). http://www.iea.org/Sankey/.

[26] Lawrence Livermore National Laboratory. Energy flow charts of primary energy resources and end uses in the united states. https://flowcharts.llnl.gov/index.html.

[27] L. E. Bell. *Science*, 321(5895):1457–1461, 2008.

[28] J. Sommerlatte, K. Nielsch, and H. Böttner. *Physik Journal*, 6(05):35, 2007.

[29] European Comission. Reducing co_2 emissions from passenger cars. http://ec.europa.eu/clima/policies/transport/vehicles/cars/index_en.htm.

[30] H. J. Goldsmid. *Introduction to Thermoelectricity*. Springer Series in Materials Science. Springer-Verlag Berlin Heidelberg, 121.

[31] *CRC Handbook of Thermoelectrics*. CRC Press 1995, 1995.

[32] G. J. Snyder and E. S. Toberer. *Nature Mater.*, 7(2):105–14, 2008.

[33] J. R. Sootsman, D. Y. Chung, and M. G. Kanatzidis. *Angew. Chem. Internat. Ed.*, 48(46):8616–8639, 2009.

[34] K. Schierle-Arndt and W. Hermes. *Chem. Unserer Zeit*, 47(2):92–101, 2013.

[35] T. M. Tritt and M. A. Subramanian. 31(03):188–198, 2006.

[36] Fraunhofer Gesellschaft. Thermoelectric materials nearing production scale. Research news der Fraunhofer Gesellschaft 12/2013.

[37] T. J. Seebeck. *Über den Magnetismus der galvanischen Kette*. Königliche Akademie der Wissenschaften zu Berlin. 1822.

[38] T. J. Seebeck. *Ann. Phys.*, 82(2):133–160, 1826.

[39] California Institute of Technology. Brief history of thermoelectrics. http://thermoelectrics.matsci.northwestern.edu/thermoelectrics/history.html.

[40] E. Altenkirch. *Physik. Z.*, 10:560–580, 1909.

[41] E. Altenkirch. *Physik. Z.*, 12:920, 1911.

[42] A. F. Ioffe. *London: Infosearch*, 1957.

[43] M. V. Vedernikov and E. K. Iordanishvili. A.f. ioffe and origin of modern semiconductor thermoelectric energy conversion. In *Thermoelectrics, 1998. Proceedings ICT 98. XVII International Conference on*, pages 37–42, 1998.

[44] H. J. Goldsmid and R. W. Douglas. *British J. Appl. Phys.*, 5(11):386, 1954.

[45] A. S. Glen. *New Materials and Performance Limits for Thermoelectric Cooling*. CRC Press, 1995. doi:10.1201/9781420049718.ch34.

[46] L. D. Hicks and M. S. Dresselhaus. *Phys. Rev. B*, 47(19):12727–12731, 1993.

[47] M. S. Dresselhaus, G. Chen, M. Y. Tang, R. G. Yang, H. Lee, D. Z. Wang, Z. F. Ren, J. P. Fleurial, and P. Gogna. *Adv. Mater.*, 19(8):1043–1053, 2007.

[48] A. J. Minnich, M. S. Dresselhaus, Z. F. Ren, and G. Chen. *Energy Environ. Sci.*, 2(5):466–479, 2009.

[49] W.-S. Liu, Q. Zhang, Y. Lan, S. Chen, X. Yan, Q. Zhang, H. Wang, D. Wang, G. Chen, and Z. Ren. *Adv. Energy Mater.*, 1(4):577–587, 2011.

[50] B. Poudel, Q. Hao, Y. Ma, Y. Lan, A. Minnich, B. Yu, X. Yan, D. Wang, A. Muto, D. Vashaee, X. Chen, J. Liu, M. S. Dresselhaus, G. Chen, and Z. Ren. *Science*, 320(5876):634–638, 2008.

[51] A. D. LaLonde, Y. Pei, and G. J. Snyder. *Energy Environ. Sci.*, 4(6):2090–2096, 2011.

[52] Q. Zhang, F. Cao, W. Liu, K. Lukas, B. Yu, S. Chen, C. Opeil, D. Broido, G. Chen, and Z. Ren. *J. Am. Chem. Soc.*, 134(24):10031–10038, 2012.

[53] X. Shi, J. Yang, J. R. Salvador, M. Chi, J. Y. Cho, H. Wang, S. Bai, J. Yang, W. Zhang, and L. Chen. *J. Am. Chem. Soc.*, 133(20):7837–7846, 2011.

[54] Q. Jie, H. Wang, W. Liu, H. Wang, G. Chen, and Z. Ren. *Phys. Chem. Chem. Phys.*, 15(18):6809–6816, 2013.

[55] M. Zebarjadi, G. Joshi, G. Zhu, B. Yu, A. Minnich, Y. Lan, X. Wang, M. Dresselhaus, Z. Ren, and G. Chen. *Nano Lett.*, 11(6):2225–2230, 2011.

[56] B. Yu, M. Zebarjadi, H. Wang, K. Lukas, H. Wang, D. Wang, C. Opeil, M. Dresselhaus, G. Chen, and Z. Ren. *Nano Lett.*, 12(4):2077–2082, 2012.

[57] S. R. Brown, S. M. Kauzlarich, F. Gascoin, and G. J. Snyder. *Chem. Mater.*, 18(7):1873–1877, 2006.

[58] E. A. Skrabek and D. S. Trimmer. pages 267 – 275. CRC, Boca Raton, 1995.

[59] E. Rausch, S. Ouardi, U. Burkhardt, C. Felser, J. M. Stahlhofen, and B. Balke. *arXiv:1502.03336 [cond-mat.mtrl-sci]*, 11 Feb 2015.

[60] S. A. Yamini, H. Wang, Z. M. Gibbs, Y. Pei, S. X. Doua, and G. J. Snyder. *Phys. Chem. Chem. Phys.*, 16(5):1835–40, 2014.

[61] G. J. Snyder and T. S. Ursell. *Phys. Rev. Lett.*, 91(14):148301, 2003.

[62] M. Zebarjadi, K. Esfarjani, M. S. Dresselhaus, Z. F. Ren, and G. Chen. *Energy Environ. Sci.*, 5(1):5147–5162, 2012.

[63] F. J. DiSalvo. *Science*, 285(5428):703–706, 1999.

[64] S. LeBlanc, S. K. Yee, M. L. Scullin, C. Dames, and K. E. Goodson. *Renew. Sust. Energ. Rev.*, 32(0):313–327, 2014.

[65] C. Kittel and S. Hunklinger. *Einführung in die Festkörperchemie – Fermi-Gas freier Elektronen*, volume 14, chapter 6, pages 149–177. Oldenbourg Verlag, München Wien, 2006.

[66] J. S. Tse and D. D. Klug. *Recent trends for the Design and Optimization of Thermoelectric materials - A Theoretical perspective*, chapter 8. CRC Press, 2005.

[67] C. Wood. *Rep. Prog. Phys.*, 51(4):459, 1988.

[68] J. P. Heremans, V. Jovovic, E. S. Toberer, A. Saramat, K. Kurosaki, A. Charoenphakdee, S. Yamanaka, and G. J. Snyder. *Science*, 321(5888):554–557, 2008.

[69] N. F. Mott and H. Jones. *The Theory of the Properties of Metals and Alloys.* Dover Publications, New York, 1958.

[70] H. J. Goldsmid and P. L. Balise. *Phys. Today*, 14:72, 1961.

[71] C. Kittel and S. Hunklinger. *Einführung in die Festkörperchemie*, volume 14. Oldenbourg Verlag, München Wien, 2006.

[72] C. Kittel and S. Hunklinger. *Einführung in die Festkörperchemie – Halbleiterkristalle*, volume 14, chapter 8, pages 207–242. Oldenbourg Verlag, München Wien, 2006.

[73] S. K. Mishra, S. Satpathy, and O. Jepsen. *J.Phys. Cond. Mat.*, 9(2):461, 1997.

[74] C. Kittel and S. Hunklinger. *Einführung in die Festkörperchemie – Phononen I & II*, volume 14, chapter 4,5, pages 207–242. Oldenbourg Verlag, München Wien, 2006.

[75] T. Tritt. *Thermal Conductivity*. Physics of Solids and Liquids. Springer US, 2004.

[76] H. J. Goldsmid and A. W. Penn. *Phys. Lett. A*, 27(8):523–524, 1968.

[77] R. Franz and G. Wiedemann. *Ann. Phys.*, 165(8):497–531, 1853.

[78] H.-S. Kim, Z. M. Gibbs, Y. Tang, H. Wang, and G. J. Snyder. *APL Mat.*, 3(4):041506, 2015.

[79] P. Debye. *Ann. Phys.*, 39:789, 1912.

[80] M. G. Kanatzidis. *Chem. Mater.*, 22(3):648–659, 2010.

[81] G. D. Mahan and J. O. Sofo. *Proc. Natl. Acad. Sci. U.S.A.*, 93(15):7436–7439, 1996.

[82] Y. Pei, H. Wang, and G. J. Snyder. *Adv. Mater.*, 24(46):6125–6135, 2012.

[83] Y. Pei, X. Shi, A. LaLonde, H. Wang, L. Chen, and G. J. Snyder. *Nature*, 473(7345):66–69, 2011.

[84] J. P. Heremans, B. Wiendlocha, and A. M. Chamoire. *Energy Environ. Sci.*, 5(2):5510–5530, 2012.

[85] J. W. Simonson, D. Wu, W. J. Xie, T. M. Tritt, and S. J. Poon. *Phys. Rev. B*, 83(23):235211, 2011.

[86] S. M. Kauzlarich, S. R. Brown, and G. J. Snyder. *Dalton Trans.*, (21):2099–2107, 2007.

[87] A. Zevalkink, Y. Takagiwa, K. Kitahara, K. Kimura, and G. J. Snyder. *Dalton Trans.*, 43(12):4720–4725, 2014.

[88] A. Zevalkink, W. G. Zeier, G. Pomrehn, E. Schechtel, W. Tremel, and G. J. Snyder. 5(10):9121–9128, 2012.

[89] G. S. Nolas, G. Fowler, and J. Yang. *J. Appl. Phys.*, 100(4):043705, 2006.

[90] G. S. Nolas, M. Kaeser, R. T. Littleton, and T. M. Tritt. *Appl. Phys. Lett.*, 77(12):1855–1857, 2000.

[91] X. Tang, Q. Zhang, L. Chen, T. Goto, and T. Hirai. *J. Appl. Phys.*, 97(9):093712, 2005.

[92] M. Puyet, A. Dauscher, B. Lenoir, M. Dehmas, C. Stiewe, E. Müller, and J. Hejtmanek. *J. Appl. Phys.*, 97(8):083712, 2005.

[93] S. B. Schujman, G. S. Nolas, R. A. Young, C. Lind, A. P. Wilkinson, G. A. Slack, R. Patschke, M. G. Kanatzidis, M. Ulutagay, and S.-J. Hwu. *J. Appl. Phys.*, 87(3):1529–1533, 2000.

[94] G. S. Nolas, M. Beekman, J. Gryko, G. A. Lamberton, T. M. Tritt, and P. F. McMillan. *Appl. Phys. Lett.*, 82(6):910–912, 2003.

[95] M. Beekman and G. S. Nolas. *J. Mater. Chem.*, 18(8):842–851, 2008.

[96] J.-F. Li, W.-S. Liu, L.-D. Zhao, and M. Zhou. *NPG Asia Mater.*, 2:152–158, 2010.

[97] H. Böttner, G. Chen, and R. Venkatasubramanian. *MRS Bulletin*, 31(03):211–217, 2006.

[98] T. Jäger, P. Holuj, C. Mix, C. Euler, M. H. Aguirre, S. Populoh, A. Weidenkaff, and G. Jakob. *Semicond. Sci. Technol.*, 29(12):124003, 2014.

[99] P. Holuj, C. Euler, B. Balke, U. Kolb, G. Fiedler, P. Kratzer, and G. Jakob. *arXiv preprint arXiv:1504.03468*, 2015.

[100] N. A. Heinz, T. Ikeda, Y. Pei, and G. J. Snyder. *Adv. Funct. Mater.*, 24(15):2135–2153, 2014.

[101] D. L. Medlin and G. J. Snyder. *Curr. Opin. Colloid Interface Sci*, 14(4):226–235, 2009.

[102] G. Gottstein. *Physical Foundations of Materials Science*. Springer-Verlag Berlin Heidelberg, 1 edition, 2004.

[103] H. Fredriksson and U. Akerlind. *Solidification and Crystallization Processing in Metals and Alloys*. Wiley, 2012.

[104] D. A. Porter, K. E. Easterling, and M. Y. Sherif. *Phase Transformations in Metals and Alloys*. CRC Press, 3 edition, 2009.

[105] W. F. Hosford. *Materials Science*. Cambridge University Press, Cambridge, 2006.

[106] *ASM Handbook, Volume 03 - Alloy Phase Diagrams*, volume 03 of *ASM Handbook*. ASM International, 1992.

[107] E. Rausch. *Heusler Verbindungen als p-Typ Halbleiter für thermoelektrische Anwendungen*. Diplom thesis, 2012.

[108] C. Wang, J. Meyer, N. Teichert, A. Auge, E. Rausch, B. Balke, A. Hütten, G. H. Fecher, and C. Felser. *J. Vac. Sci. Technol. B*, 32(2):020802, 2014.

[109] *Red Book on CD-Rom - Constitutional Data and Phase Diagrams.* ASM International, 1990-1995.

[110] H.-J. Wu, W.-J. Foo, S.-W. Chen, and G. J. Snyder. *Appl. Phys. Lett.*, 101(2):023107, 2012.

[111] T. Ikeda, V. Ravi, and G. J. Snyder. *Metall. and Mat. Trans. A*, 41(3):641–650, 2010.

[112] B. Dado, Y. Gelbstein, and M. P. Dariel. *Scripta Mater.*, 62(2):89–92, 2010.

[113] K. Kirievsky, Y. Gelbstein, and D. Fuks. *J. Solid State Chem.*, 203(0):247–254, 2013.

[114] M. Schwall. *Heusler compounds for thermoelectric applications.* PhD thesis, 2014.

[115] J. Krez. *Thermoelectric properties in phase-separated half-Heusler materials.* PhD thesis, 2014.

[116] J. Schmitt. *Investigation of acceptor dopants in ZrNiSn half-Heusler materials.* PhD thesis, 2015.

[117] T. Graf, J. Barth, C. G. F. Blum, B. Balke, C. Felser, P. Klaer, and H.-J. Elmers. *Phys. Rev. B*, 82(10):104420, 2010.

[118] J. M. Mena, E. Rausch, S. Ouardi, T. Gruhn, G. H. Fecher, H. G. Schoberth, H. Emmerich, and C. Felser. *submitted to J. Electron. Mater. (ICT 2015 proceedings)*, 2015.

[119] F. Heusler, W. Starck, and E. Haupt. *Verh. d. DPG*, 5:220 –223, 1903.

[120] F. Heusler. *Verh. d. DPG*, 5:219, 1903.

[121] C. Felser, G. H. Fecher, and B. Balke. *Angew. Chem. Int. Ed.*, 46(5):668–699, 2007.

[122] A. K. Nayak, M. Nicklas, S. Chadov, P. Khuntia, C. Shekhar, A. Kalache, M. Baenitz, Y. Skourski, V. K. Guduru, A. Puri, U. Zeitler, J. M. D. Coey, and C. Felser. *Nat. Mater.*, advance online publication, 2015.

[123] C. Felser, L. Wollmann, S. Chadov, G. H. Fecher, and S. S. P. Parkin. *APL Mater.*, 3(4):041518, 2015.

[124] O. Meshcheriakova, S. Chadov, A. K. Nayak, U. K. Rößler, J. Kübler, G. Andr, A. A. Tsirlin, J. Kiss, S. Hausdorf, A. Kalache, W. Schnelle, M. Nicklas, and C. Felser. *Phys. Rev. Lett.*, 113(8):087203, 2014.

[125] W. Jeitschko. *Metall. Trans.*, 1(10):2963–2965, 1970.

[126] L. O. Grondahl and S. Karrer. *Phys. Rev.*, 33(6):531–537, 1911.

[127] F. Heusler. *Angew. Chem.*, 17(9):260–264, 1904.

[128] F. Heusler. *Z. Anorg. Chem.*, 88(1):185–188, 1914.

[129] F. Heusler and F. Richarz. *Z. Anorg. Chem.*, 61(1):265–279, 1909.

[130] O. Heusler. *Z. Anorg. Allg. Chem.*, 159(1):37–54, 1927.

[131] F. Heusler. *Z. Anorg. Allg. Chem.*, 161(1):159–160, 1927.

[132] O. Heusler. *Z. Anorg. Allg. Chem.*, 171(1):126–142, 1928.

[133] A. J. Bradley and J. W. Rodgers. *Proc. R. Soc. A*, 144(852):340–359, 1934.

[134] H. C. Kandpal, C. Felser, and R. Seshadri. *J. Phys. D: Appl. Phys.*, 39(5):776, 2006.

[135] D. Jung, H. J. Koo, and M. H. Whangbo. *J. Mol. Struc.:Theochem*, 527(13):113–119, 2000.

[136] D. Bende, F. R. Wagner, and Y. Grin. *Inorg. Chem.*, 54(8):3970–3978, 2015.

[137] J. Pierre, R. V. Skolozdra, Y. K. Gorelenko, and M. Kouacou. *J. Magn. Magn. Mater.*, 134(1):95–105, 1994.

[138] J. Tobola, J. Pierre, S. Kaprzyk, R. V. Skolozdra, and M. A. Kouacou. *J. Phys. Condens. Matter*, 10(5):1013, 1998.

[139] S. Chadov, X. Qi, J. Kübler, G. H. Fecher, C. Felser, and S. C. Zhang. *Nat. Mater.*, 9(7):541–545, 2010.

[140] J. O. Sofo and G. D. Mahan. *Phys. Rev. B*, 49(7):4565–4570, 1994.

[141] R. P. Chasmar and R. Stratton. *J. Electron. Control*, 7(1):52–72, 1959.

[142] G. D. Mahan. *J. Appl. Phys.*, 65(4):1578–1583, 1989.

[143] J. Yang, H. Li, T. Wu, W. Zhang, L. Chen, and J. Yang. *Adv. Funct. Mater.*, 18(19):2880–2888, 2008.

[144] L. L. Wang, L. Miao, Z. Y. Wang, W. Wei, R. Xiong, H. J. Liu, J. Shi, and X. F. Tang. *J. Appl. Phys.*, 105(1):013709, 2009.

[145] S. Ouardi, G. H. Fecher, B. Balke, X. Kozina, G. Stryganyuk, C. Felser, S. Lowitzer, D. Ködderitzsch, H. Ebert, and E. Ikenaga. *Phys. Rev. B*, 82(8):085108, 2010.

[146] J. E. Douglas, C. S. Birkel, N. Verma, V. M. Miller, M.-S. Miao, G. D. Stucky, T. M. Pollock, and R. Seshadri. *J. Appl. Phys.*, 115(4):043720, 2014.

[147] J. Schmitt, Z. M. Gibbs, G. J. Snyder, and C. Felser. *Mater. Horiz.*, 2(1):68–75, 2015.

[148] S. Ouardi, G. H. Fecher, B. Balke, M. Schwall, X. Kozina, G. Stryganyuk, C. Felser, E. Ikenaga, Y. Yamashita, S. Ueda, and K. Kobayashi. *Appl. Phys. Lett.*, 97(25):252113, 2010.

[149] N. Shutoh and S. Sakurada. *J. Alloys Compd.*, 389(12):204–208, 2005.

[150] S. Sakurada and N. Shutoh. *Appl. Phys. Lett.*, 86(8):082105, 2005.

[151] X. Yan, W. Liu, S. Chen, H. Wang, Q. Zhang, G. Chen, and Z. F. Ren. *Adv. Energy Mater.*, 3(9):1195–1200, 2013.

[152] G. Joshi, T. Dahal, S. Chen, H. Wang, J. Shiomi, G. Chen, and Z. Ren. *Nano Energy*, 2(1):82–87, 2013.

[153] S. R. Culp, S. J. Poon, N. Hickman, T. M. Tritt, and J. Blumm. *Appl. Phys. Lett.*, 88(4):042106, 2006.

[154] Y. Kimura, T. Kuji, A. Zama, Y. Shibata, and Y. Mishima, 2005.

[155] T. Wu, W. Jiang, X. O. Li, Y. F. Zhou, and L. D. Chen. *J. Appl. Phys.*, 102(10):103705, 2007.

[156] T. Sekimoto, K. Kurosaki, H. Muta, and S. Yamanaka. *Jpn. J. Appl. Phys.*, 46(25-28):L673–L675, 2007.

[157] J. Krez, B. Balke, C. Felser, W. Hermes, and M. Schwind. *arXiv:1502.01828 [cond-mat.mtrl-sci]*, 6 Feb 2015.

[158] F. F. Ferreira, E. Granado, W. Carvalho Jr, S. W. Kycia, D. Bruno, and R. Droppa Jr. *J. Synchrotron Radiat.*, 13(1):46–53, 2006.

[159] L.-D. Zhao, V. P. Dravid, and M. G. Kanatzidis. *Energy Environ. Sci.*, 7(1):251–268, 2014.

[160] Y. Gelbstein, J. Davidow, S. N. Girard, D. Y. Chung, and M. Kanatzidis. *Adv. Energy Mater.*, 3(6):815–820, 2013.

[161] K. Kurosaki, T. Maekawa, H. Muta, and S. Yamanaka. *J. Alloys Compd.*, 397(12):296–299, 2005.

[162] S. Populoh, M. H. Aguirre, O. C. Brunko, K. Galazka, Y. Lu, and A. Weidenkaff. *Scr. Mater.*, 66(12):1073–1076, 2012.

[163] T. Graf, P. Klaer, J. Barth, B. Balke, H.-J. Elmers, and C. Felser. *Scr. Mater.*, 63(12):1216–1219, 2010.

[164] M. A. Verges, P. J. Schilling, P. Upadhyay, W. K. Miller, R. Yaqub, K. L. Stokes, and P. F. P. Poudeu. *Sci. Adv. Mater.*, 3(4):659666, 2011.

[165] P. Sahoo, Y. Liu, J. P. A. Makongo, X.-L. Su, S. J. Kim, N. Takas, H. Chi, C. Uher, X. Pan, and P. F. P. Poudeu. *Nanoscale*, 5(19):9419–9427, 2013.

[166] V. Ponnambalam, P. N. Alboni, J. Edwards, T. M. Tritt, S. R. Culp, and S. J. Poon. *J. Appl. Phys.*, 103(6):063716, 2008.

[167] C. Fu, T. Zhu, Y. Liu, H. Xie, and X. Zhao. *Energy Environ. Sci.*, 8(1):216–220, 2015.

[168] C. Fu, T. Zhu, Y. Pei, H. Xie, H. Wang, G. J. Snyder, Y. Liu, Y. Liu, and X. Zhao. *Adv. Energy Mater.*, 4(18):1400600, 2014.

[169] H. C. Kandpal, V. Ksenofontov, M. Wojcik, R. Seshadri, and C. Felser. *J. Phys. D: Appl. Phys.*, 40(6):1587, 2007.

[170] B. Balke, S. Ouardi, T. Graf, J. Barth, C. G. F. Blum, G. H. Fecher, A. Shkabko, A. Weidenkaff, and C. Felser. *Solid State Commun.*, 150(1112):529–532, 2010.

[171] E. Rausch, B. Balke, T. Deschauer, S. Ouardi, and C. Felser. *APL Mat.*, 3(4):041516, 2015.

[172] D. Jänsch. *Thermoelektrik: Eine Chance für die Automobilindustrie.* Expert-Verlag GmbH, 2008.

[173] M. Mikami, M. Mizoshiri, K. Ozaki, H. Takazawa, A. Yamamoto, Y. Terazawa, and T. Takeuchi. *J. Electron. Mater.*, 43(6):1922–1926, 2014.

[174] E. Hatzikraniotis, K. T. Zorbas, I. Samaras, T. Kyratsi, and K. M. Paraskevopoulos. *J. Electron. Mater.*, 39(9):2112–2116, 2010.

[175] W. J. Xie, X. F. Tang, Y. G. Yan, Q. J. Zhang, and T. M. Tritt. *J. Appl. Phys.*, 105(11):113713, 2009.

[176] I. Hideo. *Jpn. J. Appl. Phys.*, 53(12):125502, 2014.

[177] K. C. Lukas, W. S. Liu, Q. Jie, Z. F. Ren, and C. P. Opeil. *Rev. Sci. Instrum.*, 83(11):115114, 2012.

[178] G. Skomedal, N. R. Kristiansen, M. Engvoll, and H. Middleton. *J. Electron. Mater.*, 43(6):1946–1951, 2014.

[179] J. Martin, W. Wong-Ng, T. Caillat, I. Yonenaga, and M. L. Green. *J. Appl. Phys.*, 115(19):193501, 2014.

[180] Shanghai Metals Market. www.metal.com.

[181] G. Joshi, R. He, M. Engber, G. Samsonidze, T. Pantha, E. Dahal, K. Dahal, J. Yang, Y. Lan, B. Kozinsky, and Z. Ren. *Energy Environ. Sci.*, 7(12):4070–4076, 2014.